7-2-2012

Design and construction of a Bose Einstein condensate machine

Paul W. Blackburn

Paul W. Blackburn

Candidate

Department of Physics and Astronomy

Department

This thesis is approved, and it is acceptable in quality and form for publication:

Approved by the Thesis Committee:

Ivan Deutsch , Chairperson

Wolfgang Rudolph

Malcolm Boshier

Design and Construction of a Bose Einstein Condensate Machine

by

Paul W. Blackburn

Licenciatura en Ciencias c/m en Física, Universidad de Chile, 2003
Magíster en Ciencias c/m en Física, Pontificia Universidad Católica de Chile, 2007

THESIS

Submitted in Partial Fulfillment of the
Requirements for the Degree of

Master of Science
Physics

The University of New Mexico

Albuquerque, New Mexico

May, 2012

Dedication

To Mum and Dad. =P

Acknowledgments

Quite apart from the enormous body of physical knowledge and intuition that my advisor, Malcolm Boshier, wields day in and day out wrangling BECs and the Quantum world, I would like to point out that he also possesses an amazing capacity for patience and a much-appreciated willingness to explain things for the umpteenth time. These are the core qualities that have allowed me to complete this Masters program, and for this I thank him deeply. The window that he has held open while I peered into the world of down-to-earth experimental physics has provided a view of the process I will not forget. May the Science be rich and the bureaucracy featherlight, Malcolm.

It is often said that Ivan Deutsch is the best-dressed man in the UNM Physics Department, and though I would not even consider challenging that notion, I will instead remember him for his incomparable support as my academic advisor for all five years of my time at UNM. An even keel and a voice of reason, I have always felt I could turn to him and receive valuable advice. It'll be strange not emailing him every few months to update him on my status and progress. Perhaps I'll do it anyway.

The person that first taught me the basics of lasers in 2008 ended up being the same person that seeded the idea for the general focus of this thesis in 2011, and there is something quite pleasing about coming full circle. The influence of Wolfgang Rudolph has therefore been subtly present throughout all of my graduate work, and for this I am thankful.

Though we never actually chatted over the water cooler (not that there is one in our hallway, anyway), I thoroughly enjoyed the "water cooler" conversations I had with Warren Lybarger about Life, the Universe and Everything. Thanks man, and best of luck out on the West Coast.

To the team that taught me my way around the Machine Shop—Mark Peters, Al Urbaitis, Shaun Newman—, I thank you for teaching me how to build useful things out of hunks of metal (over fun and interesting conversation, no less). I'm sure you also want to thank *me* for not cutting a finger off, so... you're welcome.

And last (and foremost) my parents, always shining their support and love from half a world away.

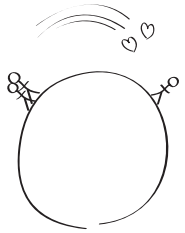

Most of the drawings depicting the experimental systems included in this thesis could not have been created with the detail and precision seen here if it were not for the use of technical drawings provided by the manufacturers. The author would like to thank the following companies for their kind permission to allow the inclusion of their technical drawings as part of some of the illustrations used in this Thesis: Agilent Technologies, Hellma, Kimball Physics Inc., MDC Vacuum Products LLC, Newport and Thorlabs.

LA-UR-12-20533

Design and Construction of a Bose Einstein Condensate Machine

by

Paul W. Blackburn

Licenciatura en Ciencias c/m en Física, Universidad de Chile, 2003
Magíster en Ciencias c/m en Física, Pontificia Universidad Católica de Chile, 2007

M.S., Physics, University of New Mexico, 2012

Abstract

A dilute gas Bose Einstein condensate (BEC) is a state of matter that occurs when a cloud of atoms in a potential are made cold and dense enough that they all occupy the potential's ground state. The onset of this phenomenon occurs when their de Broglie wavelength, $\Lambda = \sqrt{2\pi\hbar^2/mk_BT}$, becomes comparable in size to the inter-particle spacing. A BEC is a macroscopic quantum object, since all atoms in the BEC are described by a single quantum wavefunction and, as such, is a fundamental quantum many-body system. The first experimental demonstration of a dilute gas BEC was performed by Eric Cornell and Carl Wieman in 1995 and since then, several dozen groups around the world have achieved and study BECs.

This Thesis documents design and construction work performed in support of the Bose Einstein Condensate (BEC) experiment at the Los Alamos National Laboratory. The objective of the work performed was to upgrade the existing BEC machine in most of its significant subsystems to attain better experimental cycle times and BECs with a larger atom number than what was previously attainable, as well as improve the optical quality of the imaging and laser manipulation beams at the location of the BEC. These objectives were achieved through the construction of a new laser system with greater power and larger magneto-optical trap (MOT) beam diameters, a new quadrupole magnetic trap with better optical access and higher magnetic field gradients than the Ioffe-Pritchard coil configuration it replaced, and a cuvette-style quartz cell with a much higher optical quality than the hand-blown cell used previously.

In addition to these improvements the feasibility of using phase-contrast imaging of the BECs created in this machine for future experimental goals was evaluated and found to be feasible.

Contents

List of Figures

List of Tables

Chapter 1

Introduction

1.1 The Physics of BEC: A brief overview

As anyone who has chosen a career in Physics can confirm, explaining to the layman what exactly one does can sometimes be a bit of a challenge. Consider, in this case, the simplest description of the subject of this thesis: a machine that creates Bose Einstein condensates. Opting to keep it as simple as possible, one might say that it is a machine that cools certain atoms to very, very cold temperatures. Pressed further, one might add that the motivation for doing so is that at these temperatures, the atoms behave in a different way than at higher temperatures, and this different behavior is interesting, and can be useful. Specifying exactly *how* this behavior is different and *why* it can be useful requires a little more knowledge of physics that can be effectively conveyed over a single beverage of one's choice.

One approach to conveying the importance of a Bose Einstein condensate—this special collection of very cold atoms—is to say that its most salient feature is that all member atoms share the same quantum-mechanical phase. Ordinarily, in the case of cold-but-not-*that*-cold atoms, there would be no reason for this to be so, just as a thermal light source like a light bulb, say, emits photons with completely uncorrelated phase. Even if we were to restrict the light of a source to that produced by a single atomic transition, such as one of the sodium D lines at 590.0 or 590.6 nm of a sodium gas discharge lamp, we would find that the light beam derived from such a source does not have coherent phase: the light is produced as a result of many emitters acting independently. The light from a laser beam, however, does, as the photons produced by stimulated emission in the laser gain medium share the phase, wavevector direction and wavelength of the incoming photon that stimulated their emission. Atoms in a BEC are

analogous to photons from a laser source in the sense that they all share the same quantum mechanical description of their state. The condensate—as a whole, from few hundred thousand to a few million atoms in number and from a micrometer to a few hundred micrometers in extent[1]—is described by a single wavefunction. The atoms, in effect, are collectively a macroscopic quantum object that can be pushed, pulled, made to interfere with other condensates and with itself.

The first observed manifestations of condensation phenomena did not occur in a dilute atomic gas, as is used in the LANL BEC experiment, but rather as the phenomena of superfluidity of ^{4}He [1] in 1938 and of superconductivity [2] in 1911 (though it was not until the arrival of BCS theory that condensation and superconductivity were conclusively linked [3–5]) . Condensation in dilute atomic gases was only observed for the first time by the group of Wieman and Cornell in ^{87}Rb in 1995 [6] and shortly after in ^{23}Na by Ketterle's group [7] and in ^{7}Li by Hulet's group [8]. Cornell, Ketterle and Wieman were awarded the 2001 Nobel Prize in Physics for this work. Condensation was only made possible because of previous advances in techniques for laser cooling of neutral atoms from the 1970s and 1980s, most notably the demonstration in 1982 of a method of cooling neutral atoms via a combination of laser light and magnetic fields, a magneto-optical trap (MOT) [9], which will be discussed below. The present-day list of species condensed to BEC is long (^{1}H [10], ^{85}Rb [11], ^{4}He* [12,13], ^{41}K [14], ^{133}Cs [15], ^{174}Yb [16], ^{52}Cr [17], ^{84}Sr [18], ^{86}Sr [19], ^{88}Sr [20]) and is bound to get longer.

1.2 Quantum-mechanical and statistical description of BEC

Bose Einstein condensation was predicted by Albert Einstein [21, 22] as an application of the quantum statistics of photons developed by Satyendra Nath Bose [23] to massive particles—atoms, in this case. Essentially, bosons (particles of integer spin) will undergo a phase transition if their temperature drops and spatial density increases to the extent that the atomic separation becomes comparable to the de Broglie wavelength,

$$\Lambda = \frac{h}{\sqrt{2\pi m k_B T}}, \tag{1.1}$$

where h is Plack's constant, k_B is Boltzmann's constant and T is the atoms' temperature. In the current experimental setup, where ^{87}Rb is cooled to a few tens of nK, Λ increases by around six orders of magnitude to about 1 μm, which is about the size of the smallest dimension of the BECs created in our lab. This transition can also be defined as when the number density reaches [24]

$$n = \frac{2.6}{\Lambda^3}. \tag{1.2}$$

[1] In the case of a dilute gas atomic BEC.

1.2.1 A basic description of condensation

The fundamental reason for this condensation has to do with the statistics obeyed by the particles that compose the system. The wavefunction that describes a quantum mechanical system of indistinguishable particles is either symmetric (as is the case for bosons) or antisymmetric (for fermions) under the exchange of any two particles. It can be shown [25] that the number of non-interacting bosons of in a single-particle state of energy ϵ_i in a system at temperature T follows the Bose-Einstein distribution function

$$N_i(\epsilon_i) = \frac{1}{e^{(\epsilon_i - \mu)\beta} - 1}, \tag{1.3}$$

where μ is the chemical potential and $\beta = 1/k_B T$. In the context of trapped bosons, as is our case, ϵ_i is the energy of the single-particle state for the trapping potential. Note that at high temperatures, this distribution function approximates the Boltzmann distribution, $N_i \sim e^{-(\epsilon_i - \mu)/k_B T}$.

By simple examination of Equation 1.3 it is apparent that the chemical potential, which is a function of the total particle number N and temperature T, cannot be larger than the energy of the ground state, ϵ_0. If this were so, the ground state occupation would be negative, and this is unphysical. Similarly, the chemical potential cannot be equal to ϵ_0, because this would result in an infinite occupation. It follows, then, that $\mu < \epsilon_0$. Again returning to Equation 1.3, we find that if $\mu < \epsilon_0$, then

$$\frac{1}{e^{\beta(\epsilon_i - \mu)} - 1} < \frac{1}{e^{\beta(\epsilon_i - \epsilon_0)} - 1} \tag{1.4}$$

for all excited states with $i > 0$. In other words, the occupation of the excited states cannot exceed a certain quantity that is a function of temperature. If we write the total number of particles as a sum of the ground state occupation and that of the excited states

$$N = N_0 + N_{\text{ex}} \tag{1.5}$$

$$= N_0 + \sum_{i \neq 0} \frac{1}{e^{\beta(\epsilon_i - \mu)} - 1} \tag{1.6}$$

it is apparent that as the temperature is lowered, each term of the summation is bounded from above by a quantity that decreases as a function of decreasing T. As a result, the ground state occupation N_0 must rise to keep N unchanged.[2] This, in a nutshell, is how more and more bosons end up condensed in the ground state as the temperature is lowered.

The temperature T_c which determines the onset of condensation is called the critical temperature, and can be calculated in the semiclassical approximation from a more explicit form of Equation 1.5 [26].

[2]Note that μ must necessarily approach ϵ_0 as T is lowered, or else N could not be held constant, since all terms of Equation 1.5 would decrease with decreasing temperature.

For a three-dimensional harmonic oscillator potential $V(\mathbf{r}) = (m/2)(\omega_x^2 x^2 + \omega_y^2 y^2 + \omega_z^2 z^2)$ of angular frequencies ω_x, ω_y and ω_z, we consider Equation 1.5 evaluated at T_c (expressed as $\beta_c = 1/k_B T_c$) and the critical chemical potential at transition, $\mu_c = (\omega_x + \omega_y + \omega_z)\hbar/2$. At transition, then,

$$N - N_0 = \sum_{n_x, n_y, n_z \neq 0} \frac{1}{\exp[\hbar(\omega_x n_x + \omega_y n_y + \omega_z n_z)\beta_c] - 1}. \tag{1.7}$$

For large N, the level spacing is comparatively small enough that the sum can be replaced by an integral in the continuous variables n_x, n_y and n_z. This will provide a good approximation if $\hbar\bar{\omega}/k_B T_c \ll 1$ with $\bar{\omega} = (\omega_x \omega_y \omega_z)^{1/3}$ the geometrical mean of oscillator frequencies. Evaluating the integral and solving for T_c yields

$$T_c = \frac{\hbar\bar{\omega}}{k_B}\Big(\frac{N}{\zeta(3)}\Big)^{1/3} = 0.94\frac{\hbar\bar{\omega}}{k_B}N^{1/3}, \tag{1.8}$$

where we have taken $N_0 \to 0$ at T_c and ζ is the Riemann Zeta function. As an illustration, for $\bar{\omega} = 2\pi \times 100$ Hz and $N = 10^6$ atoms, the critical temperature is about 450 nK. The temperature dependence of the condensate fraction shows a cubic dependence on T, and is found to be [26]

$$\frac{N_0}{N} = 1 - \Big(\frac{T}{T_c}\Big)^3. \tag{1.9}$$

1.2.2 The Gross-Pitaievskii equation and the Thomas-Fermi approximation

Up to this point we have considered particles that do not interact. In this case the Hamiltonian that describes the condensed atoms is simply a sum of the single-particle harmonic oscillator Hamiltonians, and the volumetric density distribution of condensed atoms is $n(\mathbf{r}) = N|\phi_0(\mathbf{r})|^2$, with

$$\phi_0(\mathbf{r}) = \left(\frac{m\bar{\omega}}{\pi\hbar}\right)^{3/4} \exp\left[-\frac{m}{2\hbar}(\omega_x x^2 + \omega_y y^2 + \omega_z z^2)\right], \tag{1.10}$$

of average width $a_{\text{ho}} = \sqrt{\hbar/m\bar{\omega}}$. Note that in the absence of interactions, the size of the cloud is independent of N [26].

If atom-atom interactions are taken into account, however, the width and density distribution is considerably affected. The low-energy interaction between ^{87}Rb atoms is repulsive, and this lowers the peak density and widens the distribution. If the two-body potential is modeled as

$$V(\mathbf{r}' - \mathbf{r}) = g\delta(\mathbf{r}' - \mathbf{r}) \tag{1.11}$$

with $g = 4\pi\hbar^2 a/m$ a coupling constant that is a function of the scattering length a, then the many-body Hamiltonian governing the dynamics and interactions of the condensate can be reduced to the far more

tractable time-independent Gross-Pitaevskii [27, 28] equation (GPE):

$$\mu\phi(\mathbf{r}) = \left(-\frac{\hbar^2\nabla^2}{2m} + V_{\text{ext}}(\mathbf{r}) + g|\phi(\mathbf{r})|^2\right)\phi(\mathbf{r}) \tag{1.12}$$

with solution $\Phi(\mathbf{r}, t) = \phi(\mathbf{r})e^{-i\mu t/\hbar}$ [29]. This simplification is valid as long as there are many atoms in the condensate and the scattering length is short compared to the average distance between atoms. For ^{87}Rb atoms in the $|F = 1, m_F = -1\rangle$ state the scattering length for s-wave interactions is about 100.4 times the Bohr atomic radius [30]. In the LANL BEC, for example, condensates of number density on the order of $\rho_0 = 10^{20}$ m^{-3} are created, with an approximate inter-particle spacing of $\rho_0^{-1/3} = 2 \times 10^{-7}$ m. This implies that the ratio of scattering length to average particle separation is about 40.

If the atom number is large enough and the atom-atom interactions are repulsive, a further simplification can be carried out. The Thomas-Fermi approximation consists in neglecting the kinetic energy term of the GPE, proportional to $\nabla^2\phi$ [31]. As a result of this approximation, the time-independent GPE (Equation 1.12) becomes

$$\left[V_{\text{ext}}(\mathbf{r}) + g|\phi(\mathbf{r})|^2\right]\phi(\mathbf{r}) = \mu\phi(\mathbf{r}) \tag{1.13}$$

with simple solution

$$n(\mathbf{r}) = |\phi(\mathbf{r})|^2 = \begin{cases} \frac{\mu - V_{\text{ext}}(\mathbf{r})}{g} & \text{where the function is positive,} \\ 0 & \text{otherwise.} \end{cases} \tag{1.14}$$

In the Thomas-Fermi approximation, the first thing one notices is that the density profile is simply the negative of the trapping potential. Thus, for a harmonic potential, the three radii of the condensate are simply $R_i = \sqrt{2\mu/m}/\omega_i$.

1.3 Trapping, cooling and condensing

Armed with this overview of what exactly a BEC is, it remains to be seen how ^{87}Rb atoms can be cooled to the few hundreds of nK required for condensation. The first step, of course, is to catch enough atoms. But how?

Before we consider how to trap and cool them, we should ensure that they are isolated from external influences that might heat them up. As we will see shortly, it is possible to hold them in space via non-mechanical means. Having gone to the trouble of suspending the atoms in space, it would be foolish to expect them to be cooled much if they interact with gas at a room temperature, so we choose to

suspend them in an ultra-high vacuum (UHV), on the order of 10^{-11} Torr. Next up on the list of things to consider is the influence of the blackbody radiation emitted by the vacuum chamber's walls, which are at room temperature. Luckily, the optical transitions of our alkali species have energies much greater than $k_B T$ (not to mention a relatively narrow linewidth), and the characteristic excitation time for Rb in 25 °C blackbody radiation is on the order of 10^{11} years [32][3]. In short, our safest bet is to trap the atoms in a UHV chamber, minimizing contact with other, non-trapped atoms.

The two main approaches to the problem of accumulating atoms take different tacks, but are based on the same principle. One possibility is to use an oven to raise the vapor pressure of the alkali species in a localised area of the experiment's vacuum system. Hot atoms, with a corresponding thermal velocity distribution, are produced relatively far from the main science chamber and directed down a long tube. On their journey, they encounter a counter-propagating laser beam that is near-resonant with a Zeeman-shifted transition. The atoms are slowed by absorbing Doppler-shifted photons from the beam. Each absorbed photon reduces the atom's momentum by $\hbar k$. The excited atom re-emits the photon in a random direction, and over many interactions, the time-averaged net force (which we will call a scattering force) on the atom due to these re-emissions is very small (though not negligible, as will be discussed below). As the atoms lose momentum, they see a different Doppler-shifted laser frequency, so they are kept in resonance with the beam by a spatially decreasing magnetic field that continuously reduces the relevant transition's frequency. At the end of the slowing stage, the atoms' velocity is low enough to be captured by a trap. The Zeeman slower scheme [34], as it is called, has the disadvantage of being a large ($\sim$ 2 m, [32]), complex device that must be optimized for it to function properly. This is not the scheme used in this experiment.

Another possibility is to trap atoms directly in a region of space that is located in the presence of a certain background pressure of alkali vapor. This is called a vapor cell scheme [35] and was first realized as a simpler alternative to the Zeeman slower. This is the method that is used in our experiment. The trap itself is can be conceptually considered as a combination of six orthogonal and counter-propagating Zeeman slowers, but with a few key differences. This is the Magneto-Optical Trap (MOT), and will be briefly described here.

[3]Note, however, that the trapped atoms will be affected significantly by a desk lamp shining on a table near the experiment, owing to the much higher temperature of the filament. With this kind of stray light, the trap will empty in a few seconds. [33]

1.3.1 Optical molasses and the magneto-optical trap

Forgetting the magnetic field mentioned above for the moment, the time-averaged acceleration that a two-level atom undergoes when illuminated by a near-resonant laser is the product of the recoil velocity of a single photon absorption times the rate at which the atom absorbs photons (Equation 6.51, which will be derived in Chapter 6):

$$\langle a \rangle = \frac{\hbar k}{m} \times \frac{\Gamma}{2} \frac{I/I_s}{1 + I/I_s + 4(\Delta/\Gamma)^2}. \tag{1.15}$$

Here Γ is the full-width half maximum (FWHM) of the atomic transition's Lorentzian's lineshape, I is the intensity of the laser beam as seen by the atom, I_s is the saturation intensity of the transition and $\Delta = \omega - \omega_0$ is the detuning of the laser's frequency ω with respect to that of the atomic transition ω_0. The laser is red-detuned ($\Delta < 0$) with respect to the atomic transition's frequency, so that atoms encountering a counter-propagating beam will absorb photons at a higher rate than if they are traveling in the direction of the beam. Three orthogonal pairs of counter-propagating beams will create a region of space where they overlap in which an atom will feel a retarding acceleration proportional to its speed[4] no matter what direction it is traveling in [36]. This proportionality suggested the name *optical molasses* to describe this method of cooling, in analogy to the velocity-proportional retarding force a viscous fluid will exert on an object moving through it. Unfortunately, atoms cannot be cooled to arbitrarily low temperatures via optical molasses only. Eventually, the randomly-directed re-emission of absorbed photons jostles the atoms about at the Doppler temperature $T_D = \hbar\Gamma/2k_B$ for $I \ll I_s$ and $\Delta = -\Gamma/2$ [37]. In the case of ^{87}Rb, $T_D = 144$ μK.

The optical molasses scheme will cool atoms, but will not trap them. In order to trap the atoms as well, we would like to have each of the six lasers directed at the atom cloud push on the atoms only when the laser is approaching the cloud center, but not when it has passed it and is moving away. This can be achieved by exploiting the position-dependent Zeeman shift resulting from the presence of a suitable magnetic field.

Consider a simplified atomic manifold consisting of two hyperfine states: a single ground state with $F = 0$ and $m_F = 0$, and an excited state $F' = 1$ with three Zeeman-split sublevels $m_{F'}$ = -1, 0, 1.

Due to conservation of angular momentum, a photon that is σ^+ circularly polarized will interact only with the $|F = 0, m_F = 0\rangle \rightarrow |F' = 1, m_{F'} = +1\rangle$ transition, and a photon that is σ^- circularly polarized will interact only with the $|F = 0, m_F = 0\rangle \rightarrow |F' = 1, m_{F'} = -1\rangle$ transition.

In the presence of a magnetic field of z component $B(\mathbf{r})$, the Zeeman sublevels lose their degeneracy.

[4]The proportionality holds up to a certain speed, but thereafter is still retarding nonetheless.

The interaction Hamiltonian between a magnetic field **B** (taken along the z direction) and an alkali metal atom is

$$H = \frac{\mu_B}{\hbar}(g_S S_z + g_L L_z + g_I I_z)B_z(\mathbf{r}) \tag{1.16}$$

where S_z, L_z and I_z are the z axis projections of the electron spin, orbital angular momentum and nuclear spin; and g_S, g_L and g_I are the electron spin, electron orbital and nuclear Landé g-factors. If the energy shift induced by the magnetic field is small (below fields of around 300 G) the Zeeman energy shift of the hyperfine magnetic sublevels is linear in B and [24]

$$\Delta E_{m_F}(\mathbf{r}) = \mu_B g_F m_F B_z(\mathbf{r}) \tag{1.17}$$

where g_F is the hyperfine Landé g-factor and m_F labels the hyperfine magnetic sublevels.

In terms of frequency, the frequency of the $|F = 0, m_F = 0\rangle \rightarrow |F' = 1, m_{F'}\rangle$ transition is modified from ν_0 to [33]

$$\nu' = \nu_0 + \frac{\mu_B}{h} g_{F'} m_{F'} B_z(\mathbf{r}) \tag{1.18}$$

with $\mu_B/h = 1.4$ MHz/G. Note that the prefactor $g_{F'}m_{F'}$ determines whether the frequency of the particular transition increases with $B_z(\mathbf{r})$ ($g_{F'}m_{F'} > 0$) or decreases with $B(\mathbf{r})$ ($g_{F'}m_{F'} < 0$).

Consider the one-dimensional case of a magnetic field described simply as $B(z) = z\ \hat{\mathbf{z}}$. To the left of the origin ($z < 0$), the frequency of the transition to the $m_{F'} = +1$ state is lowered, whereas to the right of the origin, ($z > 0$) it is increased. If we red-detune a σ^+ polarized laser propagating from left to right, it will be closer to resonance with the $m_{F'} = +1$ state on the left than it is on the right. The scattering force this laser applies on atoms is thus greater when the laser is moving towards the trap center than when it is moving away.

Adding a second red-detuned laser coming from the opposite direction and σ^- polarized means that atoms will be driven to the $m_{F'} = -1$ state more strongly on the right side of the trap than the left. In the trap center, both light forces cancel out, leaving us with a restoring force that is zero at the trap center, and directed inwards with increasing magnitude as distance from the trap center increases. This is illustrated in Figure 1.1

Adding two more pairs of laser beams (directed such that the sum of their k-vectors is zero, which usually means orthogonally to the first pair) and using a quadrupole field of the form $\mathbf{B} = B_0(x, y, -2z)$ will result in a three-dimensional magneto-optical trap. In actual operation, the LANL BEC employs a trapping light detuning of about 13 MHz, compared to the transition linewidth of about 6 MHz.

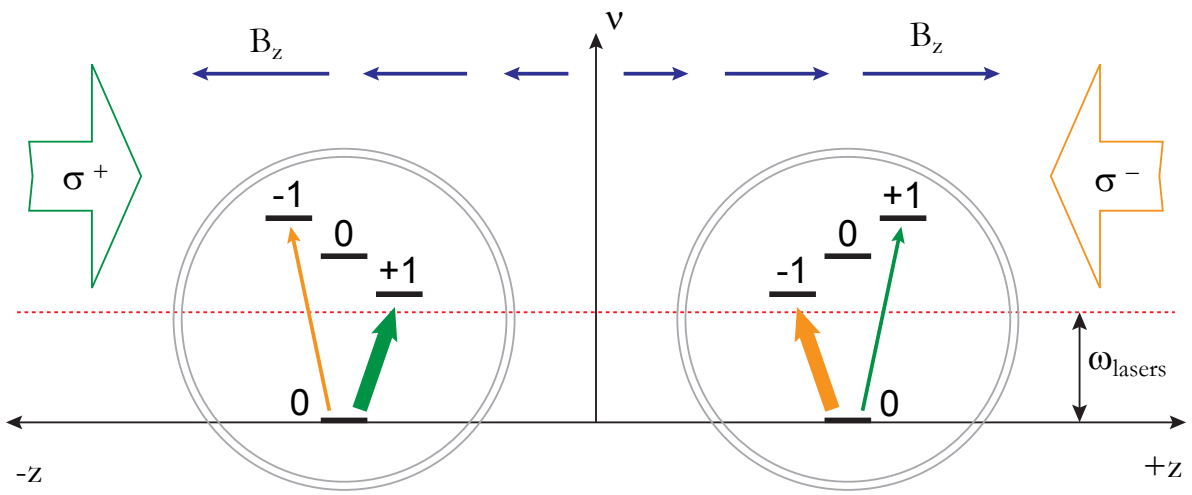

Figure 1.1: One-dimensional MOT example. Two counter-propagating beams red-detuned from the non-Zeeman-shifted $F = 0$ to $F = 1$ base frequency with circular polarizations σ^+ (green) and σ^- (red) exert a different scattering force on an atom on depending on what side of the trap it is on and how far it is from the center of the trap. The thickness of the arrow linking the ground state to the excited state represents the strength of the light pressure exerted by the beam of corresponding color.

In practice, the level scheme is not so simple. The transition used in the LANL BEC experiment for cooling and trapping is part of the D2 line, which is from the $5^2S_{1/2}$ manifold to the $5^2P_{3/2}$ manifold; specifically, from the F=2 to F'=3 hyperfine levels (see Figure 1.2). The added complexity of the D2 line manifolds has a consequence that has yet to be accounted for. Trapping light that is red-detuned from the F=2 to F'=3 levels is still close enough to the F'=2 level to drive the F=2 to F'=2 transition at a very low rate. Apart from decaying into the F=2 state, atoms can decay from the F'=2 state into the F=1 ground state, where they no longer interact with the trapping laser. An additional laser driving the F=1 to F'=2 transition is overlapped at low intensity with the trapping light, and this prevents the trapped atoms from eventually all falling into an untrappable state. This is called the repump laser.

One interesting thing worth knowing about MOTs is that the total number of atoms they capture and hold is not dependent on the background pressure, as long as the background pressure is dominated by the element being trapped. If that element is rubidium, this is called the rubidium-dominated regime. What *does* depend on the background pressure, however, is the rate at which the trap can capture atoms from the surrounding vapor [33]. This loading rate is experimentally very relevant, since a slow loading rate will result in an experiment that takes a long time to repeat. On the other hand, once the atoms have been cooled in the dissipative MOT, they are held in a conservative magnetic potential and subsequently transferred to an all-optical dipole potential as part of the several steps required for

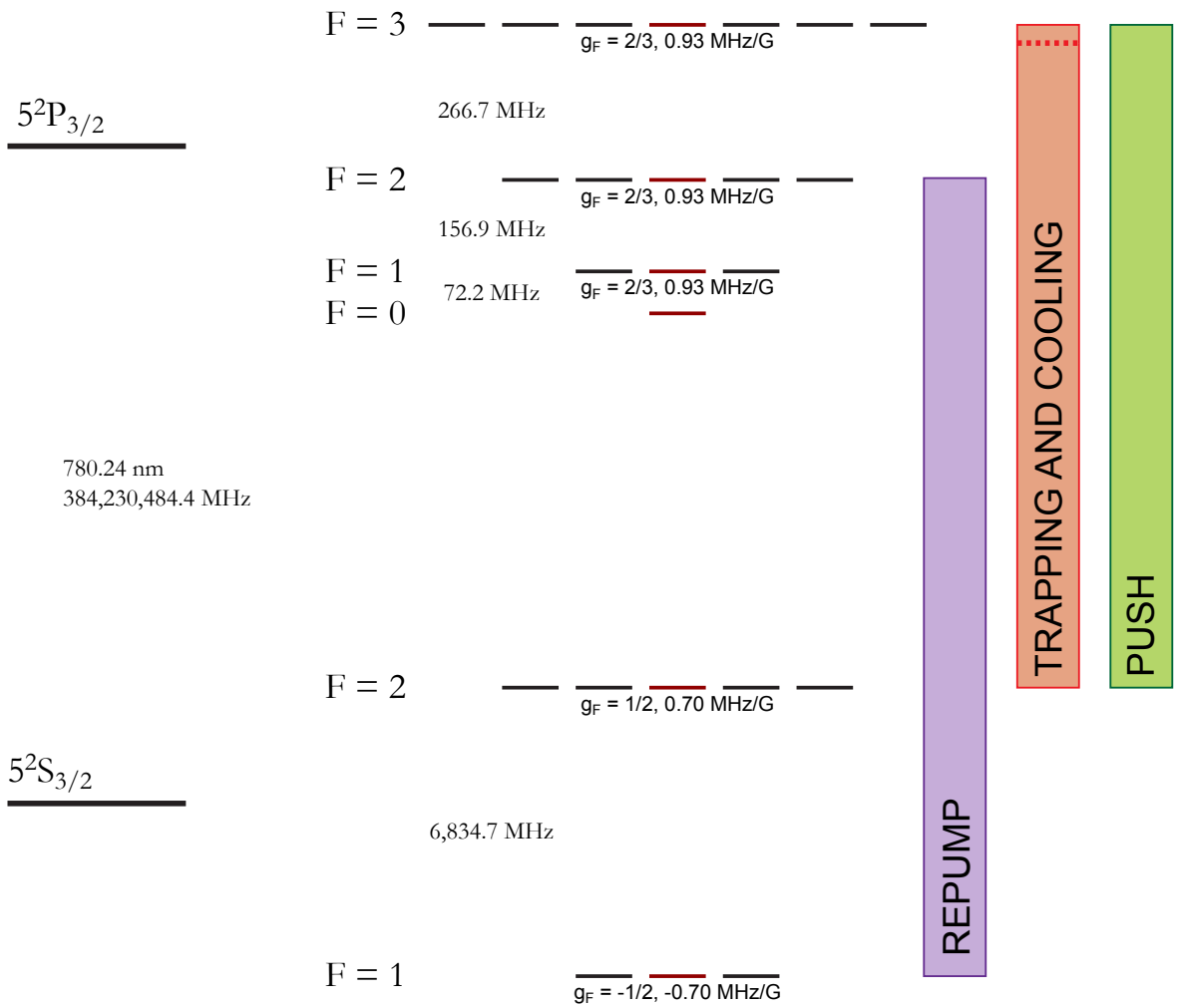

Figure 1.2: ^{87}Rb level scheme for the D2 line. Shown are the hyperfine sublevels of the $5^2S_{1/2}$ ground state and $5^2P_{3/2}$ excited state, along with their Landé g-factors and the Zeeman splitting for the magnetic sublevels (a numerical value for $g_F\mu_B/h$ in MHz/G). Shown also are the transitions used for repumping; trapping and cooling, and the push beam which transfers the atoms from the HP to the LP MOT. Data from [38, 39] via [40].

achieving BEC. When the cold atom cloud is in these conservative potentials, it is very susceptible to collisions from background gas, whatever its type may be. If the collisional rate with background gas is too high, atoms will be knocked out of the trap, and the trap will eventually empty.

The conflicting requirements of a relatively high background pressure of ^{87}Rb for trap loading and low background pressure overall for BEC achievement appear irreconcilable. One solution is to design the experiment around *two* MOTs [41]. The first, or high pressure (HP) MOT, exists in a rubidium-

dominated regime that leads to fast trap loading times. The cold atoms in this trap can then be sent by some method to a low pressure (LP) trap, where they can then be further cooled in an environment where background gas collisions do not render the trap lifetime too short to be useful. This is the setup used in the LANL BEC experiment. The atoms that are collected and cooled in the HP MOT are pushed by a near-resonant laser beam to the LP MOT tens of times per second. This results in both fast loading times and a good initial atom number in the LP MOT.

1.3.2 Magnetic trapping and forced RF evaporation

It is possible to cool atoms further than the Doppler limit, as long as the local magnetic fields are kept low, below the Earth's field [42, 43], such that the atoms are Zeeman-degenerate. Though we will not describe these sub-Doppler processes here, a good overview can be found in [44]. The theoretical limiting temperature is simply the recoil temperature of an atom that has absorbed a single photon, $T_R = \hbar^2 k^2 / k_B m$. Though this temperature for ^{87}Rb and 780 nm light is about 360 nK, in practice only temperatures about ten times this value can be achieved [45].

At this point, the atoms cannot be cooled further by optical means, since this ultimately means having them interact with momentum-carrying photons. A different approach is required to further cool the atoms. If the hottest atoms could be selectively removed from the atom cloud then, after rethermalization, the cloud's average temperature would drop. To do this, the atoms must be first held in a conservative magnetic trap, as opposed to a dissipative, laser-bathed MOT.

Recalling the energy shift of a hyperfine magnetic sublevel in the presence of a magnetic field (Equation 1.17), we see that it is possible to have a position-dependent energy shift that increases as the atom moves towards higher field. This will be the case as long as the sign of $g_F m_F$ is positive, since these states lower their energy as the field becomes weaker. They are thus called weak field seeking states. If an inhomogeneous magnetic field can be set up in space such that there is a local minimum, weak-field-seeking states will see a potential energy gradient towards this location. As with the MOT, a quadrupole field satisfies this requirement. Indeed, the coils that provided the quadrupole field for the LP MOT now provide the quadrupole field for the magnetic trap (these coils, called anti-Helmholtz coils, will be described in Chapter 3). The significant difference, however, is that here the trapping potential arises from a magnetic field gradient, whereas in a MOT, the potential is a result of a position-dependent scattering force. Consequently, the currents required to generate the quadrupole field for a MOT and for a magnetic trap are very different in magnitude, the latter being larger.

To selectively remove atoms from the atom cloud, an RF field of frequency ν_{RF} set up in the vicinity

of the LP MOT cell will drive transitions between hyperfine sublevels if the RF frequency matches the frequency of the transition between Zeeman sublevels, that is, $\nu_{\mathrm{RF}} = \Delta E_{m_F}(\mathbf{r})/h$ [46]. Since $\Delta E_{m_F}(\mathbf{r})$ is proportional to the magnitude of the magnetic field (which is strongest away from the trap center), starting at a high RF frequency and ramping down will result in atoms being flipped into strong-field-seeking states in an ellipsoidal surface that closes in on the trap center from the outside. The flipped atoms escape the trap immediately, because they have been converted from weak field seeking states to strong field seeking states, and since the hottest atoms are most likely to be found on the outside surface of the trap, this method is effective at getting rid of the hottest atoms.

The key to this method working successfully is how fast the truncated Boltzmann thermal distribution can rethermalize via elastic collisions. If this does not happen fast enough, the loss processes that are constantly causing the trap to lose atoms (inelastic collisions among trapped atoms and collisions with background gas) dominate the process, and the trap empties before the atoms can be cooled significantly.

To speed up the rethermalization process, the magnetic trap is made tighter by increasing the current flowing through the anti-Helmholtz coils. Care must be taken not to heat the trapped atoms by tightening the potential too abruptly, so this process must be done adiabatically.

There is one other loss mechanism that is intrinsic to the use of a magnetic trap with zero magnetic field at its center, as is our case. As the trapped atoms become denser and colder in the magnetic trap under RF evaporation, the proportion of atoms lost to this mechanism, called Majorana losses [47], can become significant [48]. An atom is magnetically trapped only if the atom's magnetic moment can follow the direction of the local magnetic field adiabatically, with its spin axis precessing around the local magnetic field vector. If the rate of change of the magnetic field becomes comparable to the Larmor precession frequency of the magnetic moment around this magnetic field vector, the atom can flip into a non-trapped state. Near the center of the quadrupole trap, the field changes direction quite abruptly from the point of view of an atom traveling through or near it. The center of the trap becomes a hole from which atoms leak into non-trapped states, and at low temperatures and high densities, as encountered during forced RF evaporation, atom losses will put an end to progression towards BEC.

There are different approaches to tackling this issue. Instead of a purely quadrupole magnetic field, alternative versions with nonzero local magnetic field minima have succesfully been used for BEC, such as the time-orbiting potential [6, 48], and Ioffe-Pritchard [49] traps. The first makes use of a time-varying magnetic field whose hole changes position cyclically with time, at such a rate that the atoms are confined to the center of the time-averaged potential. The second is static, but has a non-zero field minimum, and generally produces elongated, ellipsoidal atom clouds [33]. The latter is what the

Sussex-era LANL BEC machine used.

1.4 Optical dipole traps and painted potentials

Another alternative is to plug the Majorana loss hole with a blue-detuned repulsive laser beam. This approach is called an optical plug [7], and was briefly considered for the LANL BEC. A different approach, which is used in the LANL BEC system, is similar to that taken by Lin et al. in their 2009 publication "*Rapid production of* ^{87}*Rb Bose-Einstein condensates in a combined magnetic and optical potential*" [50]. Instead of plugging the Majorana hole, atoms are RF evaporated in a magnetic trap as usual until the point at which Majorana losses become unacceptable. At this point, the atoms are carefully released into an optical dipole potential (described below) that matches the trapping frequencies of the magnetic trap. One advantage of this approach is that adiabatically changing the trap shape from linear quadrupole (as is produced by the anti-Helmholtz coils) to harmonic (as is the case with an optical dipole potential) actually increases the phase space density of the atom cloud, giving it a boost on the path to BEC [50]. Gradually reducing the dipole beam's intensity reduces the optical trap depth and, in the same way in which RF evaporation results in the removal of the outermost, hotter atoms from the trap, this forced evaporative cooling ultimately leads to condensation.

1.4.1 Optical dipole potentials

An optical dipole potential—whether it is repulsive as in the case of the optical plug or attractive, as in the case of the trap used in the final evaporation stage, mentioned above—arises as a result of the interaction potential between the induced dipole moment $\mathbf{p}$ of an atom and an applied laser electric field $\mathbf{E}$ of frequency ω. In the semiclassical approximation, if they are defined as

$$\mathbf{p}(\mathbf{r},t) = \hat{\mathbf{e}}\tilde{p}(\mathbf{r})\exp(-i\omega t) + \text{ c.c.} \tag{1.19}$$

$$\mathbf{E}(\mathbf{r},t) = \hat{\mathbf{e}}\tilde{E}(\mathbf{r})\exp(-i\omega t) + \text{ c.c.} \tag{1.20}$$

with $\hat{\mathbf{e}}$ the unit polarization vector, then $\tilde{p}$ given simply by $\tilde{p} = \alpha(\omega)\tilde{E}$, where $\alpha(\omega)$ is the complex polarizability. The interaction potential of the induced dipole moment is then [51]

$$U_{\text{dipole}}(\mathbf{r}) = -\frac{1}{2}\langle \mathbf{p}\cdot\mathbf{E}\rangle = -\frac{1}{2\epsilon_0 c}\text{Re}(\alpha)I(\mathbf{r}) \tag{1.21}$$

where the time average has been taken. In Chapter 6 we will derive the atomic polarizability for a two-level atom (Equation 6.47). This expression can be written in a form that is more useful here,

however.[5] In terms of the atomic linewidth Γ and the detuning $\Delta = \omega - \omega_0$, with ω_0 the atomic transition frequency, the real part of the complex polarizability is

$$\text{Re } \alpha(\omega) = -\frac{3\epsilon_0\lambda^3}{4\pi^2}\frac{\Delta/(\Gamma/2)}{1 + I/I_s + 4(\Delta/\Gamma)^2} \tag{1.22}$$

where I_s is the transition's saturation intensity. In the far-detuned case, saturation of the transition is negligible, and $|\Delta| \gg 1$. In this case, then, the optical dipole potential can be written as

$$U_{\text{dipole}} = \frac{3\pi c^2}{2\omega_0^3}\frac{\Gamma}{\Delta}I(\mathbf{r}). \tag{1.23}$$

Note that the sign of the detuning determines the sign of the potential. A red-detuned laser, with $\Delta < 0$, will form an attractive potential, whereas a blue-detuned laser will form a repulsive one.

An important consideration is the rate at which an atom in a far-detuned beam will scatter photons. In the same semiclassical approximation, it is [51]

$$\Gamma_{\text{scatt}} = \frac{3\pi c^2}{2\hbar\omega_0^3}\left(\frac{\Gamma}{\Delta}\right)^2 I(\mathbf{r}). \tag{1.24}$$

One notices immediately that whereas the potential scales as Γ/Δ, the scattering rate scales as $(\Gamma/\Delta)^2$. In other words, optical dipole potentials require large detunings to keep the scattering rate low, but high intensities to compensate and achieve a required potential depth. The wavelength of the optical dipole potentials used in the LANL BEC experiment are far from the 780 nm of the ^{87}Rb D2 transition. The light sheet employs 1064 nm light, and the tweezer beam uses 830 nm. Δ for 830 nm light with respect to the 780 nm transition is on the order of $\Delta \sim 10^{13}$.

Optical dipole traps offer several advantages over purely magnetic traps for BEC formation and holding. They are generally not state-dependent[6], unlike magnetic traps, that can only form BECs in states that can be magnetically trapped. More importantly, at least from the point of view of the experimental mission of the LANL BEC, optical dipole traps do not have to be stationary. They can be rapidly moved, tracing out a time-averaged optical potential for the condensed atoms.

1.4.2 Painted optical potentials

Currently all experimental research carried out on the LANL BEC machine makes heavy use of time-averaged optical dipole potentials. Two beams provide the all-optical three-dimensional trapping required for experiments: a static horizontal light sheet, produced by rapidly scanning a red-detuned

[5] Via Equations 6.48 and 6.48.

[6] If the dipole beam used for trapping is linearly polarized and the beam's detuning is much larger than both the excited and ground state Zeeman sublevel splitting—and in the case of the LANL BEC, it certainly is—then the potential can be considered independent of quantum numbers F and m_F [51].

beam back and forth in the horizontal plane, and a vertical tweezer beam, scanned vertically through this plane following an arbitrary, cyclical path with total control over beam power. With this combination, pseudo-2D potentials in the shape of toroids, squares, grids and so on can be generated [52]. Potentials are created by providing an arbitrary waveform generator (AWG) with instructions from a user-created computer program. The AWG reproduces the required RF signals that drive x and y deflecting accousto-optical modulators (AOMs). These AOMs deflect and control the power of the tweezer beam as it is rastered through the light sheet, allowing time-varying arbitrary potentials to be created. Generally speaking, the condensed atoms will see a time-averaged potential as long as the scanning frequency of the beam is about 10 times the trapping frequency.

1.4.3 The Physics of BEC: Closing remarks

This Chapter should have provided enough background on the creation of BECs to allow a general understanding of how the systems described in subsequent chapters fit together in the day-to-day operation of the LANL BEC machine. For a much more in-depth examination of the physics involved, the reader is directed to the theses of Aidan Arnold [33] and Calum MacCormick [53], who completed their PhD theses while part of Dr Boshier's group.

1.5 Thesis outline

This Thesis documents design and construction work performed in support of the Bose Einstein Condensate experiment operated by Dr Malcolm Boshier and Dr Changhyun Ryu at the Los Alamos National Laboratory, Group P-21 in Los Alamos, New Mexico, from the Summer of 2009 through to the Spring of 2012.

In 2009 it was decided that an all-new BEC machine would be constructed to operate in parallel to the existing experiment, first constructed at the University of Sussex in the mid 90s and used to create the first BEC in the United Kingdom in 1998 [33]. This plan progressed until October 2010, when an insulation failure on the low-pressure (LP) section magnetic coils spurred the re-purposing of that which had been designed and built so far (the magnetic subsystem, Chapter 3; the laser subsystem, Chapter 4; and the magneto-optical trap beam expanders, Chapter 5). Construction of a single, entirely new BEC machine became the priority, and this new machine first achieved BEC in 2011.

The main design objectives for the new machine were the ability to attain BECs with more atoms

in a shorter period of time than what was possible previously. Larger diameter MOT beams with more power available to them, a tighter magnetic field gradient on the low pressure system end and an improved pressure ratio between the high pressure and low pressure ends of the experiment account for the improved BEC size and experimental cycle time.

Stability and robustness were also sought, and the main contribution to these objectives comes from the use of a single-mode fiber optic system that keeps beam path lengths—and the corresponding amount of adjustable optics involved—at a minimum, compared to what would be required if fully free-space optics and beam periscopes were employed. A different kind of insulation was used on the LP magnetic coils, hopefully preventing another short circuit in the distant future.

The pursuit of more demanding scientific objectives also motivated the adoption of a quartz cell (inside which the BEC is formed and manipulated) with improved optical quality, as well as a motorized tweezer beam focus adjustment stage.

The structure of the Thesis is as follows.

Chapter 1, this Introduction, has given a brief overview of the wide-ranging physics involved in achieving Bose Einstein Condensation. It is not intended to be an authoritative reference on the topic, but rather enough basic information for a reader with a good physics background to make sense of the purpose of the systems described in the following chapters. References are provided for further study and information.

Chapter 2, "Quartz Cell and Vacuum System", provides an overview of the quartz cell that provides access to the BEC, as well as the new vacuum system design. It is noted that design of the a large part of the vacuum system was not the author's own work, but it is included for completeness.

Chapter 3, "Magnetic System" describes the magnetic coils and their associated support mechanisms that were designed for the new apparatus.

Chapter 4, "Laser System" covers the lasers used in the experiment, from their locking, to the system used to divide the beams into many fiber-coupled sub-beams.

Chapter 5, "Optics" goes over the optics used to expand the fiber-coupled sub-beams into large-diameter, collimated beams used for magneto-optical trapping.

Finally, Chapter 6, "Phase Contrast Imaging" is a feasibility study on whether or not a non-destructive imaging method could be used on the LANL BEC experiment in future.

Before the reader progresses any further, it is probably a good idea that they familiarize themselves with the general layout of the BEC machine, shown in Figure 2.3 on page 23. It will provide a useful visual reference for the location of the rest of the subsystems discussed in this Thesis.

Chapter 2

Quartz cell and vacuum system

Shortly after the failure of the old Sussex-era LP MOT coils, it was decided that the entire vacuum system would be overhauled. A new glass cell was designed and ordered (Section 2.1) and an all-new vacuum chamber system was built (Section 2.2), along with new alkali metal vapor sources (Section 2.3). This Chapter focuses on the aspects on which the author made a substantial contribution, but it should be noted that group member Alina Blinova was heavily involved in the design of the new vacuum system (essentially, everything but the quartz cell), and was entirely responsible for its assembly and bakeout.

2.1 Quartz cell design

The quartz cell used in the Sussex BEC machine was hand-blown and thus not of excellent optical quality [33]. After serving the purposes of all experiments undertaken up to 2010, a new cell with better optical quality was needed for the more demanding experimental goals that were anticipated. Quotes were requested from Hellma USA for a spade-shaped design that mimicked the Sussex quartz cell (model 221-402-VY) and for a cuvette-style design (model 221-403-VY, Figure 2.4), both manufactured from Vycor quartz. The cuvette style was ultimately chosen. The section of high optical quality is 125 mm long on the outside and 30 mm in square cross section. The thickness of the quartz is 2.5 mm throughout. The entire cell, from tip to the outer face of the flange, is 245 mm long.

The cell was designed to be 120 mm long on the inside, a length that would easily accommodate MOT beams crossing at 45° angle of incidence, but when it was determined that the beams would have

to be crossed at a shallower angle (see Section 3.2), a simple geometrical analysis (Figure 2.1) shows that for an obliquely-incident MOT beam of width w_b and angle of incidence α from the surface of the cell, and a cell of height w_c, the minimum length for clear passage of the beam is

$$l = \frac{w_c}{\tan\alpha} + \frac{w_b}{\sin\alpha}. \tag{2.1}$$

The minimum length required for an oblique incidence angle of 29°, as is the case with the new LP MOT design, requires a cell length of about 91 mm, a figure that is within the 120 mm avilable.

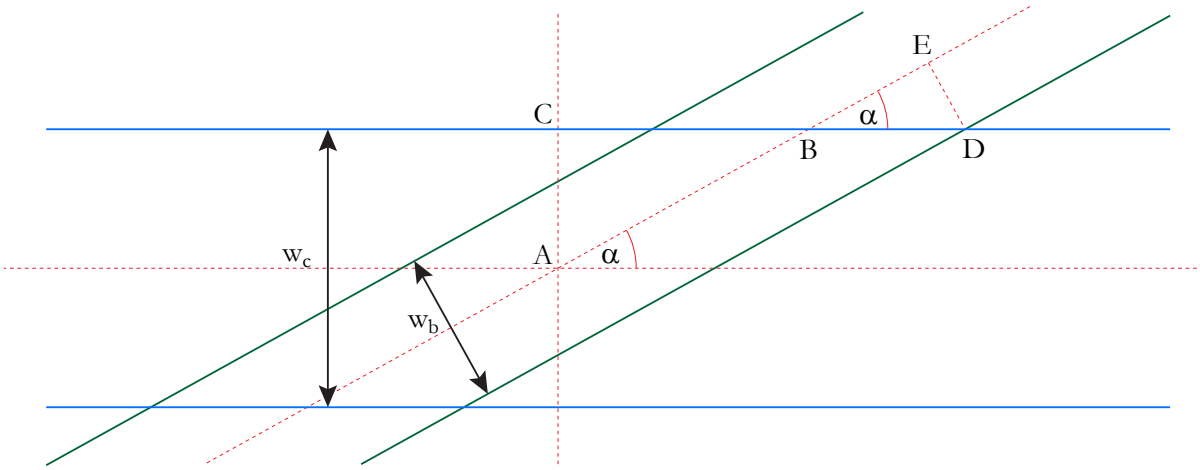

Figure 2.1: Calculation of minimum cell length for a given beam width w_b, cell width w_c and beam incidence angle α. A schematic LP MOT beam (green) incident on the quartz cell (blue) at an angle α is required to pass through the trap center **A**. To do this, the cell must be at least twice the length of segment $\overline{CD}$, to avoid distortion from cell corners and/or edges. The length of $\overline{CD}$ is calculated from segments $\overline{CB}$ and $\overline{BD}$. $\overline{CB} = (w_c/2)/\tan\alpha$ by right angle triangle ABC and $\overline{BD} = (w_b/2)/\sin\alpha$ by right angle triangle BDE.

The cell was mounted on the assembled vacuum system, and the system was baked and pumped out. It was only after a few weeks, with the new system already mounted on the optical table, that it was noticed that the quartz cell was apparently rotated about its long axis with respect to the mounting bolts. This would prove problematic if left uncorrected, since the BEC is created in a horizontal light sheet, and since the light sheet must be perpendicular to gravity, this would inevitably result in non-normal angles of incidence on the cell faces, with the corresponding possibility of interference and multiple reflections (the cell is not anti-reflection coated, unlike the vacuum system viewports).

An attempt to quantify this rotation was made by means of a digital photo, since extreme care was taken at all times not to touch the cell. This ruled out any form of contact-based measurement. This image was taken at the greatest optical telephoto setting and subject-camera distance that allowed a

complete view of the vacuum system. Measurements were taken by superimposing vector markers with Adobe Illustrator CS4 and measuring their position relative to each other. Figure 2.2 enumerates the measurements that were taken.

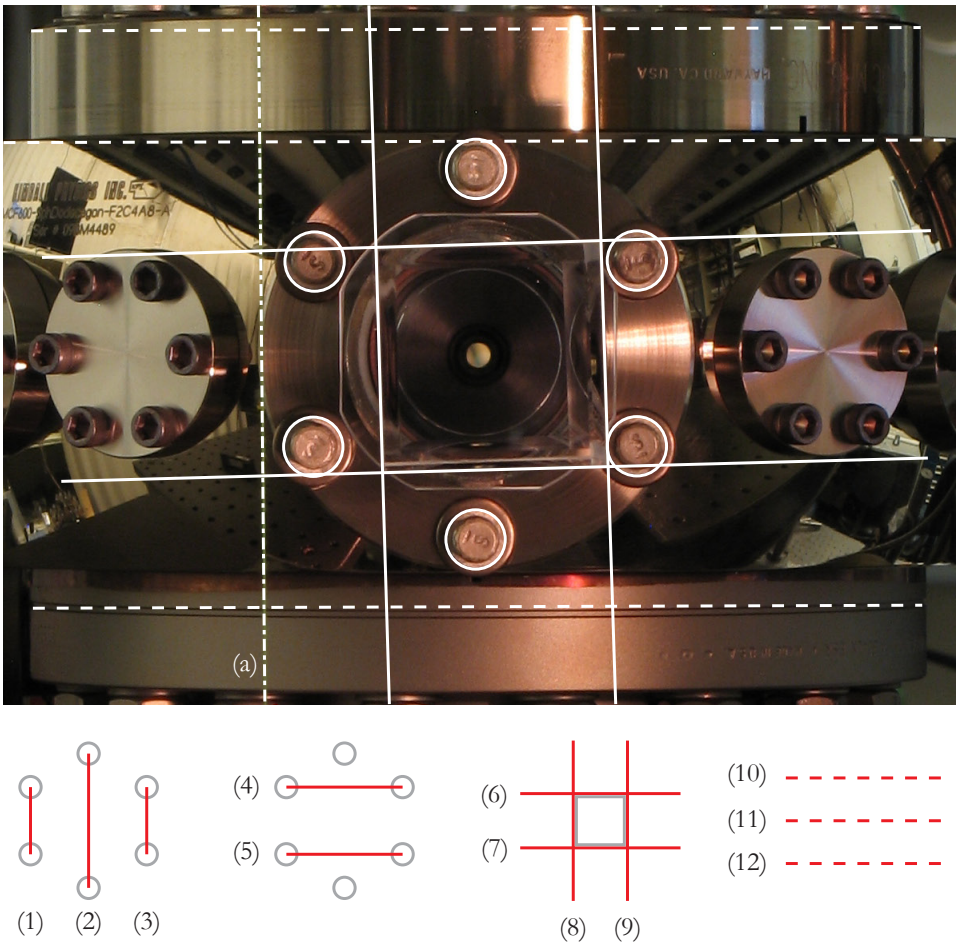

Figure 2.2: Measurement of the rotation of the 221-403-VY quartz cell. A digital photograph originally measuring 3072 by 2304 pixels was taken. Shown is a cropped area and the graphical markers that were overlaid on the image. 12 angular measurements were made, corresponding to bolt alignment positions, cell rotation and the vacuum system reference angle. A thread was hung from above the vacuum system to be able to compare all angles to gravity **(a)**. Note that in the case of the cell, the marker lines were extended beyond their original point of measurement for clarity. Note also that the constriction tube between the HP and LP ends of the system can be seen at the center of the picture, showing a clear view along the push beam's axis.

Owing to the different baselines of all 12 angular measurements, it is prudent to check what angular deviation a 1 pixel error in marker placement will result in. The worst affected, owing to their short

Objects Compared	Magnitude of Relative Rotation (°)
Bolts/Vacuum system	0.04 ± 0.06
Cell/Vacuum system	1.51 ± 0.1
Cell/Bolts	1.54 ± 0.1
Thread/Vacuum system	0.34 ± 0.04
Thread/Cell	1.16 ± 0.1

Table 2.1: Magnitude of relative rotation between various system components. Note that, to within the calculated error of these measurements, the bolt flange and the vacuum system are aligned.

baselines, are the bolt and the cell measurements, at $\pm 0.12°$ and $\pm 0.20°$ respectively. The vacuum system reference lines and the hanging thread fare better at $\pm 0.05°$ and $\pm 0.03°$ respectively.

All angular measurements near 0° degrees were rotated by 90° to facilitate comparison. In this way, bolt measurements 1 to 5 were averaged, as were cell measurements 6 to 9 and vacuum system measurements 10 to 12. All estimated errors were added in quadrature.

Table 2.1 summarizes the magnitudes of the relative rotation between system components. From this we can conclude that the cell is indeed rotated by about 1.5° with respect to the vacuum system, and about 1° with respect to gravity.

Since we expect the tolerance in the machining of the vacuum system with respect to the flange bolts to be of a precision higher than that discernible with the present measurement method, the agreement between independent the bolt and vacuum system measurements is reassuring. This would indicate that the quartz cell is rotated on its mounting flange. Communication with Hellma USA (and through them, Hellma Gmbh) resulted in a plausible explanation for this discrepancy: standard manufacturing rotation tolerances for cell/flange joints are ±5° unless a lower tolerance is requested. Since a lower tolerance was never requested, our version of model 221-403-VY was provided rotated.[1]

The small but measurable discrepancy between the direction of gravity as measured by the hanging thread and the vacuum system orientation ($0.34 \pm 0.04°$) is most likely due to the fact that the whole system rests on two long sections of Unistrut steel frame (assuming a perfectly level optics table). Considering the separation between the two rails (5 in = 127 mm), the inclination of the vacuum system could be explained by a height difference between Unistrut segments of as little as $127 \times \sin(0.34°) = 0.75$

[1] A backup cell was also ordered with the main cell—just in case—and this, too, was measured via a similar method. It was found that the quartz cell was rotated by $1.5° \pm 0.1$ with respect to the flange bolt holes.

mm, which is certainly feasible.

After performing these measurements, the entire system was shimmed by placing thin pieces of metal under one of the Unistrut segments. This successfully addressed the problem.

2.2 Vacuum system overview

The LANL BEC machine, like its Sussex-originated predecessor, is a double MOT system. See Figure 2.3 for an overview of the system. In the high pressure side of the system, ^{87}Rb is evaporated from a metallic source (described in Section 2.3), allowing a rapid filling of the HP MOT. The low pressure end, however, is kept at a much lower pressure by a physical constriction (Figure 2.3, inset). In the case of the LANL BEC, in addition to a tighter constriction, a pump system with a significantly larger effective pumping speed than that which was used on the Sussex BEC is used. These two characteristics are the key vacuum-related improvements that allow a much higher HP/LP pressure ratio to be maintained. As a result, faster filling of the HP MOT is now possible, resulting in a better experimental duty cycle, while maintaining the good LP vacuum level of about 10^{-11} Torr required for a long-lived LP MOT.

At UHV/XHV pressures (on the order of 10^{-11} Torr) the system is well into the molecular regime, where the mean free path of atoms and molecules is so large that their trajectories through the interior of the system are effectively purely ballistic. Upon hitting a chamber wall, they do not bounce, but rather adsorb for a short period of time, and are then sent off in a random direction following a cosine rule. The calculation of how volumes of particles move from one section to another in a vacuum system in this regime is essentially one of geometry. Indeed, the quantity that characterizes the way in which a tube or duct affects the transmission of molecules through it is called *conductance*, and has dimensions of volume per unit time. The conductance of an aperture of area A for molecules or atoms of molar mass M_m at temperature T is [54]

$$C_A = A\sqrt{\frac{RT}{2\pi M_m}} \tag{2.2}$$

where R = 8.314 J/mol/K is the universal gas constant. If we wish to include the effect of the tube or duct that lies behind said aperture, its aperture conductance is multiplied by a transmission probability α. In the case of a long tube of diameter d and length l, α_{tube} can be represented by a series,

$$\alpha_{\text{tube}} = \frac{4d}{3l} - \frac{1}{2}(d/l)^2 \log(2l/d) \cdots , \tag{2.3}$$

the first two terms of which are accurate enough for our purposes.[2]

[2]For $l/d \sim 10$, the second term is about 10% of the first.

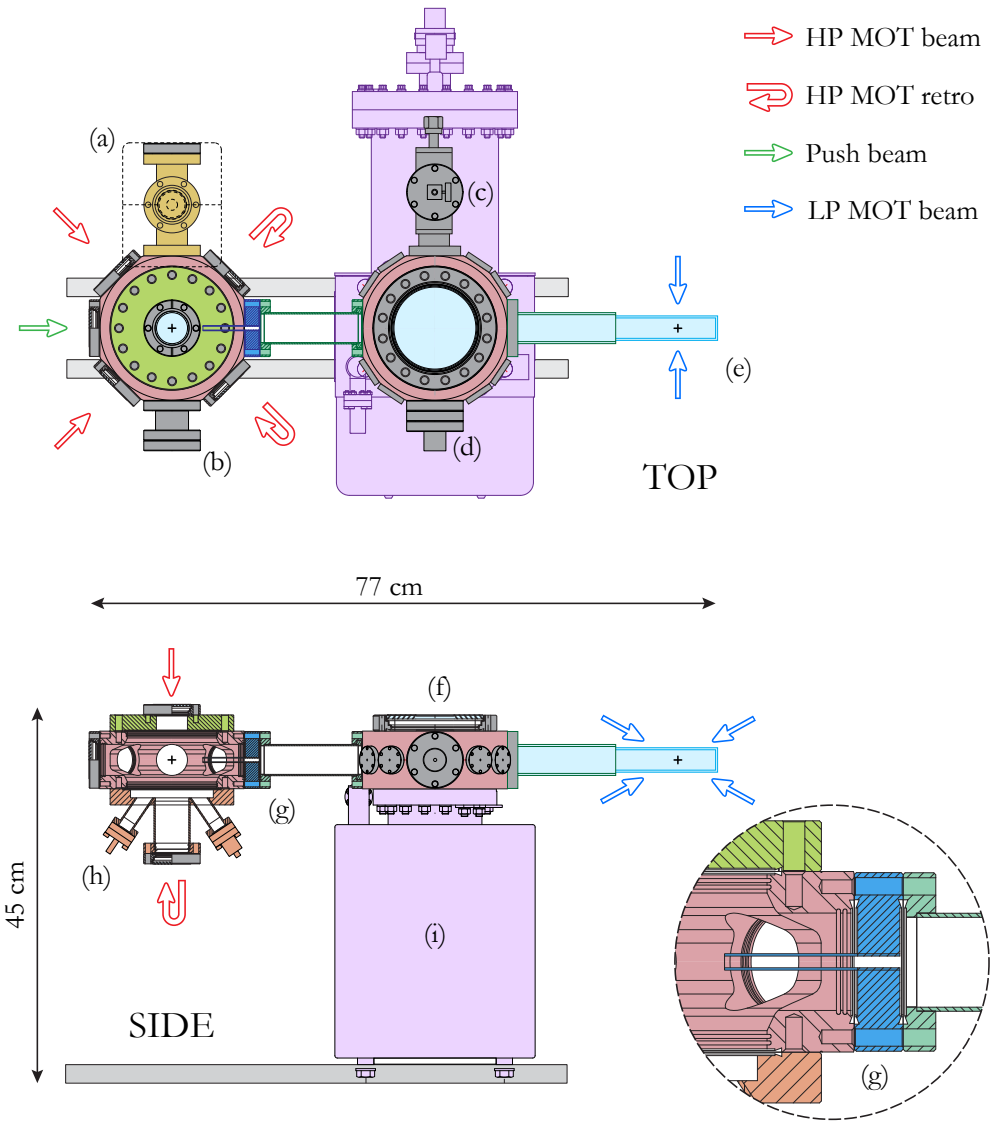

Figure 2.3: Overview of vacuum system. The entire apparatus rests on two lengths of Unistrut rails. It is pumped out by two vacuum pumps: a Varian StarCell 20 **(a)** and an Agilent VacIon assembly **(i)**. Ion gauges are fitted at **(b)** and **(d)**, but only the latter is used. The bakeable valve used to rough the system is at **(c)**. The quartz cell is at **(e)**. A large-diameter viewport was placed on top of the VacIon 150 assembly at **(f)**. A constriction tube, vital to maintaining the pressure difference between the HP and LP ends, is shown in detail at **(g)**. The alkali metal sources are installed in each of the six arms of the bottom source holder **(h)**. The smaller vacuum pump **(a)** has been omitted from the side view for clarity, as has the bakeable valve **(c)**. Technical drawings from MDC, Kimball and Agilent used with permission.

Species	Sussex conductance (l/s)	LANL conductance (l/s)
^{87}Rb	1.9	8.4×10^{-2}
H_2	12.8	5.5×10^{-1}

Table 2.2: Constriction tube conductances for ^{87}Rb and H_2 for the Sussex and LANL BEC systems (calculated).

If vacuum system elements of conductances C_1 and C_2 are connected in series, the total conductance C is given by

$$\frac{1}{C} = \frac{1}{C_1} + \frac{1}{C_2}. \tag{2.4}$$

Note that this effectively means that if several vacuum system ducts and apertures are connected in series the total conductance will never be larger than the smallest conductance involved, and will generally lie close to this value. As an illustration, whereas two tubes of 10 l/s conductance in series behave like a single 5 l/s conductance tube, increasing the conductance of one of them to 100 l/s will only bring the total conductance up to 9 l/s or so.

In the Sussex BEC, the HP side of the vacuum chamber had no pump, and therefore this region was pumped through the constriction tube by a Varian StarCell 20 l/s ion pump, mounted on the LP side. In the LANL BEC, this same StarCell pump is installed on the HP side, but is generally not in use. The LP side is pumped by a VacIon 150 Triode ion pump and a titanium sublimation pump, both of which are housed in the same assembly (labeled **(i)** in Figure 2.3) and connected to the LP side by an 8 inch conflat flange. As a result of these analogous configurations, the HP/LP pressure ratio can be compared between the Sussex and LANL machines. Table 2.2 summarizes the conductances of each system's constriction tube for ^{87}Rb and H_2.

To calculate the theoretical pressure ratio attainable between the HP and LP ends of the system, it is first necessary to define the flow rate of a gas as a *throughput* $\dot{Q} = PS$, where S is the volumetric rate, or speed, of the gas being evacuated, and is measured in liters per second. With this definition, the conductance of an object placed between an upstream region of pressure P_u and a downstream region of pressure P_d is

$$C = \frac{\dot{Q}}{P_u - P_d}. \tag{2.5}$$

In a steady state situation, the throughput from the HP to the LP chambers, $\dot{Q}_1$ must be equal to

the throughput from the LP chamber to the LP vacuum pump, $\dot{Q}_2$. We have

$$\dot{Q}_1 = (P_{\mathrm{HP}} - P_{\mathrm{LP}})C_{\mathrm{tube}} \tag{2.6}$$

$$\dot{Q}_2 = P_{\mathrm{LP}} S_{\mathrm{pump}} \tag{2.7}$$

and the ratio of the HP to LP chamber pressures is

$$\frac{P_{\mathrm{HP}}}{P_{\mathrm{LP}}} = \frac{S_{\mathrm{pump}}}{C_{\mathrm{tube}}} + 1. \tag{2.8}$$

Though Equation 2.8 should refer to the *effective* pumping speed S_{eff} once all pump flanges and geometrical factors that affect a pump's speed are considered, the fact that the ion pump (rated at 150 l/s) and Ti sublimation pump (rated at about 1200 l/s for H_2 and just over 500 l/s for N_2) are located a short distance behind an 8 inch diameter flange (of aperture conductance of over 3700 l/s) justifies neglecting the flange's effect. For molecular hydrogen, then, the pressure ratio $P_{\mathrm{HP}}/P_{\mathrm{LP}}$ is on the order of 2×10^3, whereas the Sussex ratio is about 2.5.[3] In summary, an improved constriction tube and better LP pumping result in about a thousandfold improvement in the HP/LP pressure ratios. In practice, we expect the pressure ratio for Rb to be even higher, given its tendency to adsorb for relatively long times on stainless steel. [55]

In practice (as of Spring 2012, at least), the actual pressure ratio is not maintained as high as it could be, mainly because the HP end is also being pumped. A pressure ratio $P_{\mathrm{HP}}/P_{\mathrm{LP}}$ of about 10 provides adequate experimental cycle times and trap lifetimes, though the latter have yet to be measured precisely.[4]

2.3 Alkali sources

The Rb source used in the Sussex system provided natural Rb, composed of 72% ^{85}Rb and 28% ^{87}Rb according to these isotope's natural abundance in a ratio of 1:2.6. Due to collisional processes in the MOT, however, in practice only about 1.5 times the number of ^{85}Rb atoms relative to ^{87}Rb were collected [33]. During the design phase of the new LANL BEC machine it was decided that isotopically pure sources of ^{87}Rb would be used. In addition to ^{87}Rb, the multi-feedthrough base of the HP chamber was put to good use by loading four other species, in anticipation of future experiments. These sources, manufactured by Alvatec, contain only the required species sealed in an Ar environment behind an In seal. This seal is melted only once during the initial pumpdown phase. Table 2.3 lists the sources used.

[3] In this last calculation we have taken the ion pump's full speed of 20 l/s. This is justified by the fact that it is connected to the LP end via a DN40 conflat flange, which has an aperture conductance of about 145 l/s.

[4] C. Ryu, personal communication.

Source Material	Quantity (mg)	Alvatec Part Number
^{87}Rb	25	AS-3-Rb87(98%)-25-F
^{87}Rb	25	AS-3-Rb87(98%)-25-F
K	25	AS-3-K-25-F
^{40}K	25	AS-3-K40(5.5%)-25-F
Cs	25	AS-3-Cs-25-F
Li	25	AS-3-Li-25-F

Table 2.3: List of alkali metal sources available for use. The ^{87}Rb sources are enriched to 98% ^{87}Rb, and the ^{40}K source has been enriched to 5.5%, up from a natural abundance of 0.012%. Currently only one source (^{87}Rb) has been activated.

When the experiment is in operation, the source requires between 3.3 to 3.5 A of current for ohmic heating.

2.4 Summary

The upgraded quartz cell and vacuum system design have proved their worth during the operation of the new LANL BEC system. Optical distortions introduced by the previous quartz cell are no longer an issue, and a higher pressure ratio has contributed to halving of the experimental cycle time. Timely identification of the slight rotation of the quartz cell allowed the vacuum system to be shimmed before the complex set of optics and hardware that usually surround the LP quartz cell at close range had been fully installed.

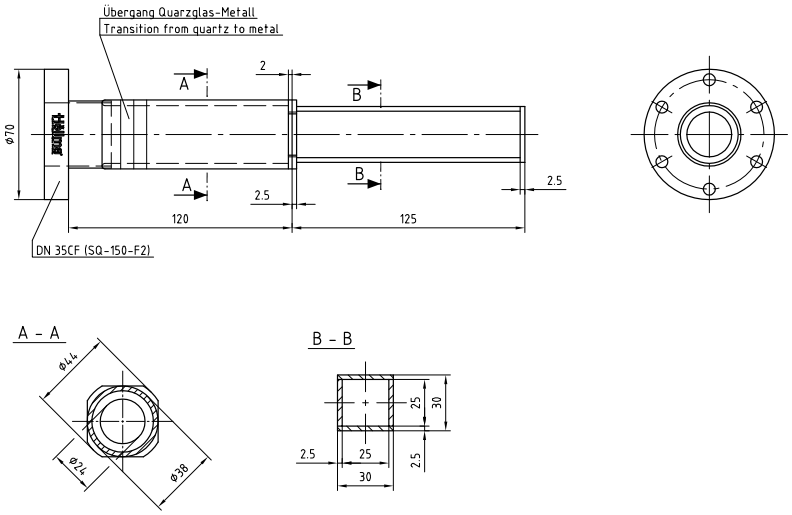

Figure 2.4: Technical drawing of quartz cell provided by Hellma. Used with permission.

Chapter 3

Magnetic subsystem

The LANL BEC machine suffered an insulation failure on the LP magnetic coils in October 2010. The opportunity was taken to re-design the magnetic coil system from scratch, to take advantage of the new, more compact LP quartz cell geometry and use compact anti-Helmholtz coils instead of the bulkier Ioffe-Pritchard set of coils. The new HP vacuum chamber would require a much larger set of coils than those that had been used previously. This chapter covers the basics of quadrupole field generation (Section 3.1) and the design of the LP (Section 3.2) and HP (Section 3.3) magnetic coils.

3.1 Generalities

In order to apply the various cooling methods that will lead the ^{87}Rb atoms to BEC, they must be localized in space. To do this, they must be under the influence of a potential that traps them. This is achieved in the LANL BEC experiment via a quadrupole magnetic field. This type of field can be realized with several different types of magnetic coil. The most straightforward is a pair of coils of parallel and colinear axes and separated by a certain distance, with current flowing in opposite directions, such that the magnetic fields at their center are opposed. This configuration is called an anti-Helmholtz coil pair.

The field produced by this loop pair is determined by integrating the Biot-Savart expression for a segment of wire $d\mathbf{l}$ located at $\mathbf{r}$ carrying a current I. At $\mathbf{r}'$ the contribution of the segment to the total field is

$$d\mathbf{B} = \frac{\mu_0 I}{4\pi} \frac{d\mathbf{l} \times (\mathbf{r} - \mathbf{r}')}{|\mathbf{r} - \mathbf{r}'|^3}. \tag{3.1}$$

The result of integrating this expression for a pair of current loops of current I, separation d and radius R involves elliptical integrals, and so a series expansion about the origin, halfway between the loops, is far more useful. To lowest order, the magnetic field near the center of the trap can be approximated by [56]

$$\mathbf{B} = 48\mu_0 I \frac{dR^2}{(d^2+4R^2)^{5/2}} \begin{bmatrix} -x/2 \\ -y/2 \\ z \end{bmatrix}. \tag{3.2}$$

Taking only the lowest-order term in the expansion is justified since we are interested in the field in the vicinity of the atom cloud, which is at least an order of magnitude smaller in extent than either R or d. The approximate three-dimensional potential the atoms see is then

$$U_B(x,y,z) = \mu_B g_F m_F B'_z \sqrt{\frac{x^2}{4} + \frac{y^2}{4} + z^2} \tag{3.3}$$

with $B'_z = \mu_0 48 I d R^2/(d^2+4R^2)^{5/2}$, the z axis gradient of the magnetic field at the origin. For the ^{87}Rb $|F=1, m_F=-1\rangle$ state, $g_F = -1/2$. It is useful to consider that the minimum z axis gradient required to hold the atoms against gravity is $B_z = 2mg/\mu_B = 0.305$ T/m. [50]

We seek to create the steepest possible trapping potential we can because, generally speaking, the tighter we can compress the atom cloud during the forced RF evaporation process, the faster atoms will be able to rethermalize through elastic collisions, and the quicker the process can be completed. A fast RF evaporation stage (which is the slowest stage in the BEC creation process) means that less time is wasted holding the atoms in the presence of background gas, since these loss processes are constant and act the entire time the atoms are held in the trap.

In seeking to create the steepest possible trapping potential, it is clear from Equation 3.3 that the *gradient* of the magnetic field must be maximized. There are two paths to achieve this. The first is to increase the current in the loops as much as is feasible given the amount of heat that can be practically removed from the coils. The second is to address the shape of the coils themselves. From Equation 3.2, the magnitude of the magnetic field gradient along the z axis of the center of the trap is proportional to a purely geometrical factor

$$\alpha_{\text{geom}} \equiv \frac{dR^2}{\left(d^2+4R^2\right)^{5/2}}. \tag{3.4}$$

Though much analysis can be put into the maximization of this geometrical factor by examining its dependence on d and R, ultimately geometrical design constraints limit the range of values we can choose. At the end of the day the coils are simply designed to be as close to the vacuum chamber (HP MOT) or quartz cell (LP MOT) as is physically feasible, thus fixing d and R for the innermost loops of wire or tube in the coils.

3.2 Low pressure system

The magnetic coils designed and constructed for the LP system were made from 1/8 in hollow copper tube, commonly used in air conditioning and refrigeration systems. This allowed an internal flow of water to dissipate the heat generated by the electrical current flowing through them. To counteract the natural springiness of coiled copper tube, they were constructed layer by layer and held in place with commercial epoxy glue. Figure 3.1 is a picture taken during this process. The copper tube was insulated with a single layer of clear, flexible, PVDF heat shrink tubing, which was expected to prove more robust than the standard, black heat shrink that was used on the previous magnetic coils and which failed after about 15 years of operation.

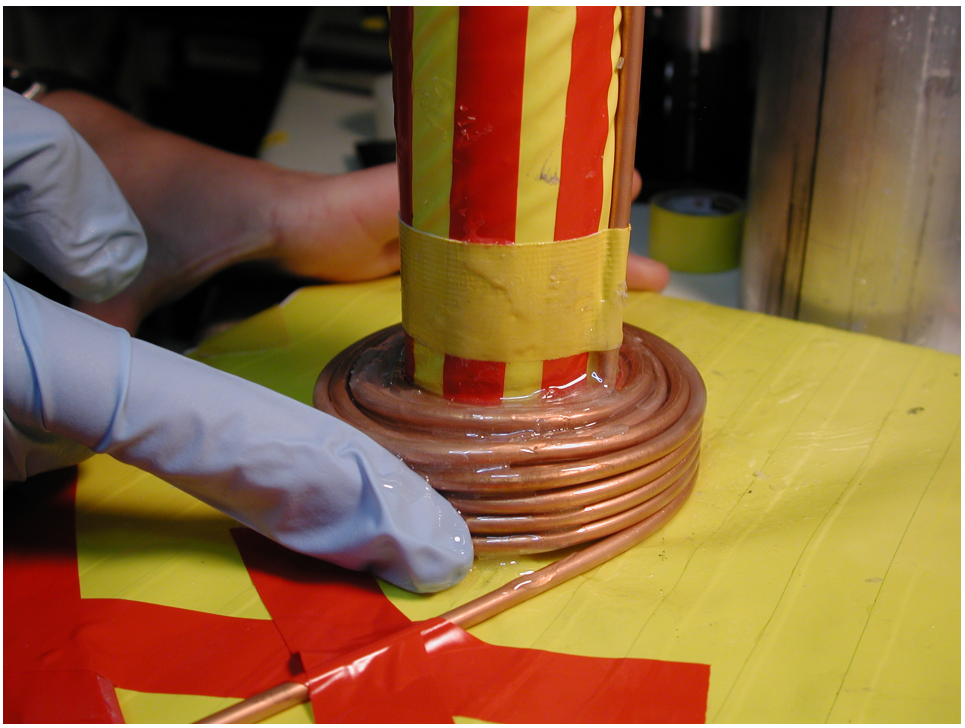

Figure 3.1: Production of an LP magnetic coil. The support and former piece were covered in vinyl electrical tape, since it was found that this was one of the few items available in the lab that the epoxy glue would not adhere to. The adhesive on the back of the tape was scraped off with the help of commercial water-displacing lubricant spray, which was good at un-bonding it from the vinyl. These protective, non-adhesive sheets of vinyl could then be peeled off the formed coil after the expoxy had hardened.

The two unavoidable physical constraints the system's design is subjected to are the size of the quartz cell, which is 30 mm across, and the outer diameter of the Mitutoyo tweezer beam objective (labeled

(h) in Figure 3.2), which is approximately 33 mm, and approaches the cell vertically from above. This determines the absolute minimum coil separation d and inner radius R_i that can be used. Additionally, an air gap must be left between the coils and the cell. This air gap must accommodate the two-loop coil of wire used as the RF antenna for the RF evaporation stage of BEC creation[1]. On the other hand, the number of layers that the coils can extend along their axis and radially outwards is decided by the interplay between electrical and thermal characteristics of the possible alternatives.

Concerning the actual placement of the coils, though there are several configurations that allow good optical access to the BEC by all six MOT beams, the tweezer beam, and the imaging system, one particular configuration was chosen as it would allow a magnetic coil inner diameter limited only by the diameter of a MOT beam, and a coil separation limited only by the OD of the Mitutoyo tweezer beam objective. The latter is about 10 mm larger than the former, so using the coils' central hole for a MOT beam and not the objective results in an improved magnetic gradient at the center of the trap, via α_{geom}'s dependence on R. As an example, for a coil-to-coil separation of $d = 34$ mm, having a MOT beam-sized inner diameter of 24 mm results in a geometrical factor 1.9 times as large as having chosen an inner diameter that would fit the tweezer beam objective (35 mm). Since the magnetic field gradient produced by the coil pair is proportional to the current, this design requires about half the current for the same magnetic field gradient. This is a very strong motivation to pursue this design.

The implementation of this layout is depicted in Figure 3.2. Custom pieces were designed and manufactured to allow stable, adjustable positioning of the coils. Each coil is held by epoxy adhesive in an annular holder that has been slotted to avoid the formation of eddy currents **(g)**. This is mounted to a vertical support block **(d)** via bolts that are free to slide a few cm above and below the center height of the quartz cell. This ability was put to use in the final configuration of the apparatus to allow the center of the LP MOT and magnetic trapping potential to be formed a few mm higher than the quartz cell's centerline. This raised BEC location was chosen to allow a greater distance between the Mitutoyo tweezer beam objective **(h)** and the quartz cell **(b)**. The tweezer beam objective is quite wide compared to its optical working distance (depicted as a red dashed line near the centerline of the cell), to the extent that the MOT beams incident in the vertical plane, shown as crossed dashed lines in the side view of Figure 3.2, must be angled at about 61° from vertical, instead of the more usual 45°. Despite the wider crossing angle, operation of the LP MOT is not functionally compromised.

[1]This antenna was also manufactured by the author. The diameter was taken as just larger than the width of the quartz cell. In that way, the two bulky points of the overlapped, two-loop antenna (where the two loops of common magnet wire cross over each other) could be placed outside the narrow cell/magnetic coil space, allowing a smaller cell/magnetic coil separation. The loops were held in place with thin Kapton tape.

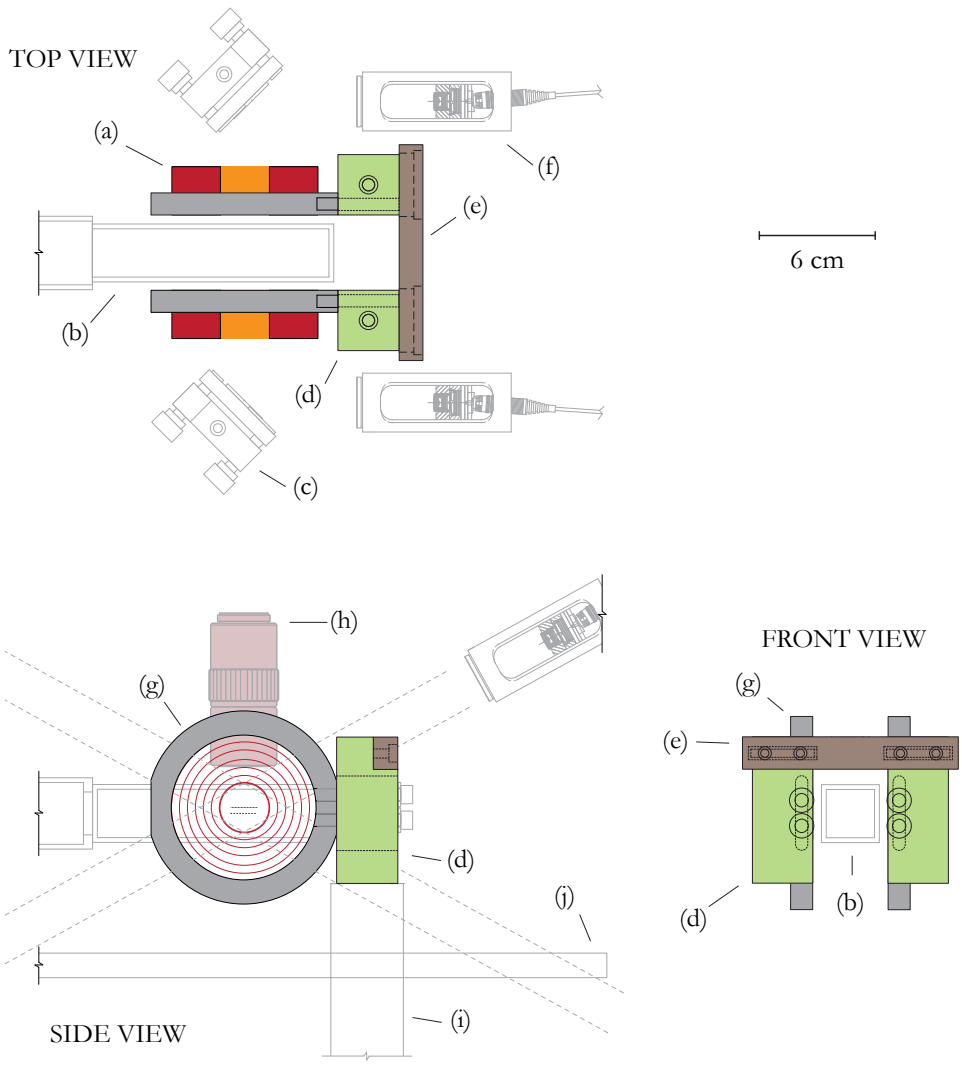

Figure 3.2: LP magnetic coils and support system. See main text for full description. **(a)** Copper coil. **(b)** Quartz cell. **(c)** Folding mirror for MOT beam. **(d)** Vertical support pieces for LP coil (green). **(e)** Cross link to ensure stable LP coil separation (brown). **(f)** LP MOT beam expander. **(g)** Annular support for LP coils (solid grey; anti-eddy current slot not shown). **(h)** Mitutoyo tweezer beam objective and location of focal plane (red, dashed) as compared to quartz cell center (black, dashed). **(i)** Thorlabs DP14 damped 14 inch post. **(j)** Height of raised breadboard pair that hold lateral LP MOT expanders and other optics. MOT beams in the vertical plane are depicted as dashed lines crossing in an obtuse "X".

The vertical support blocks **(d)** are mounted on Thorlabs DP14 damped 14 inch posts and are connected to each other via a cross piece **(e)**. The cross piece ensures a precisely determined coil separation distance, as well as ensuring that the coils are precisely parallel. The cross piece was machined in such a way that it would not interfere with the MOT beam nearest to it. The damped posts ensure

that the vibration present in the LP coils (transmitted from the water chiller and booster pump via the circulating water) is conducted to the optics table, and not the raised platforms that support the tweezer beam system, cameras and two of the MOT beams. These raised platforms **(j)** are also decoupled from the vacuum system and cell.

3.2.1 Thermodynamic and electrical design considerations

Once the geometrical constraints were identified, the next major design consideration was the power dissipation capacity of the system. Given the geometrical constraints, generating the required magnetic field gradients, as we shall see shortly, requires an amount of power that simply cannot be dissipated via radiation and convection. It was necessary to set up straightforward calculations that would examine the feasibility of achieving a given magnetic field gradient when constrained by electrical, hydraulic and thermodynamic considerations. A good design would hopefully be able to function with the existing water circuit chiller, booster pump and high current source.

The starting point for these calculations is the maximum z-axis magnetic field gradient that the LP coils could be expected to generate. Though in the very early design process gradients of 5 to 10 T/m were considered in order to accommodate unknown future requirements, a more modest maximum target of 4 T/m was set. This a few T/m larger than the gradients used in [50], who also use an optical dipole trap as the final stage of BEC creation. The expected day-to-day maximum working gradient was taken to be 2.4 T/m. This value was taken from the previous (Sussex) experimental setup as operated at LANL, where the z axis gradient that was commonly used was reported to be 8 times that required to hold the atoms against gravity.[2]

Presently (Spring 2012) experimental requirements do not have an exceedingly large BEC as a priority, and therefore the experiment is simply run with parameters that have been optimized for the current operation, and not necessarily with the highest magnetic field gradients that could be used. The compressed magnetic trap is currently ramped up to a maximum current of 122 A during the adiabatic magnetic compression stage, which is calculated to generate about 3.6 T/m, or 11.9 times the gradient required to hold atoms against gravity. Another reason for not operating with the highest magnetic field gradient is that whereas doing so might cut the experimental cycle time by a few seconds, the undesirable local heating around the LP coil cell outweighs the possible time gains, especially if the experimental cycle is much longer, on the order of half a minute or so.

A *Mathematica* notebook was set up to provide a dynamically-updated table listing the predicted

[2] C. Ryu, personal communication.

electrical, thermal and hydraulic properties of the coil pair given the required z axis gradient B'_z, the number of loops per coil along the axial direction and the number of layers of loops in the radial direction, as well as other relevant physical parameters. This provided great freedom to quickly consider many "what if" cases.

The starting point of these calculations was the evaluation of an expression that calculates B'_z as a sum of contributions for every loop pair in the coils. The real-world loop-to-loop separation of previous insulated and epoxied coils was measured and used to accurately predict the radius and separation of each loop pair, where the effective conductor radius R_j and z axis separation d_j are taken as

$$\begin{aligned} R_i &= R_{\text{clear}} + \frac{\Delta_R}{2} + i\Delta_R \\ d_j &= d_{\text{clear}} + \Delta_d + j2\Delta_d. \end{aligned} \tag{3.5}$$

R_{clear} and d_{clear} are the minimum assured clear apertures through the center hole and between the coil pair, respectively. This is illustrated in Figure 3.3. The expression for the total magnetic field gradient along the z axis is then

$$B'_z = \mu_0 48 I \sum_{i=0}^{N_R-1} \sum_{j=0}^{N_z-1} \frac{d_j R_i^2}{(d_j^2 + 4R_i^2)^{5/2}}. \tag{3.6}$$

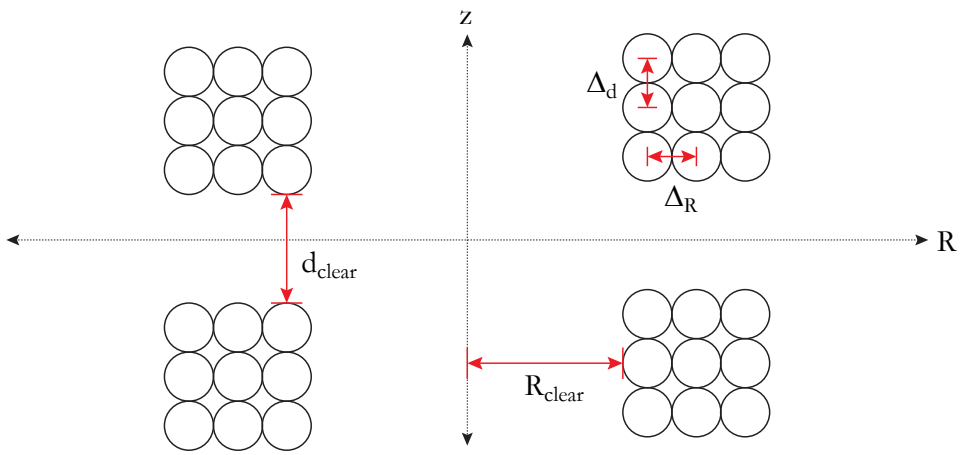

Figure 3.3: Layer-by-layer conductor position for gradient calculation. In this cross-section view the radial and axial position of each loop of insulated and epoxied copper tube is considered during the calculation of the magnetic field gradient at the origin. A schematic coil pair (top and bottom) is illustrated by coils that have 3 radial and 3 axial layers.

Equation 3.6 is solved for I to express the current that is required to achieve a required B'_z when the number of radial N_R and axial N_z loops, per-loop average separation and minimum clear separations R_{clear} and d_{clear} are given.

The total resistance of the coils is calculated from the total length of both coils (itself determined by adding up all the perimeters according to Equation 3.5), the conductor cross-section and the temperature-dependent resistivity of copper ρ_T, [57]

$$\rho_T = \rho_{20}[1 + \alpha_{20}(T_c - 20^\circ)] \tag{3.7}$$

where $\rho_{20} = 1.72 \times 10^{-6}$ ohm-cm and $\alpha_{20} = 0.0041K^{-1}$. With the total resistance and the required current, we are able calculate total power dissipation $P = I^2R$, and total voltage drop $V = IR$.

The expected water flow depends on the tube's inner diameter, roughness, temperature and length. An excellent approximation, however, is [57]

$$Q_{\text{capacity}} \approx 3.84 \times 10^5 \sqrt{\frac{\Delta P}{L_{\text{single}}}} w_{\text{ID}}^{5/2}. \tag{3.8}$$

In the above expression, the flow Q_{capacity} in liters per minute is determined by the total pressure drop ΔP in atmospheres, the length of one coil L_{single} in meters and the internal diameter of the tube w_{ID} in meters. It should be remembered that this is the per-coil flow capacity, and since both coils are hydraulically connected in parallel, the total system flow will be double this amount.

If each coil is expected to dissipate a power P_{single}, then one can perform a very rough calculation to determine the flow rate required to remove this amount of energy per second. Indeed, if it takes E joules to raise the temperature of a mass m of water by ΔT degrees, with $E = c_p m \Delta T$ and $c_p = 4.186$ $J/(g \cdot K)$ the specific heat of water, then the water flow required to carry away this amount of heat per second is

$$Q_{\text{required}} = \frac{P_{\text{single}}}{c_p \Delta T}. \tag{3.9}$$

The above expression assumes perfect heat transfer between the copper and the cooling water, and completely neglects the expected temperature rise that the water will experience as it travels through the coils. Nevertheless, as a ballpark figure, this calculation proves useful.

A coil configuration with 6 radial layers and 5 axial layers was selected based on the expected water flow requirements and coil capacity, as well as the characteristics of the available power source (maximum power, voltage and current). Tables 3.1 and 3.2 provide a summary of various coil alternatives and their predicted properties at B'_z of 2.4 T/m and 4 T/m.

After construction, the coils were checked against the predictions described above. The measured and predicted values are compared in Table 3.3. The water flow capacity of each coil was measured at

R Layers	Z Layers	Voltage (V)	Resistance (mOhm)	Current (A)	Power (W)	Flow Required (LPM)	Flow Capacity (LPM)
2	5	1.6	10	164	269	0.38	2.03
3	5	1.8	15	122	224	0.32	1.66
4	5	2.1	21	102	216	0.31	1.41
5	5	2.4	28	90	223	0.32	1.23
6	**5**	**2.9**	**35**	**82**	**238**	**0.34**	**1.09**
7	5	3.3	43	77	258	0.37	0.98
8	5	3.8	52	74	283	0.40	0.89

Table 3.1: Predicted electrical and hydraulic characteristics of various designs of LP coils for $B'_z = 2.44$ T/m, a water-conductor ΔT of 10°, operating pressure of 110 PSI, clear aperture diameter of 25.4 cm and a coil separation of 35 mm. The row that corresponds to the coils that were constructed is hilighted in bold. LPM stands for litres per minute.

R Layers	Z Layers	Voltage (V)	Resistance (mOhm)	Current (A)	Power (W)	Flow Required (LPM)	Flow Capacity (LPM)
2	5	2.7	10	268	722	1.0	2.03
3	5	3.0	15	200	601	0.86	1.66
4	5	3.5	21	167	580	0.83	1.41
5	5	4.0	28	147	598	0.85	1.23
6	**5**	**4.7**	**35**	**135**	**638**	**0.91**	**1.09**
7	5	5.5	43	126	693	0.99	0.98
8	5	6.3	52	120	761	1.10	0.89

Table 3.2: Predicted electrical and hydraulic characteristics of various designs of LP coils for $B'_z = 4$ T/m, a water-conductor ΔT of 10°, operating pressure of 110 PSI, clear aperture diameter of 25.4 cm and a coil separation of 35 mm. The row that corresponds to the coils that were constructed is highlighted in bold. LPM stands for liters per minute.

60 PSI using the facility water line and compared to the flow predicted. The degree to which Equation 3.8 and what was measured agreed was a welcome surprise, and this lends credibility to the extrapolated flow calculation at 110 PSI, which is the LP cooling circuit's operating pressure. It should be noted that despite the fact that a precisely-positioned magnetometer was used to measure B'_z at a current of 5 A, thus providing a value for how many T/m are produced per amp, in practice this value is measured via the minimum coil current required to hold the atoms against gravity, once everything has been assembled and is in its final operational position.

It remained only to check whether or not the existing pump system would be able to drive the expected flow rates and attain the pressures required for LP coil operation. First, water pressure at

Parameters	Measured	Calculated
Outer diameter (mm)	74	68
Resistance, total (mOhm)	38	35
Water flow at 60 PSI, single coil (LPM)	0.41	0.40
Water flow at 110 PSI, single coil (LPM)	-	0.55
Current required to reach 0.093 T/m (A)	5	4.99

Table 3.3: Comparison between predicted and measured properties of LP coils.

the chiller's pump[3] is raised to about 65 PSI (measured) and sent through 3/4 in plastic tubing to a Tuthill booster pump. This gear pump[4] raises the water pressure to about 105 PSI, and it is then sent to the LP coils. Figure 3.4 summarizes the pump and system characteristic curves for our setup. It indicates that the maximum flow this system could drive through the coils is about 1.35 LPM at 170 PSI, but the actual operating point is just over 1 LPM at 105 PSI since the booster pump is not driven at maximum speed.[5] It is found that this operating point keeps the coils cool at the currents used in day-to-day operation, and the added pump capacity will allow higher magnetic field gradients to be reached in future, should the need arise, up to around 4.9 T/m (though since the LP coils are not used throughout the entire experimental cycle, higher gradients may be achievable).

Finally, the inductance of each coil was measured using an oscilloscope and a square wave generator. The voltage drop across three resistances of measured value placed in series with the coil was measured at four points along its RL curve.[6] Coil 1 was found to have an average inductance of 25.4 ($\sigma = 1.1$) μH and Coil 2 of 20.9 ($\sigma = 2.2$) μH. With these inductances, an unassisted shutoff of the coils can be performed in a calculated time of 1.4 and 1.2 ms, respectively, which is adequate for current experimental requirements. As a point of reference, the previous system's LP coils' inductance was 360 μH each.

[3]Thermo Neslab Merlin M75 chiller using a PD1 rotary vane pump with an essentially flat characteristic curve of 5.7 LPM from 0 to 60 PSI, at least according to the manufacturer's literature.

[4]Model number DGS.57PPPV2NN0V000, 0.57 ml per revolution displacement.

[5]Measuring the actual rotational speed of the gear pump would not be straightforward, since the pump is controlled by a controller (Dart Controls Inc., model 15DVE) that regulates pump drive velocity via an unmarked potentiometer.

[6]The internal resistance of the function generator was measured and taken into account.

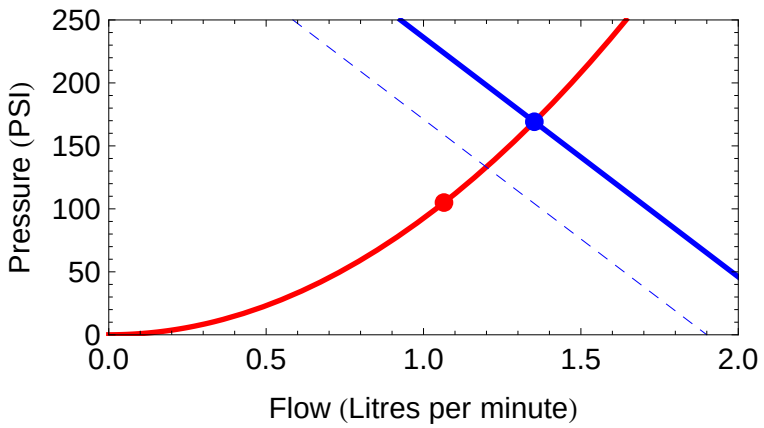

Figure 3.4: Pump and system characteristic curves. Shown is the theoretical system curve of the LP coils (red), plotted along with the pump characteristic curve of the Tuthill booster pump acting alone (dashed, blue) and acting in series with the 65 PSI head provided by the chiller's PD1 pump. The booster pump's curves are graphed for 3500 RPM operation, as per literature provided by the manufacturer [58], but it is very likely that the booster pump is operated at a lower RPM, given that the measured LP coil pressure drop is 105 PSI and just over 1 LPM, as represented by the red dot on the system curve. The theoretical system-pump operating point at 3500 RPM is 1.35 LPM at 170 PSI (blue dot).

3.3 High pressure system

Unlike the LP coils, the coils designed for the HP system do not have to attain the very high magnetic field gradients required for purely magnetic trapping, since they are only required for MOT creation. The coils from the earlier incarnation of the system could not be recycled, owing to the completely different shape and size of the HP vacuum system end. Figure 3.5 shows the main tool used in the design of the HP coils. Despite the fact that the magnetic field gradient requirements were modest (the Sussex BEC HP MOT required around $B'_z = 0.1 \sim 0.14$ T/m [33]), it was immediately apparent that care would have to be taken with respect to the placement of the coils. Location **(g)** of Figure 3.5 was naturally considered, but the window on the top of the HP vacuum system is further from the center of the trap than **(g)**, forcing the coil placement much further down, in the region of $\alpha_{\text{geom}} \sim 1.0$.[7] Wrapping unbound loops of wire in the corner near **(c)** was also considered, but this idea was discarded because it did not provide enough conductive cross section to keep the power requirement down to a reasonable value. Ultimately the location **(d)** was chosen, and once R_{clear} and d_{clear} were determined for the coils, all that remained was to pick a given number of radial and axial layers of wire, as well as the cross section of the wire used. A dynamic spreadsheet was constructed, as was done for the LP

[7] Coils with asymmetrical radius and z axis position were briefly considered and analyzed, but it was found that the structure of the magnetic field gradient around the trap center was compromised by using this setup.

magnetic coils, as is shown in Table 3.4.

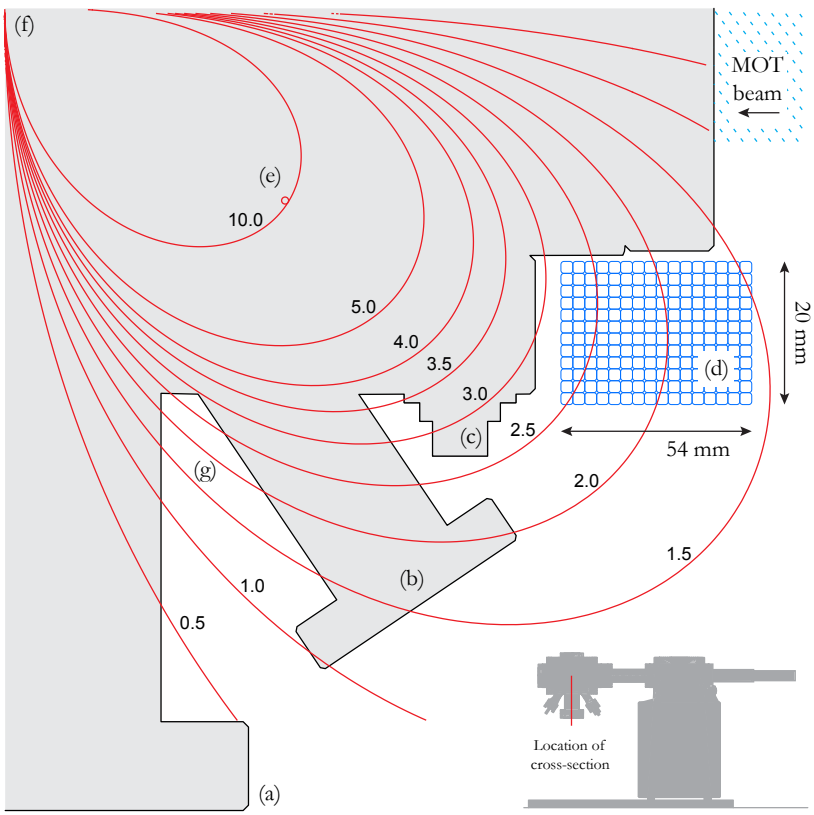

Figure 3.5: Placement of HP magnetic coils. The HP end of the vacuum system is shown in cross section and silhouette. Only the lower-right quadrant is depicted. **(f)** marks the geometrical center of the MOT trap. The long axis of the entire vacuum system (or similarly, the push beam axis) is into the paper. The illustration terminates on the left hand side at the vertical axis of the magnetic trap, and at the top it terminates at the center of a MOT beam. The bottom MOT window is at **(a)** (vertical MOT beam not shown) and **(b)** is one of the six arms housing the various alkali metal vapor sources. Shown also is the head of a standard hexagonal 1/4-20 bolt **(c)**. Superimposed are contour lines for the geometrical factor $\alpha_{\text{geom}} = dR^2/(d^2 + 4R^2)^{5/2}$. These are contours of the value α_{geom} would assume for a single anti-Helmholtz loop pair placed at a given location. The HP magnetic coils that were constructed were placed at **(d)**. For reference, the previous system's HP coils were located at **(e)**. Note the difference in α_{geom} for both coil locations.

The main concern during the design of the HP coils was the ability to dissipate enough heat while maintaining the current required for operation. The previous, Sussex-era HP coils were mounted on aluminum formers and dissipated approximately 10 W during operation. It was expected that a considerably larger surface area would allow the new HP coils to operate at a reasonable temperature. This

R Layers	Z Layers	Length (m)	Voltage (V)	Resistance (Ohm)	Current (A)	Power (W)
14	12	5.4	5.4	1.3	4.0	21.6
15	12	5.4	5.4	1.4	3.8	20.5
16	**12**	**225**	**5.5**	**1.5**	**3.6**	**19.6**
17	12	241	5.6	1.7	3.4	18.8
18	12	257	5.7	1.8	3.2	18.2

Table 3.4: Predicted electrical characteristics of various designs of HP coils for $B'_z = 0.09$ T/m, conductor temperature of 30°, 7.2 cm separation and 15.9 cm inner diameter. The conductor-to-conductor spacing was taken as 1.7 mm. The row that corresponds to the coils that were constructed is highlighted in bold.

was found to be the case after construction. Based on geometrical considerations, a 16 by 12 winding scheme was chosen. The total length of this design was about 25 m below the total amount of copper wire available.[8]

A wooden former was constructed to aid in the winding of the coils, and this was placed on a workshop lathe to provide a sturdy, rotating axis. Pre-bent plastic zip ties were laid in grooves cut in the former's central barrel (constructed out of fiberglass tubing) and these were used to secure the coils until they were wrapped with thin kapton tape. A foam dummy matching the shape and size of a coil was made to make sure the lower HP coil could be mounted without damaging the delicate electrical contacts of the feed-through connectors on the underside of the HP vacuum system (see Figure 3.10).

The finished coils were measured and found to have an internal diameter of 15.9 cm, an outer diameter of 21.3 cm, and a height of 2 cm. Their total series resistance was measured and found to be 1.65 ohm. The gradient produced by a given current was not measured, but they were found to perform according to requirements once mounted in the experiment.

In addition to the HP magnetic coils, it was found that a small bias coil pair was needed to help line up the HP MOT center with the centerline of the HP/LP vacuum system constriction tube. A simple 250 turn, 26 AWG coil of diameter 11 cm was made and mounted near the outside of the HP vacuum chamber.

[8] 200 m of wire sold by MWS of California. Ordered as 14 gauge, square section, HAPT (poly amide resin insulation), NEMAMW36-C, Class 200C.

3.4 Summary

The new anti-Helmholtz coil pair on the LP end are considerably more compact than the numerous set of coils required for Ioffe-Pritchard field generation, and allow better optical access to the cell. Their relatively precise design allows their placement only a few millimeters from the quartz cell and MOT beams, allowing high field gradients to be generated efficiently. Improved heat shrink insulation and the rigidity offered by their epoxy encasement should ensure that the LP coils will not suffer a short circuit in future. Mechanical anchoring directly to the optics table surface ensures that the vibrations from the water pumps that are transmitted to the rest of the system are minimized. Also, the HP anti-Helmholtz coils were successfully designed and constructed to meet magnetic field gradient and space constraint requirements.

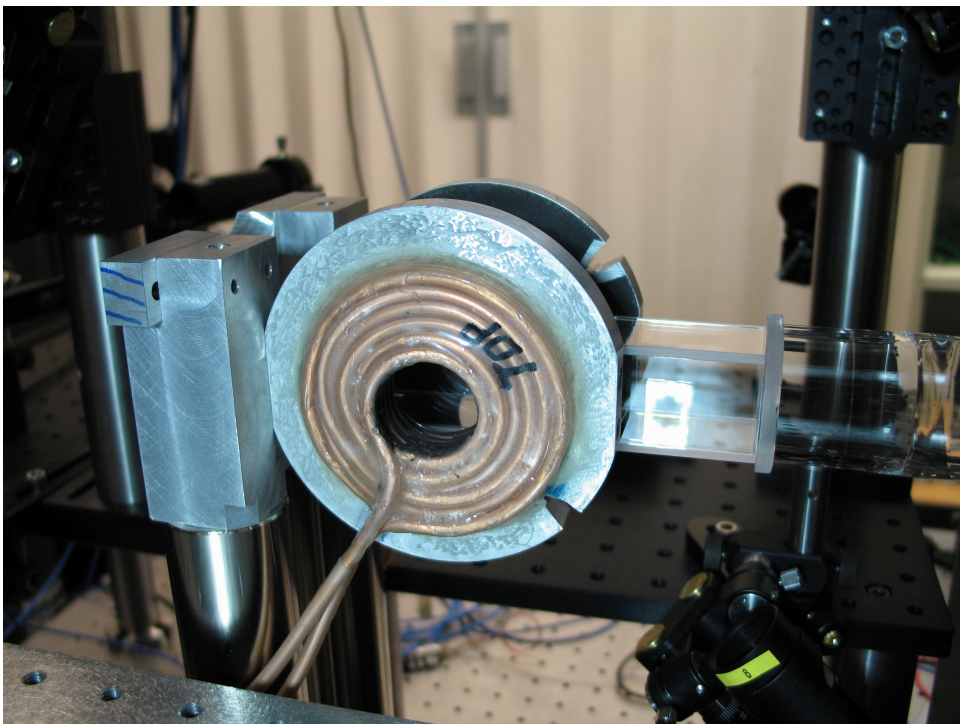

Figure 3.6: LP MOT coil mounting system, side view.

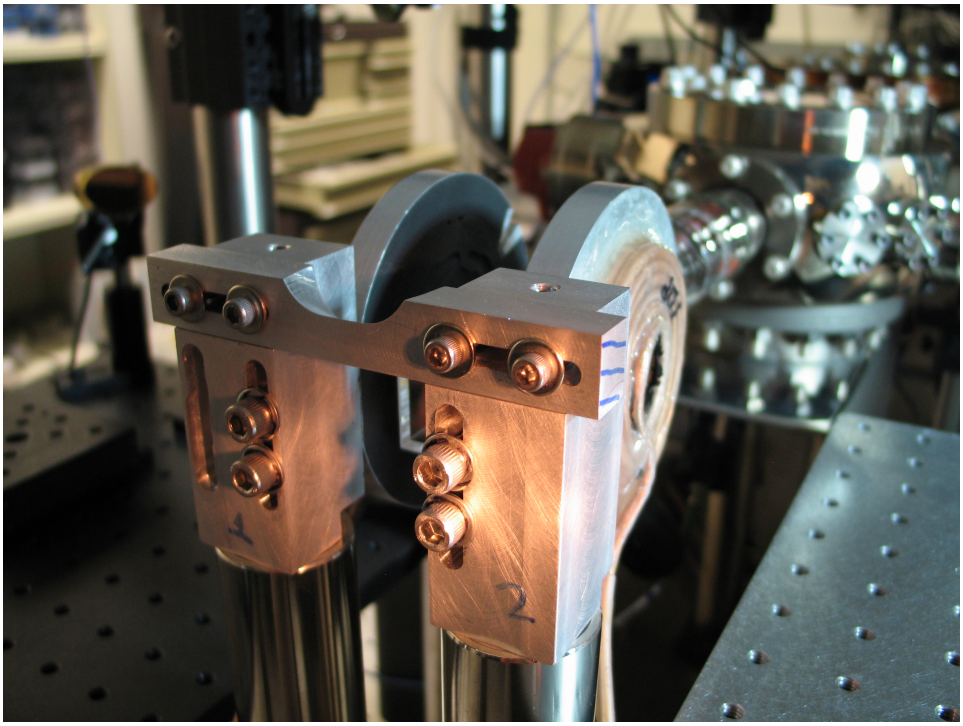

Figure 3.7: LP MOT coil mounting system, front view. Note the machined crossbar, allowing the 61°-from-vertical MOT beam unobstructed view of the cell.

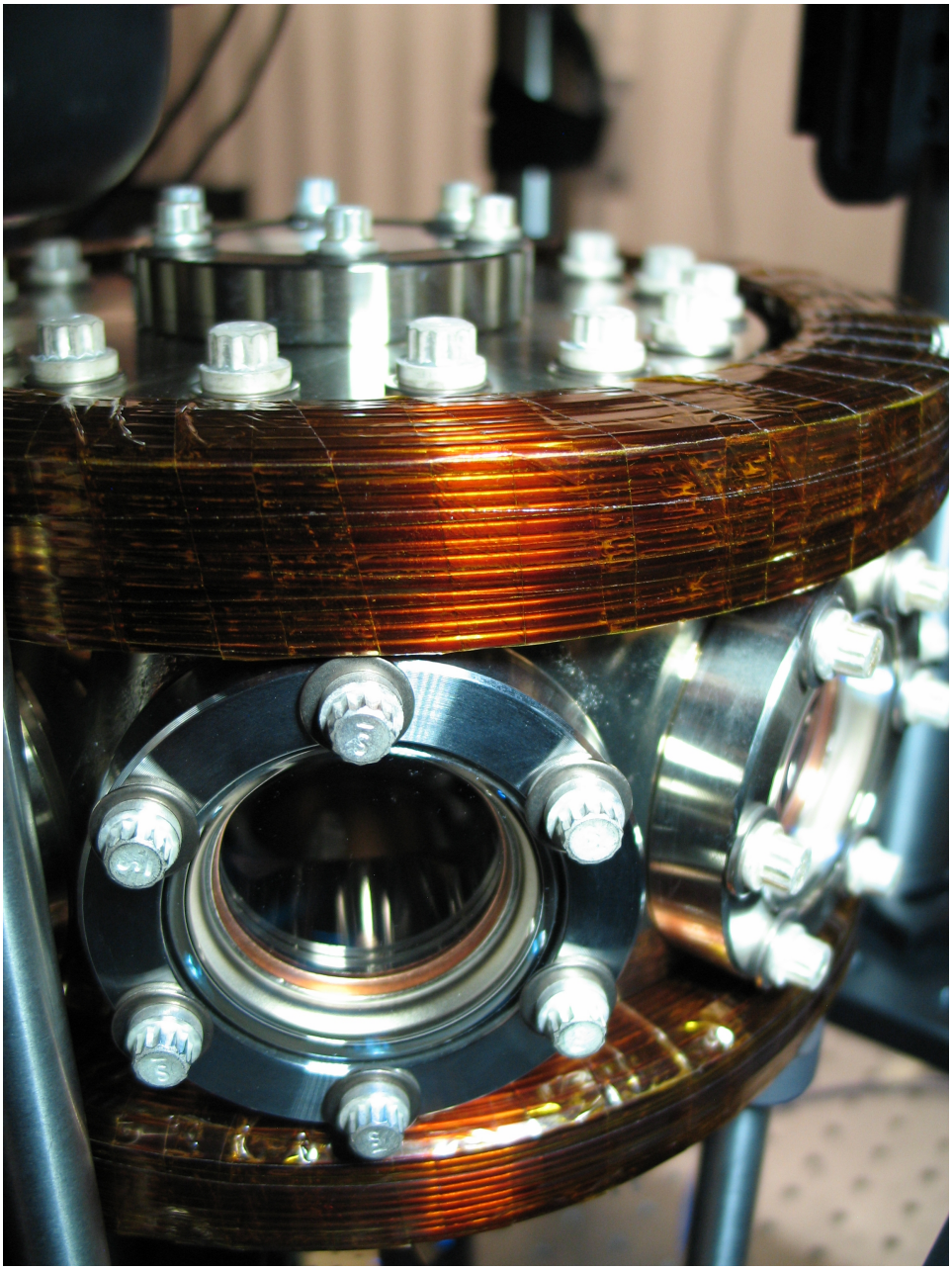

Figure 3.8: HP MOT coils mounted, top coil.

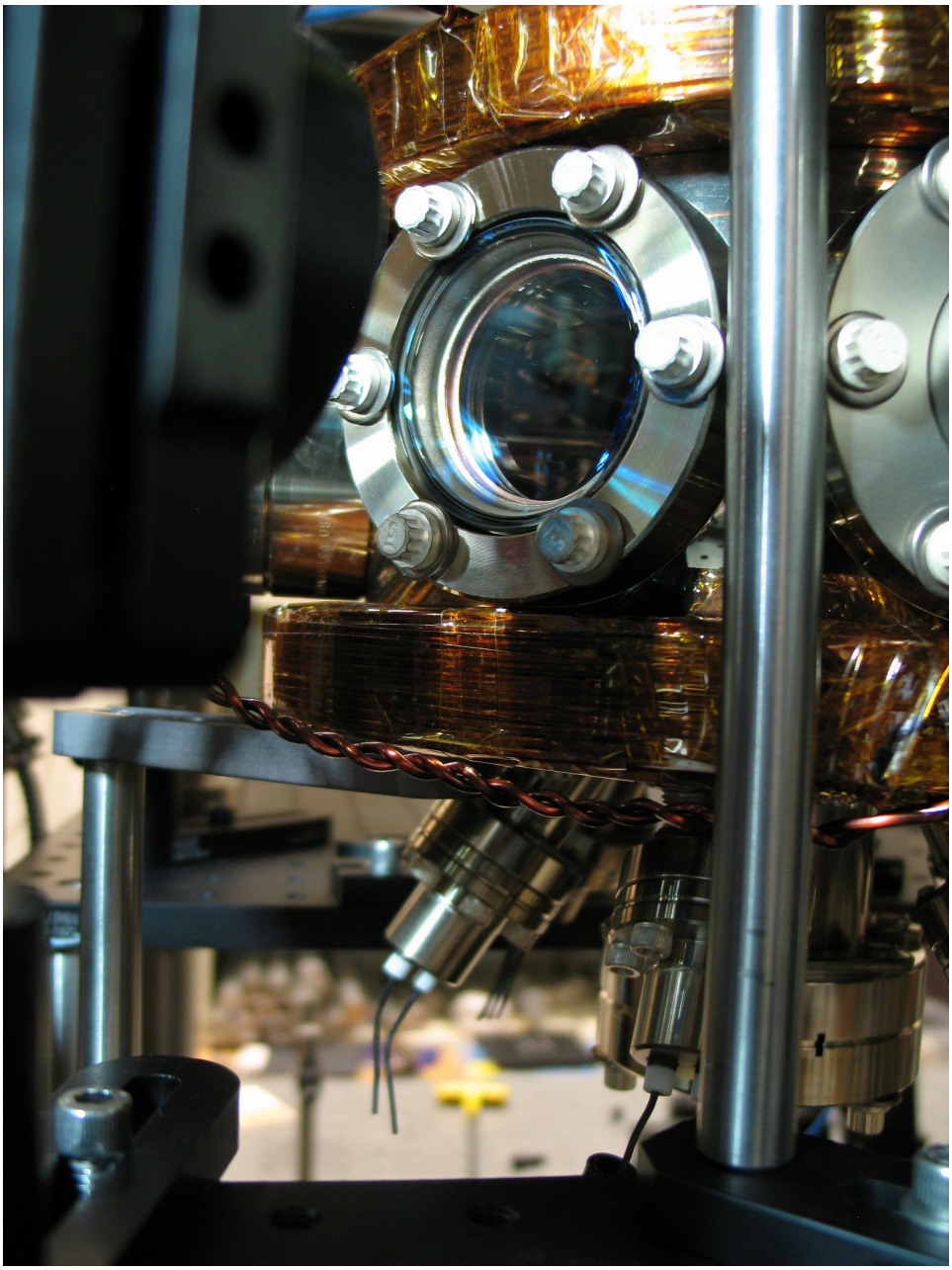

Figure 3.9: HP MOT coils mounted, bottom coil. Note the electrical feed-throughs and their electrical contacts, some of which are brittle, some pliable.

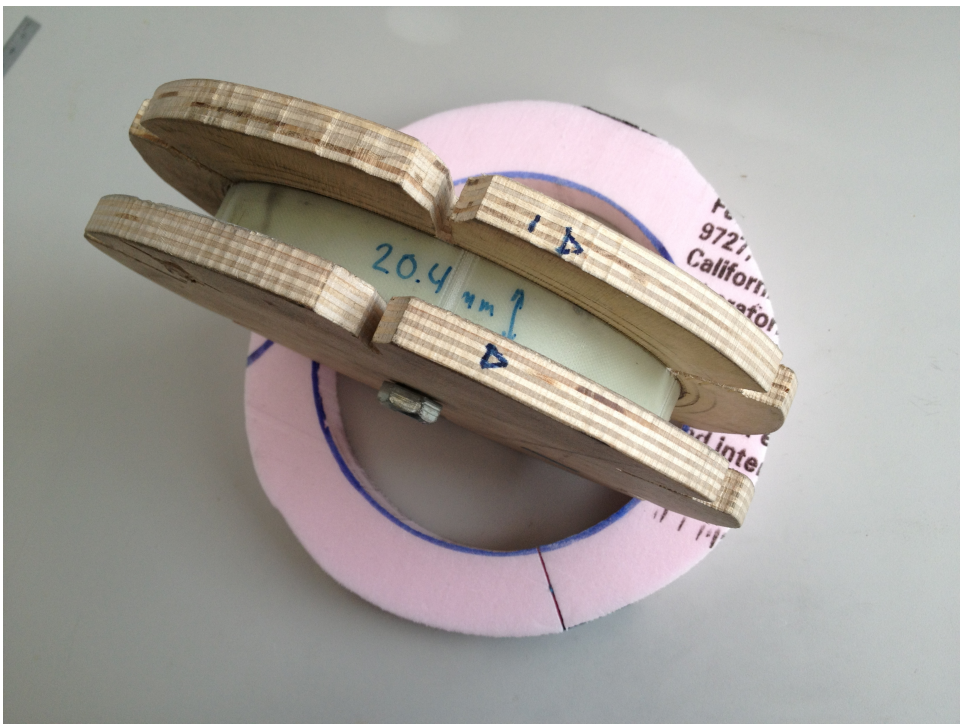

Figure 3.10: Wooden former and dummy for HP coils.

Chapter 4

Laser System

The LANL BEC experiment requires a multitude of frequency-stabilized laser beams of precisely controllable power in order to operate. This Chapter covers the changes and upgrades to the laser system that were carried out between 2009 and 2011.

Following an overview of the laser system (Section 4.1), the diode lasers that provide most of the required laser light are covered, as well as the method used to lock their frequency (Section 4.2). Following that, an analysis of fiber coupling efficiency is detailed (Section 4.4), since this is relevant to the design of the 1-to-3 and 1-to-6 beam dividers and associated optics required for the three HP MOT beams and 6 LP MOT beams (Section 4.5). Finally, a discussion of issues that were encountered with the polarization-maintaining optical fibers used in the experiment is discussed in Section 4.6.

4.1 Overview

The driving requirement behind the construction of this system was to provide frequency-stabilized light that could be mechanically decoupled from its source system and brought to bear on the BEC via optical fiber with more trapping power than that which had previously been available at the MOT traps.

A quick estimate of the amount of power required for the experiment's MOT beams is useful to determine what sort of laser source is required for the experiment. If we take the HP MOT beams as 50 mm diameter and the LP mot beams as 22 mm diameter, then the approximate total beam area is $3 \times (\pi 2.5^2) + 6 \times (\pi 1.1^2) = 82$ cm^2. In order to drive each beam near the saturation intensity of 1.6

mW/cm^2, we require about 130 mW of total laser power, and this is before considering the roughly 80% efficiency of an AOM or the 60-70% efficiency of a fiber coupler. It is clear that a simple diode laser producing on the order of 30 mW is not enough to achieve this objective.

The extra power is provided by a New Focus tapered amplifier, model TA-7613, able to achieve in excess of 1 W output. The seed laser for the amplifier, as well as the laser that provides the repump light, are two New Focus Vortex Series StableWave TLB-7013 tunable diode lasers (external cavity diode laser, Littman-Metcalf design), which were used at about 30 mW output.

At the heart of the laser system are the accousto-optical modulators (AOMs) that shift the frequency of two laser diodes to the correct frequencies needed to manipulate and maintain the BEC. Figure 4.1 outlines the particular shifts used.

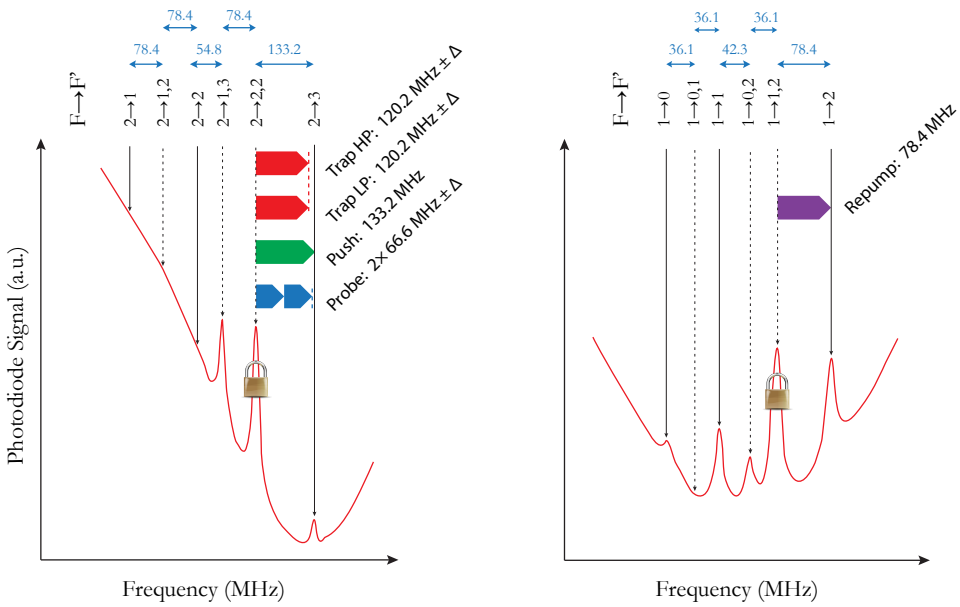

^{87}Rb $F = 2 \rightarrow F' = 1, 2, 3$ ^{87}Rb $F = 1 \rightarrow F' = 0, 1, 2$

Figure 4.1: Frequencies provided by the laser system (not to scale). Overlaid on two ^{87}Rb saturation absorption spectra are elements indicating the features that the lasers called "Zeus" and "Hera" are locked to, marked by a padlock, and the frequency shifts provided by AOMs further down their beams. In red, the trapping light, with a separate AOM for the HP and LP beams, both detuned to the red of the $(F \rightarrow F')$ 2→3 transition. In green, the push beam, on resonance and in blue, a 66.6 MHz AOM through which light is passed twice, for a detunable shift near the resonance. Repump light from Hera is shifted up by 78.4 MHz to the 1→2 transition.

The main elements in the laser system and their logical arrangement are depicted in Figure 4.2.

The two 780 nm diode laser systems, nicknamed "Hera" and "Zeus" for convenience, both locked to crossover features of the ^{87}Rb saturated absorption spectrum, provide the light required for trapping, repumping, pushing and probing the BEC. Both lasers have optional pickoffs via fiber coupling, but these are unused currently.

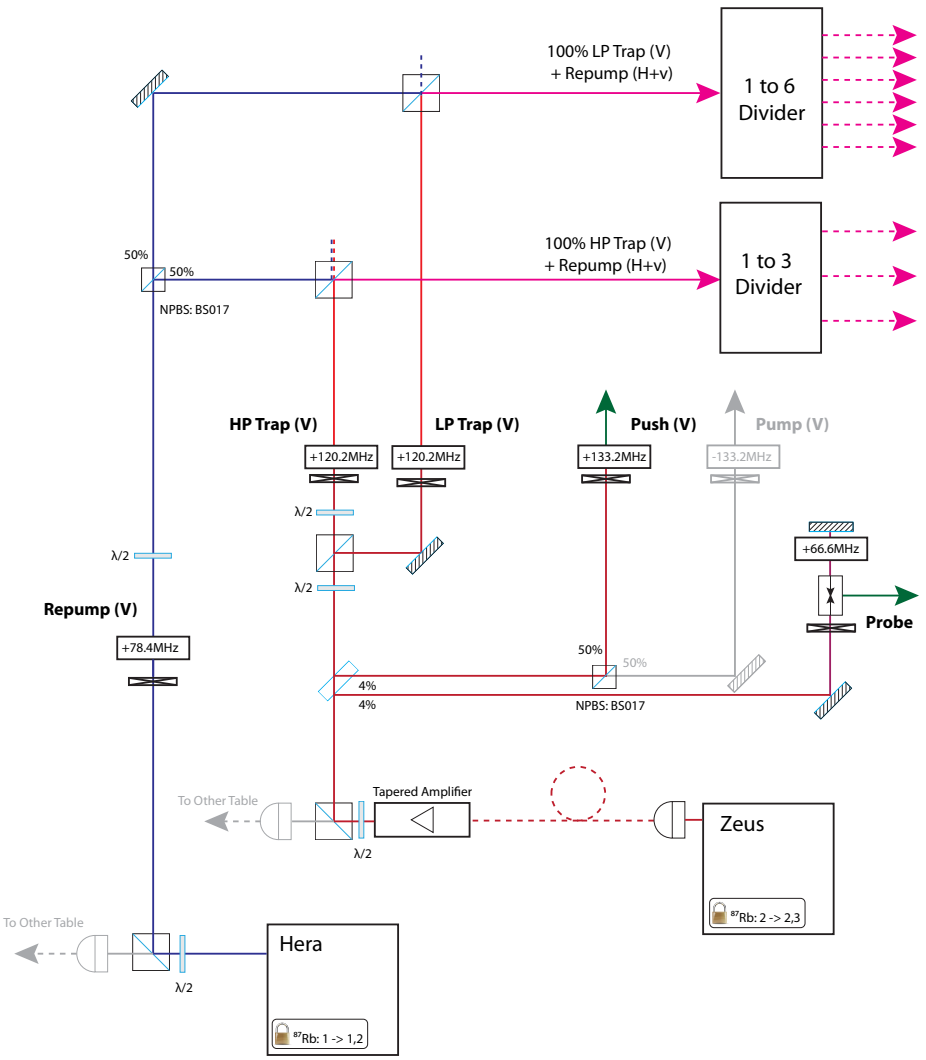

Figure 4.2: Schematic layout of North table laser system. The polarization of the beams sent to the beam dividers is vertical for the trapping light and horizontal for the repump light. See main text for a detailed description.

The laser called Hera produces light that is frequency-shifted via AOM to the frequency required for repumping the BEC atoms. This light is split into two beams via a non-polarizing beamsplitting

cube (PBS) and overlapped with the trapping light that originates from the other diode laser, Zeus. The light from Zeus is amplified via a tapered amplifier (TA) to about 1.1 W. Most of this light is then destined to be overlapped with the repumping light, and both overlapped beams are sent to the 1-to-3 divider (for the HP MOT) and the 1-to-6 divider (for the LP MOT). A half-waveplate control the ratio of this split. A thick glass blank picks off a small amount of light for the push beam and the probe beam. The probe beam is frequency shifted via a cat's eye arrangement (described below) and a double pass through an AOM. Provisions were made for a separate pump beam, but this was not implemented.

Though little power goes into the push and probe beams, it was nonetheless important (at the design stage) to determine if enough light would reach the BEC to maintain saturation of the relevant transition. The first requirement was to determine the diffraction efficiency of the family of AOMs that had been acquired from IntraAction. The 66.6 MHz model was tested and found to have an efficiency of about 75% at maximum RF drive power. The real-world fiber coupling efficiency of the Thorlabs/OFR PAF-X-5-B fiber couplers used throughout the experiment was not seen above 80% in optimal conditions, and can be taken as 50% as a conservative low-end estimate. On the other hand, the relationship between the power in a Gaussian beam and its peak intensity is

$$P_0 = I_{peak}\frac{\pi\omega^2(z)}{2}, \tag{4.1}$$

so if, as a point of reference, a beam with a 5 mm diameter and 4 mW/cm^2 peak intensity (above the 1.6 mW/cm^2 saturation intensity of the relevant ^{87}Rb transitions) will need about 0.4 mW total power. Accounting for a single AOM pass and coupling into fiber, roughly only 2 mW have to be picked off the main beam for the repump and push beams. This power level is two orders of magnitude below what is available from the tapered amplifier, and thus it was determined that the intensity goals could be met for the relevant non-trapping beams.

In the case of the probe beam, it was necessary to use a cat's eye setup to minimize from angular beam deviations as a result of changing the AOM's frequency. This type of setup is used when an AOM's driving frequency is expected to be changed, but the direction of the outgoing beam must not deviate appreciably. Figure 4.3 shows an outline of how this method works. It was found that a 650 μm waist beam undergoes 5 μrad/MHz deviation in a range from 61 to 71 MHz using a 30 cm lens pair and the probe beam's 66.6 MHz AOM. This was considered adequate for the purposes of this experiment.

Figure 4.4 is a scale drawing of how the laser system was physically assembled.

The blocks marked Hera and Zeus represent the slightly raised platform containing the diode laser heads and optical elements necessary for saturated absorption frequency locking. Both beams start

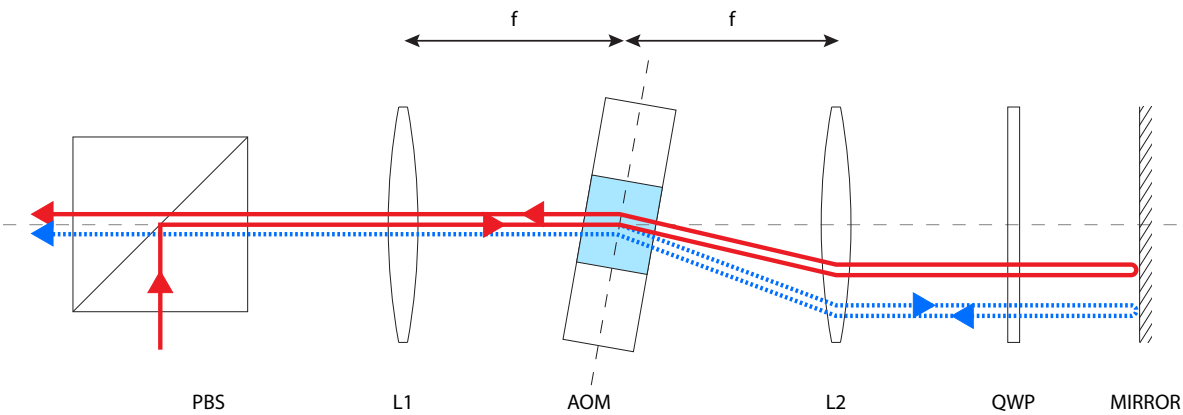

Figure 4.3: How a cat's eye double-pass AOM shift works. The red beam's polarization is perpendicular to the table surface in this top-down view. The AOM is placed at the focus of lens L1, and angled through half the optimal diffraction angle for the frequency of interest. After the half-frequency shift, the beam is re-collimated by L2 to its original diameter, and the quarter wave plate rotates the beam's polarization to horizontal after its second pass. The beam then receives its second frequency at the AOM, and passes through the polarizing beamsplitter cube on to the rest of the system. If the AOM's driving frequency must be changed, the diffraction angle of the beam changes as well. Since the AOM is at the focus of the lens pair, however, the effect this change has on the final angular deflection of the beam is minimized.

with a polarization vector perpendicular to the table surface. At **3**, a half wave plate (HWP) rotates the polarization of Hera's beam, having been previously frequency-shifted to the repump frequency. A non-polarizing beamsplitting cube then splits the repump light into equal beams, irises block unwanted diffraction orders from the frequency-shifting AOM, and both beams are merged with the trapping light at polarizing beamsplitter cubes at **4**.

On the other hand, Zeus' beam is fiber coupled into the TA-7613 tapered amplifier at **1**. The TA's beam is taken to have its waist at **2**. The half wave plate at **5** controls the split between HP and LP laser power. The HWP at **6** rotates the polarization of the beam to vertical again, and they are overlapped with the repump light at **4**, where they are then directed to the HP (**7**) and LP (**8**) beam dividers.

A thick glass blank at **9** splits a few mW of the main beam into the light required for the probe and push beams. The cat's eye setup at **10** ensures that changing the frequency of the probe beam's AOM won't change its direction, as it would be impossible to maintain a useful beam coupling at **11** if this were not the case (see Figure 4.3).

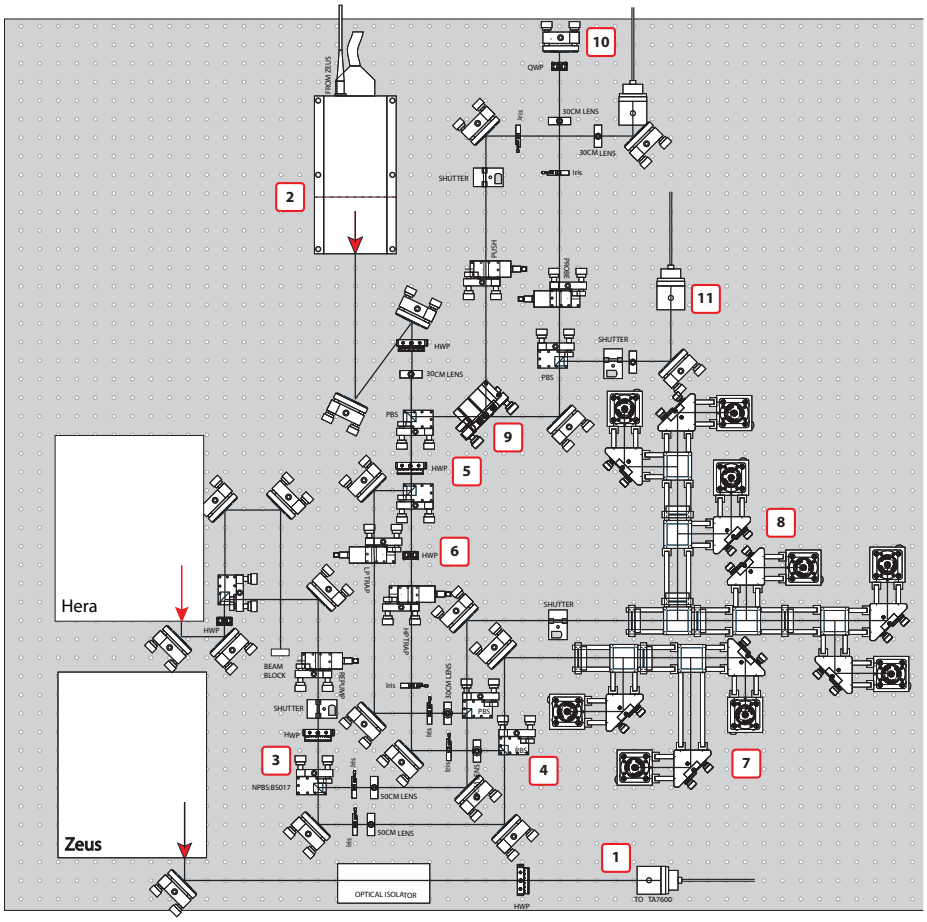

Figure 4.4: To-scale layout of the North table laser system. The distance between each hole on the optical table is 1 inch. North is at the bottom of the picture. See main text for a detailed description. Technical drawings by Thorlabs used with permission.

4.2 Laser sources

The three beam sources for the laser system were characterized and studied. Luckily few surprises were encountered, mostly concerning the tapered amplifier.

Early in the laser system's design process it was noticed that the Newport TA-7613 semiconductor tapered amplifier produced a beam profile that only became recognizably Gaussian at high power output. Consequently, beam profile measurements were completed at high power and using several sequential methods of attenuation: two HWP and PBS cube pairs plus one AR (anti-reflection) coated thick glass blank placed at about 45° angle of incidence, used in reflection. This brought the intensity of the beam

down to a level that did not saturate the beam profiler's CCD. It was found that the waist of the beam produced by the tapered amplifier is located about 7.7 cm behind the front face plate, with a roughly 1 cm mismatch between the horizontal and vertical profiles, with the horizontal waist profile being further from the face plate than the vertical profile waist. The minimum waist sizes were measured as 503 μm vertical and 545 μm horizontal.

Once the tapered amplifier's beam properties had been determined, it was necessary to ensure that the subsequent AOMs the beam would encounter were at or near a reasonably-sized beam waist. In this case, lenses from the Thorlabs catalog were considered and a 30 cm plano-convex lens was selected to re-create a waist of about 500 μm at a distance from the tapered amplifier that was not too great. To ensure that placing the lens in the wrong position would not result in an unsuitable waist size or position, the following calculation was performed. Consider a lens of focal length f placed at a distance d_1 from the TA. The transformed waist will be produced on the other side of the lens at a distance d_2. It is found from Gaussian beam matrix calculations that if $d_1 = f$, then $d_2 = f$. Otherwise,

$$d_2 - f = \frac{f^2}{z_1^2 + (d_1 - f)^2 (d_1 - f)} \tag{4.2}$$

with $z_1 = \pi\omega_{01}^2/\lambda$. ω_{01} is the incoming beam's waist, and it is also found that

$$\omega_{02} = \frac{f}{\sqrt{z_1^2 + (d_1 - f)^2}} \omega_{01}. \tag{4.3}$$

From these relations, it was calculated that for a 30 cm lens, if the lens is placed 10 cm away from the intended location (a conservative estimate given the accuracy of optics table measurements), then the transformed waist location would be 3 cm away from the expected location, and less than a μm different from its expected size. These results indicate that the placement of the collimating lens need not be extremely precise to render the beam suitable for AOM application.

The beam profiles of the diode lasers Hera (repump) and Zeus (TA seed laser) were measured, though only Hera's parameters will be reported here, as Zeus' beam ends its free-space life quite promptly, at a fiber coupler whose throughput is not vital, as long as it is above the minimum seed power requirements for the TA-7613 (about 10 mW). Hera was found to have a waist for its vertical profile near the location of the first folding mirror right after the beam exits the raised saturated absorption subassembly board, as is seen in Figure 4.4. The waist of its horizontal profile is located some 14-18 cm in front of this mirror. Both waists were found to be about 250 μm in size. The difference between horizontal and vertical waist positions is presumed to be due to anamorphic beam shaping optics inside the laser diode head, since the beam exiting from a laser diode is not in any way a symmetric Gaussian beam.

4.3 Saturated absorption locking

The diode lasers used in the experiment do not have the short or long term frequency stability required for atom trapping. The D2 line of ^{87}Rb has a linewidth $\Gamma_\nu = 6.07$ MHz [59] and thus long-term stability on the order of 1 MHz is required for trapping. In general terms, to be able to lock a laser to a specific frequency, some form of electrical signal (called an error signal) must be generated that is proportional to the deviation of the laser from the required frequency. Saturated absorption spectroscopy, as described by MacAdam, Steinbach and Wieman in 1992 [60] provides a physical system from which a useful error signal can be derived.

Saturated absorption spectroscopy is described in simple terms in Figure 4.5. It requires little alignment precision and optical beam quality. A probe laser **(a)** is shone through a glass cell containing natural atomic vapor at zero temperature. As the laser's frequency is scanned, the frequency will eventually match the resonance frequency of an atomic transition, the atoms will absorb the beam's photons, and these will be re-radiated by spontaneous decay in all directions. Consequently, at this frequency, energy is taken out of the probe beam and the photodiode voltage drops. If the atoms are allowed thermal motion, as in **(b)**, some atoms will see Doppler-shifted photons, and will begin to interact with the frequency-scanned probe beam before it has reached the actual resonance frequency. The resonance is said to be thermally broadened, and the photodiode signal is no longer representative of the true width of the atomic transition. If a counter-propagating saturation beam **(c)** is overlaid on the first beam and they are both of the same frequency, however, then *only* atoms with a negligible Doppler shift will interact with *both* beams when they are scanned over the true transition frequency. Since this same velocity class of atoms is interacting with two beams, it approaches saturation, and the probe beam's intensity is reduced less. This produces a sharp, "Doppler-free" feature in the photodiode signal.

The actual situation presented by ^{87}Rb is a little more complex than Figure 4.5 suggests, since the D2 line contains more than one $F \rightarrow F'$ hyperfine transitions with a common ground state. This results in the appearance of crossover peaks on the saturated absorption spectrum. For every pair (ν_1, ν_2) of hyperfine transitions that share a common ground state, a peak appears at the intermediate frequency $(\nu_1 + \nu_2)/2$. This is illustrated in Figure 4.6. The figure on the left represents the photodiode voltage as a probe laser's frequency is scanned over two hyperfine transitions that share a common lower state in the same setup as Figure 4.5 **(a)**, at zero temperature. If the transitions are Doppler-broadened to the extent that they overlap at nonzero temperature, as on the right, a peak in the PD voltage signal appears at a frequency $(\nu_1 - \nu_2)/2$ halfway between the two transition frequencies. To understand this extra

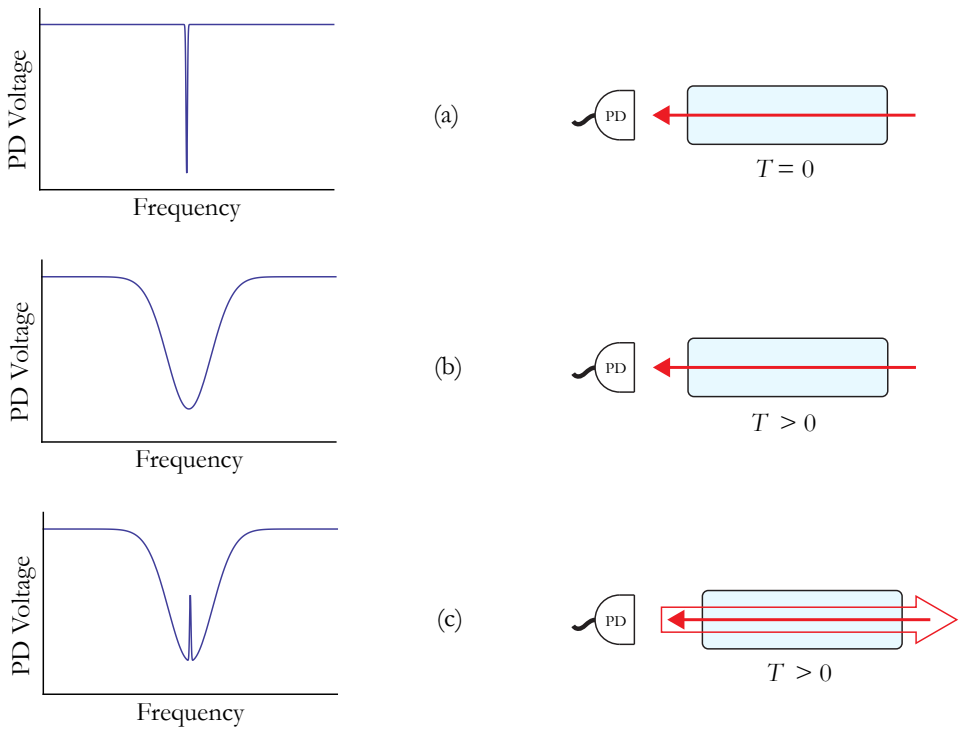

Figure 4.5: A simple illustration of how saturated absorption spectroscopy works for a single atomic transition.**(a)** A probe laser is shone through a glass cell containing natural atomic vapor at zero temperature. **(b)** The same, but at nonzero temperature. **(c)** A counter-propagating saturation beam is overlaid on the first beam. This produces a sharp, "Doppler-free" feature in the photodiode signal.

peak, consider atoms that move towards the saturation beam and are Doppler-shifted into resonance with the higher-frequency transition. Only one velocity class of all these atoms will also be at the right frequency to be Doppler-shifted *down* to the counter-propagating probe beam, as well. Since these two transitions share a common ground state, atoms in this velocity class are less likely to be found in the ground state by the probe beam, reducing the energy taken out of the probe beam by the atom vapor at this frequency.

A photograph of the Doppler-broadened saturated absorption spectrum used in the experiment is shown in Figure 4.7.

Once a satisfactory saturated absorption spectrum is obtained, the next step is to derive an error signal from it. A simple method (not used in our experiment) is to use the side of one of the saturated absorption peaks as an error signal. If the laser frequency is manually set to the side of one of these

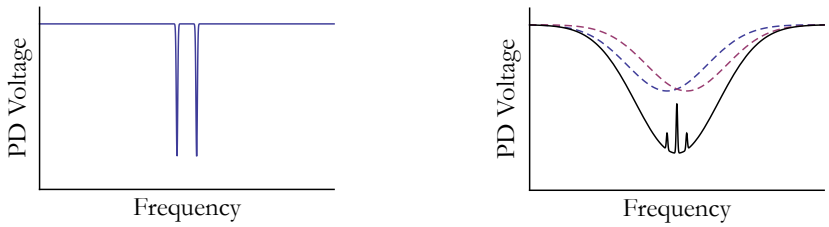

Figure 4.6: Crossover transitions in saturated absorption spectroscopy. **Left**: PD voltage as a probe laser's frequency is scanned over two hyperfine transitions that share a common lower state at zero temperature. **Right**: The same, but at non-zero temperature.

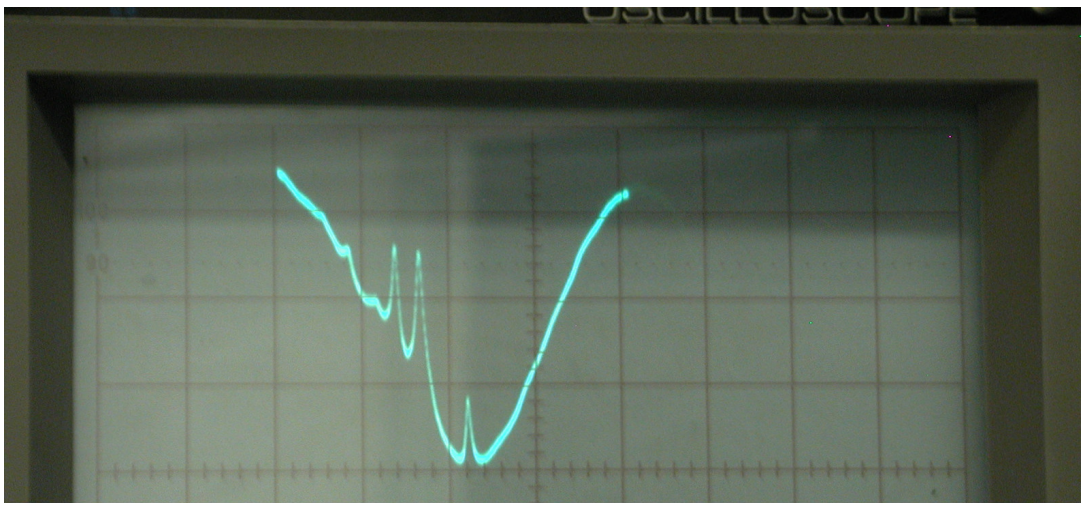

Figure 4.7: Photograph of oscilloscope displaying saturated absorption spectrum. In this case, the laser frequency sweeps out the Doppler-broadened manifold of the $F = 2 \rightarrow F' = 1, 2, 3$ hyperfine transitions of ^{87} Rb.

peaks, an increase or decrease in laser frequency, produced by environmental factors, will result in a proportional increase or decrease in the photodiode voltage signal. This is then the error signal, and can be fed into a servo control loop that attempts to restore the laser back to a zero error signal via external inputs that alter the laser's frequency. Though effective and simple, this method is susceptible to any effect that may cause the photodiode voltage to rise yet is not a result of the laser frequency changing. Laser amplitude drift, for example, will have this effect, and cause the lock point to drift over time as well.

A better option is to derive an error signal from a saturated absorption peak by other means, hopefully in a way that isolates the error signal from amplitude and other sources of noise. If the laser frequency is modulated sinusoidally at low amplitude (much less than an atomic linewidth) and

high frequency, usually on the order of tens of kHz, then generally speaking, if the laser's frequency has drifted to a lower frequency (it is on the left of a saturated absorption peak), this modulation signal will appear on the photodiode voltage as a sinusoidal modulation that is in phase with the input modulation. If, on the other hand, the laser's frequency has drifted to a higher frequency (it is on the right of a saturated absorption peak), the modulation signal will appear 180° out of phase with the input modulation. Essentially, the photodiode voltage becomes proportional to the *derivative* of the saturated absorption feature,

$$V_{\text{out}} \propto V_{\text{in}} \frac{\partial V_{\text{out}}}{\partial V_{\text{in}}} \tag{4.4}$$

where the partial derivative is taken at the particular point on the saturated absorption feature the laser happens to be on.

This can be achieved with a lock-in amplifier (LIA). A lock-in amplifier is an apparatus that can perform phase-sensitive detection of very small AC signals in the presence of large amounts of noise. Suppose that the LIA generates an internal reference square wave of frequency ω_{ref} (used only internally). From this reference square wave, a sinusoidal voltage signal of amplitude V_{ref}, frequency ω_{ref} and phase shift θ_{ref} is generated. If this signal is fed into the laser as a modulation signal, the laser's frequency will be modulated at frequency ω_{ref}. At the other end, the photodiode signal will also be modulated at the same frequency, but naturally with its own amplitude V_{sig} and phase shift θ_{sig}. These two signals, the modulation and the external photodiode signal can be multiplied internally by the LIA:

$$V_{\text{LIA}} = \Big[V_{\text{sig}} \sin(\omega_{\text{ref}} t + \theta_{\text{sig}})\Big] \times \Big[V_{\text{ref}} \sin(\omega_{\text{ref}} t + \theta_{\text{ref}})\Big] \tag{4.5}$$

$$= \frac{1}{2} V_{\text{sig}} V_{\text{ref}} \Big[\cos(\theta_{\text{sig}} - \theta_{\text{ref}}) - \cos[(\omega_{\text{ref}} + \omega_{\text{sig}})t + \theta_{\text{sig}} + \theta_{\text{ref}}]\Big]. \tag{4.6}$$

If a low-lass filter is applied to V_{LIA} the second high-frequency term is eliminated, and what is left is a DC signal proportional to the signal voltage.

$$V_{\text{LIA}} = \frac{1}{2} V_{\text{sig}} V_{\text{ref}} \cos(\theta_{\text{sig}} - \theta_{\text{ref}}). \tag{4.7}$$

If θ_{ref} is manually adjusted such that $\theta_{\text{sig}} - \theta_{\text{ref}} = 0$, then

$$V_{\text{error}} = \frac{1}{2} V_{\text{sig}} V_{\text{ref,}} \tag{4.8}$$

and the LIA's output will be maximized.

V_{error} can then be used as the input error signal for an integrator circuit, whose output is proportional to the integrated error signal over some time constant τ:

$$V_{\text{correction}} = -\int_0^t \frac{V_{\text{error}}}{\tau} dt. \tag{4.9}$$

In this way, the corrective voltage applied to the laser head's frequency control input ($V_{\text{correction}}$) is proportional to the size and sign of the error signal V_{error} and its integral over time. The time constant of the integrator circuit is made as small as possible before feedback oscillations take control of the locking system.

In the LANL BEC setup the diode lasers are not locked and modulated by means of the same mechanism. The laser controller box accepts two inputs that modulate the laser's frequency. The first is a voltage-controlling input that determines the voltage added or subtracted to the diffraction grating's piezoelectric mount. This input accepts ±4.5 V from DC to 3.5 kHz at a default gain of 25. The lasers' frequency response can be calculated from the manufacturer-supplied test data sheet. Zeus (Hera) has a response of 41.1 (40.0) GHz/V calculated over the entire 117 V range of the piezo actuator. Taking into account the 50 Ω output impedance of the Stanford Research Systems SR830 Lock-In Amplifier and the 5 kΩ input impedance of the voltage control input on the laser control box, a simple voltage divider was constructed and placed before the voltage control input. For Zeus (Hera), the series resistance used was 366.4 kΩ (366.9 kΩ) for a calculated frequency response of 55.5 MHz/V (53.6 MHz/V).

The other input controls the current fed to the laser diode. This changes the frequency of the laser by altering the index of refraction of the laser gain medium. Since this value varies a lot from diode to diode, the frequency response through this input was measured. A Melles-Griot Fabry-Perot (model 13SAE025, 2 GHz free spectral range) scanning cavity was used to obtain a resonance feature of known slope on a monitoring oscilloscope. This same feature was used to determine the laser frequency change produced by a known input on the laser's current control input. The 50 Ω output impedance and 5 kΩ input impedance of the current control input were taken into consideration for the construction of a simple voltage divider box placed before the current control input. The series resistance used on Zeus (Hera) for this voltage divider was 99.45 kΩ (100.1 kΩ) for a response of 1.45 MHz/V_{pp} of modulation. In this way a front panel indication of 0.2 V_{RMS} modulation on the SR830 lock-in amplifier's sine output results in a 0.7 MHz (peak-to-peak) modulation on the lasers' frequency. As a point of reference, this is about 20% of the width between the ^{87}Rb Lorentzian feature's inflection points and about 12% of the linewidth.

With these input conditioning boxes, both lasers are satisfactorily locked to their respective peaks in the ^{87}Rb saturated absorption spectrum.

4.4 On fiber coupling efficiency

The main concern during the design of the beam divider system, detailed in Section 4.5, was being able to couple light into the optical fibers in a way that allowed even power sharing between all 3 and 6 outputs of each divider. Each fiber coupling port has limited ability to compensate for a beam that is off-axis or entering at an angle, but given prior experience with the PAF-X-5-B's x-y adjustment screws, it was decided that two steering mirrors per port would allow a a much easier coupling (and re-adjustment) process.

The other issue that could pose a problem was the range of distances that each port would be from the repump/trapping beams' waist. Before purchasing and construction could be initiated, the impact of waist position on coupling efficiency needed to be determined.

The figure that quantifies this coupling efficiency is the mode matching efficiency

$$\eta = \frac{|\int E_1^* E_2^* \, dA|}{\sqrt{\int |E_1|^2 \, dA \int |E_2|^2 \, dA}} \tag{4.10}$$

for the overlap of two electric fields, where dA is an area element taken in a plane parallel to the field vectors. We will interpret the second electric field as that which is *expected* by the fiber coupling port.

We will treat the case where both beams are collinear and they differ only in waist size and location, since it is assumed that any lateral or angular deviation can be compensated by the steering mirrors and fiber coupler adjustment screws.

A single-mode Gaussian beam's electric field E_1 is described by

$$E_1(r,z) = E_{01}\frac{\omega_{01}}{\omega_1(z_1)} \exp[-r^2/\omega_1^2(z_1)] \exp[-i(kz_1 - \arctan z_1/z_{01} + kr^2/2R_1(z_1)]. \tag{4.11}$$

where the standard notation of $\omega_1(z_1)$ as the $1/e$ amplitude radius or beam waist, ω_{01} as the minimum waist, and z_0 as the Rayleigh range has been used. We begin working through Equation 4.10 by noting that[1]

$$\int |E_1|^2 \, dA = |E_{01}|^2 \frac{\omega_{01}^2}{\omega_1^2(z_1)} \int_0^\infty r \exp\left[-(2/\omega_1^2(z_1))r^2\right] \, dr d\theta \tag{4.12}$$

$$= |E_{01}|^2 \omega_{01}^2 \frac{\pi}{2}, \tag{4.13}$$

and thus it follows that the denominator of Equation 4.10 is

$$\sqrt{\int |E_1|^2 \, dA \int |E_2|^2 \, dA} = |E_{01}||E_{02}|\omega_{01}\omega_{02}\frac{\pi}{2}. \tag{4.14}$$

[1] Given that $\int x e^{-cx^2} dx = -e^{-cx^2}/2c$. Evaluated between zero and infinity results in $1/2c$.

On the other hand,

$$E_1^* E_2 = E_{01}^* E_{02}^* \frac{\omega_{01}\omega_{02}}{\omega_1(z_1)\omega_2(z_2)} e^{-\left(1/\omega_1^2(z_1)+1/\omega_2^2(z_2)\right)r^2} e^{i(\cdots)} e^{i\frac{k}{2}(1/R_1(z_1)-1/R_2(z_2))} \tag{4.15}$$

$$= E_{01}^* E_{02}^* \frac{\omega_{01}\omega_{02}}{\omega_1(z_1)\omega_2(z_2)} e^{i(\cdots)} \exp\left[-\left\{\left(\frac{1}{\omega_1^2(z_1)}+\frac{1}{\omega^2(z_2)}\right)+i\frac{k}{2}\left(\frac{1}{R_2(z_2)}-\frac{1}{R_1}\right)\right\}r^2\right]. \tag{4.16}$$

The exponential whose argument is merely an ellipsis contains no r dependence, and thus will disappear when the modulus is taken following integration. Performing the integration leads to

$$\int E_1^* E_2 \, dA = \tag{4.17}$$

$$E_{01}^* E_{02}^* \frac{\omega_{01}\omega_{02}}{\omega_1(z_1)\omega_2(z_2)} e^{i(\cdots)} 2\pi \left[\frac{1}{2}\left(\frac{1/\omega_1^2(z_1)+1/\omega_2^2(z_2)}{\left[1/\omega_1^2(z_1)+1/\omega_2^2(z_2)\right]^2+\frac{k^2}{4}\frac{(R_1(z_1)-R_2(z_2))^2}{R_1^2(z_1)R_2^2(z_2)}}\right)+i\,(\cdots)\right]. \tag{4.18}$$

After taking the modulus and carrying out extensive algebraic simplification of terms we arrive at

$$\eta = \frac{|E_{01}^* E_{02}|}{|E_{01}||E_{02}|} \frac{2}{\sqrt{\frac{(\omega_1^2+\omega_2^2)^2}{\omega_1^2\omega_1^2}+\frac{k^2}{4}\frac{(R_1-R_2)^2}{R_1^2R_2^2}\omega_1^2\omega_2^2}}. \tag{4.19}$$

We will assume that the coupling mode the fiber coupling port "expects" is flat. In other words, the best possible coupling is achieved by placing the incoming beam's minimum waist at the coupling lens. This is equivalent to assuming $z_2 = 0$, $\omega_2 \to \omega_{02}$ and $R_2 \to \infty$. We will also take, in what follows, the field amplitudes as being equal. η can now be considered a function of three variables:

$$\eta(d,\omega_{01},\omega_{02}) = 2\left[\left(\frac{1}{\omega_1(d)^2}+\frac{1}{\omega_{02}^2}\right)^2+\frac{k^2}{4}\frac{\omega_1^2(d)}{R_2(d)^2}\omega_{02}^2\right]^{-1/2}. \tag{4.20}$$

If the separation between the coupler and the incoming beam's waist location is written as a function the coupler's ideal beam Rayleigh length, that is $d = \alpha z_{02}$, and the incoming minimum waist size is written as a function of the coupler's optimal waist size, $\omega_{01} = \beta\omega_{02}$, then

$$\eta(d = \alpha z_{coupler}, \omega_{beam} = \beta\omega_{coupler}) = \frac{2\beta}{\sqrt{\alpha^2+(1+\beta^2)^2}}. \tag{4.21}$$

The ideal situation, as one might expect, is $\alpha = 0$ and $\beta = 1$.

We are now equipped with the tools to determine if a design like that used in Section 4.5 will work. The two limit cases of interest are coplanar ($z_1 - z_2 = 0$) waists and equal waists ($\omega_{01} = \omega_{02}$). Figure 4.8 plots Equation 4.21 for different locations and sizes of the incoming beam's waist. As a result of this calculation it is evident that placing the incoming beam's waist about one Rayleigh length away from the coupler and even mismatching the expected waist size by 50% will still get a very acceptable

coupling coefficient. As a point of reference, for a 780 nm Gaussian beam of waist 500 μm, the Rayleigh range is about 1 m. This result allowed us to move forward with the design and construction of the 1 to 3 and 1 to 6 beam dividers.

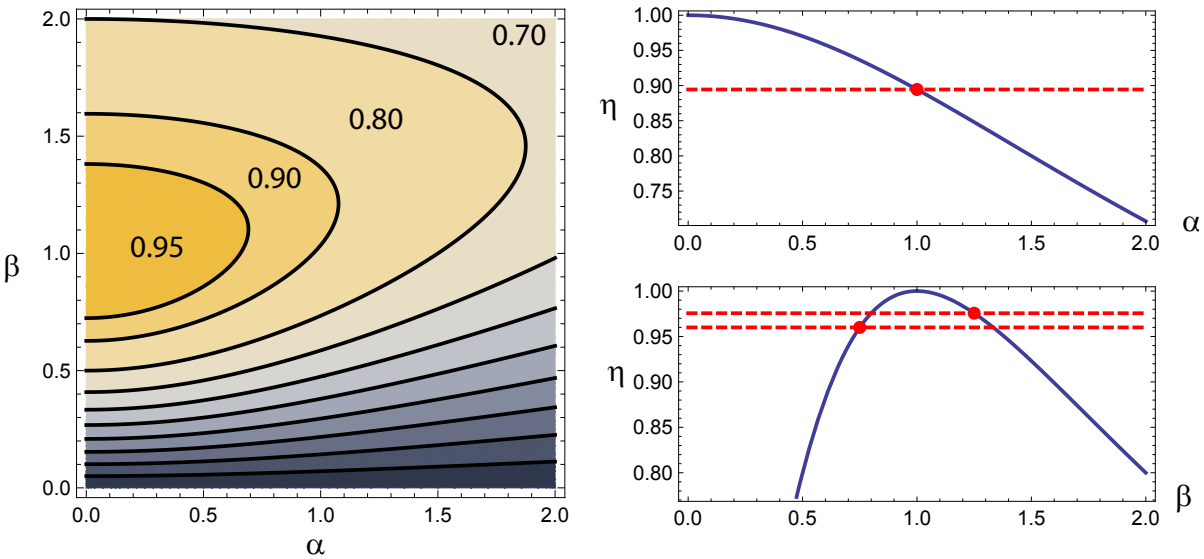

Figure 4.8: Predicted coupling efficiency η for an on-axis Gaussian beam of waist β times the coupler's optimal waist that is placed at a distance αz_{02} from the coupler face. The top right plot takes the incoming and expected waists as equal. The red dot marks the efficiency that is attained when the incoming waist is placed one coupler Rayleigh length away from the coupler. Here $\eta = 2/\sqrt{5} = 89\%$. The bottom right plot, on the other hand, takes the incoming beam's waist as coplanar with the coupler face, but shows the variation in η as the size of the beam waist is varied. The red dots mark the efficiency when the waist is made 25% larger and 25% smaller than the coupler's expected size. The efficiency in this range is always above 95%. The contour plot illustrates this quite broad acceptance range.

4.5 1 to 3 and 1 to 6 beam dividers

A double MOT setup has advantages over other approaches to making a BEC, but it does require a rather large amount of beams. Each beam has to be power balanced precisely versus the others impinging on the trap, and the power requirements for each set of MOT beams may well be different. Considering the relative atomic densities encountered in the traps in the LANL BEC experiment, one can get away with having only three incoming beams for the high pressure MOT, which are then retro-reflected back towards the atoms, but one cannot do the same for the low pressure MOT. This means a total of 9 beams must be created from one source of trapping light and one source of repump light.

The beams that end up going to each MOT are split early on in the beam path using a straightforward half wave plate/PBS combination. The problem arises when each of these two beams must then be split into three and six beams. The first way of doing this that was considered was using ordinary beamsplitting materials: plates, pellicles and so on. The problem is that off-the-shelf splitters behave far from their theoretical ideal when one uses polarized light. Compounding the problem is the fact that each MOT beam was a collinear arrangement of trapping light, with a vertical linear polarization, and repump light, with a horizontal linear polarization. The main problem, however, is simply one of arithmetic: creating three equal beams from a single source beam requires a beamsplitter with a 33:66 ratio and one with a 50:50 split ratio. The former was not readily available and the latter was not enough, on its own, to achieve the ratios needed. Figure 4.9 illustrates the problem posed by attempting to split two overlaid beams with orthogonal polarizations with a 50-50 beamsplitter. Beamsplitters were thus ruled out, and pairs of half wave plates and polarizing beamsplitter cubes were chosen.

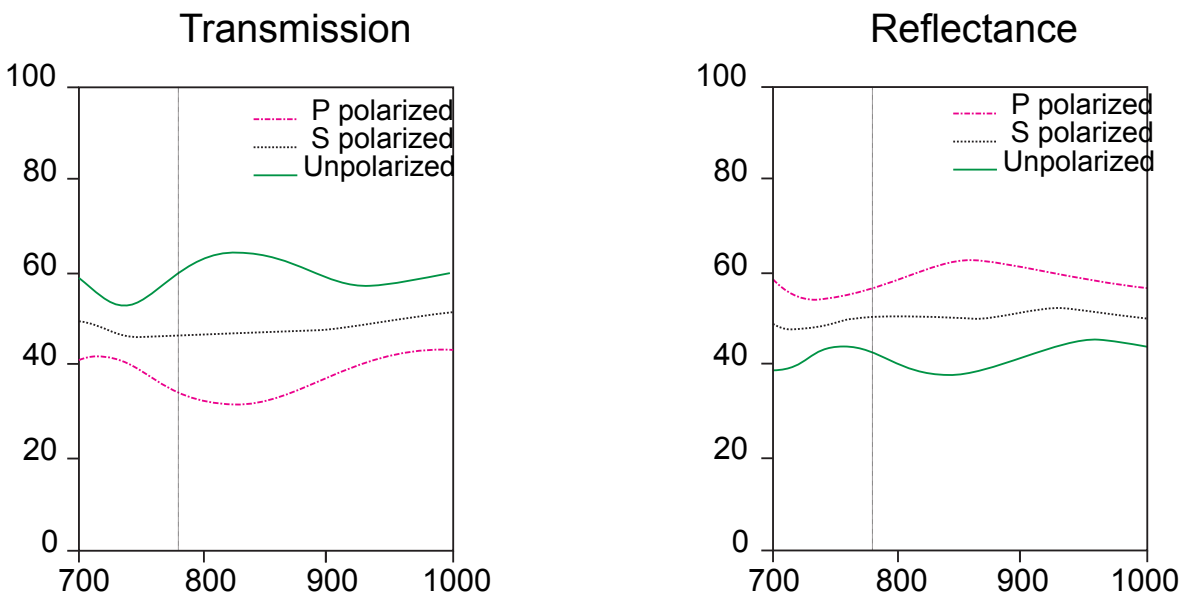

Figure 4.9: Performance of Thorlabs' UV Fused Silica Plate Beamsplitters for use with 700 - 1100 nm light. The vertical dashed line marks the 780 nm point. At this wavelength, P (S) polarized light is transmitted at about 55% (43%) and reflected at about 35% (60%). Data from [61].

For the actual mechanical construction, several options were considered. The most obvious solution, an arrangement of free-space optics, was deemed potentially susceptible to the cumulative effects of element-by-element thermal creep, vibration and accidental mechanical mis-adjustment. Self-contained solutions were surveyed, and two product families were considered. Miniature FiberTable and Fiber-

Bench systems from Thorlabs/OFR offered the advantage of a very small physical footprint, but despite extensive assistance and help from the manufacturer, these were ultimately not chosen due to concerns over the ability to adjust and direct beams accurately towards the fiber couplers, given difficulty encountered through experience in adjusting the PAF-X-5-B's X-Y screws.

Thorlabs' 30 mm Cage System was chosen instead. This modular combination of rods and standardized optical component holders is described by the manufacturer as "four rigid steel rods on which optical components can be mounted along a common optical axis". What was most attractive about this setup is that, once assembled, all relative distances and alignments would remain fixed (up to thermal effects, naturally). Figure 4.10 illustrates the final design. Note that in this top-down view, the fibers rise out of the page. What is not apparent in this drawing is that there are 6 extra PBS cubes placed immediately before certain fiber couplers. These were added to every sub-beam that originates from a PBS cube in reflection, but not transmission. The reason for this has to do with the polarization issues that were encountered once the system had been put in operation, and this will be covered in the next Section.

4.6 Polarization issues

A certain time after the beam divider had been placed in operation, it was noticed that the brightness, and hence the atom number, of the atom cloud in both MOTs was not stable. Indeed, the atoms could be observed being trapped in the MOT, attaining a certain level of brightness, and then slowly fading over the course of a minute or so. The issue affected both MOTs, but not in a synchronized way. The issue was roughly cyclic, but with no apparent fixed period. Possible causes were eliminated one by one, until the problem was traced to how the various elements in the beam divider, optical fiber and beam expander interacted with the incoming beam's polarization. To understand the issue fully, it is necessary to review some basic facts about polarized beamsplitting cubes and polarization-maintaining fiber.

The type of fiber chosen for the laser system was polarization-maintaining single-mode fiber (Thorlabs P3-780PM-FC-5 patch cords). Polarization-maintaining fiber is available in several types, but the type used was of the Panda type. This means that the core of the fiber is stressed laterally via stress rods laid parallel to the core. This produces a birefringent medium, and the intent is to inhibit crosstalk between the two propagating polarization modes in the fiber. If linearly polarized light is launched into the fiber, generally parallel to the medium's slow axis, it will remain polarized to a high degree at the

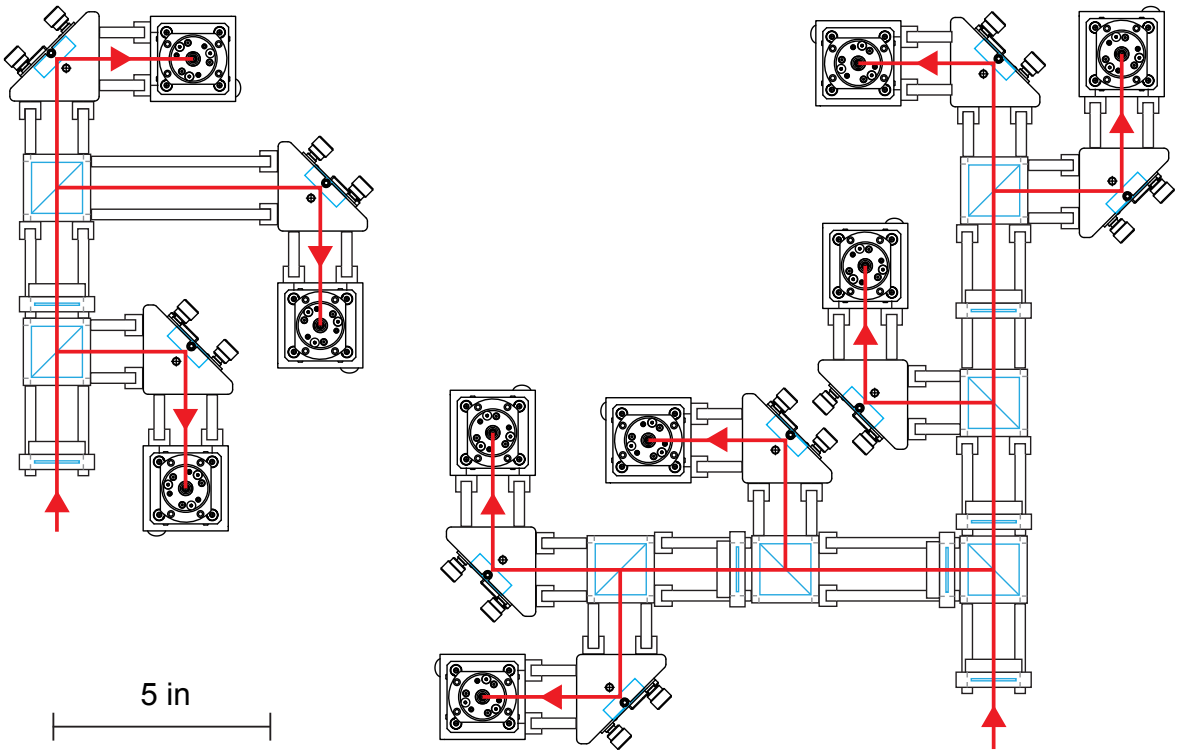

Figure 4.10: HP (left) and LP (right) beam dividers, top view. Overlapped repump and trap beams are split into 3 and 6 sub beams for fiber coupling. Ratios are controlled by half wave plate and polarizing beamsplitter cube pairs. The final trajectory of every sub beam involves two steering mirrors. In the case of sub beams that *reflected* off the last PBS in their path, an extra polarizing beamsplitter cube (not shown due to the top-down view) is placed before the fiber coupler. This extra PBS cube ensures that the polarization of the coupled light is as linear. Technical drawings from Thorlabs used with permission.

output. No guarantee is made, however, about the *relative phase* between each polarization axis, and this phase will depend mostly on the mechanical and thermal stresses the fiber is subject to.

The problem encountered with the initial design of the laser system stemmed from two oversights: care was not taken to align each fiber coupler's axis with the polarization axis of the incoming light and, more importantly, not all fiber coupling ports were provided with highly linearly polarized light. This latter situation was due to the use of polarizing beamsplitter cubes to control the ratio of light directed to each fiber coupling port. PBS cubes are inherently better at *transmitting* one polarization (V) over the other, with an extinction ratio of over 1000:1, but are not so good at *reflecting* one polarization (H) only, where the extinction ratio is closer to 100:1. Since many fiber ports are at the end of a sub-beam originating from the reflection off a PBS cube interface, these sub-beams will not be entirely H polarized.

This problem is not such an issue for the fiber coupler ports that obtain their sub-beam from a PBS cube used in *transmission*.

Luckily, a near infra-red (NIR) polarimeter was available, and a test case was set up to explore the situation. A half wave plate was placed before a PBS cube, and the polarization state of the reflected light was observed for two different split ratios: a 0.34 split ratio and a 0.50 split ratio, as is encountered in the beam divider setup. In terms of the azimuth angle (the angle formed between the major semi-axis of the polarization ellipse and the x axis) and the ellipticity, the major to minor axis ratio, it was found that an even split produced light with an azimuth angle of 85.5° and an ellipticity of 5.5°. A 33:66 split resulted in an azimuth angle of 84.6° and an ellipticity of 6.7°.

Adding a second PBS cube so that the light emerging from the first cube was transmitted (with the intent of attaining a higher degree of polarization) improved these parameters to 89° azimuthal angle and 0.9° ellipticity for the 50:50 split and 89.1° azimuth angle and 0.9° ellipticity for the 33:66 split. Given these results, a second PBS cube was added to all fiber couplings ports taking light from a PBS cube in reflection.

The new setup was aligned and tested with the aid of the polarimeter and associated software. In particular, the program offered a mode which traced out the polarization state of the measured light on a Poincaré sphere, recording at a rate of about 30 samples per second. As each fiber was mechanically and thermally stressed (using force applied by a hand or the warmth transmitted by holding a segment of the fiber in a tight fist), the relative phase between the two polarization modes transmitted by the fiber changed. This change caused the polarization state of the emerging light to trace out a small circle on the Poincaré sphere. The size of this circle is related to the extinction ratio of the fiber optic setup as follows:

$$\mathrm{ER} = 20 \log \frac{1}{\tan |\eta|_{\max}}, \tag{4.22}$$

where η is the ellipticity of the emerging light as defined above. Aligning the fiber coupling port very carefully to the incoming light while monitoring the extinction ratio allowed us to greatly reduce the susceptibility of the fiber system to thermal or mechanical stresses. All ports were left in a final configuration that allowed no less than 24 dB of ER.

After implementing these changes and adjustments, the issues with the MOTs were no longer present, and the development and reconstruction of the LANL BEC experiment could proceed.[2]

[2]It is interesting to note that two types of fiber were encountered. One was susceptible to mechanical stress, to the extent that merely touching the optical fiber anywhere along its length would make the polarization state on the Poincaré sphere trace out its circle extremely rapidly, indicating rapid changes in phase between the two

4.7 Summary

An all-new laser system was designed and constructed. This system satisfies the design requirements of mechanical stability and de-coupling from the main BEC machine apparatus via single-mode fiber coupling, as well as providing enough laser power for large-diameter MOT beam operation. The feasibility of dividing two main beams and coupling them into three and six fiber couplers, all at different locations from the main beam waist position, was studied and found to be achievable. Issues stemming from an improper fiber rotational alignment were analyzed and resolved.

birefringent modes of the fiber. The other type encountered was extremely insensitive to mechanical stress, but holding the fiber in a clenched palm would set the polarization state slowly rotating around the circle it traced on the Poincaré sphere. Despite sequential serial numbers on the Thorlabs patch cords, no correlation to any external property of the fibers was determined, and Thorlabs Support was unable to offer an explanation.

Chapter 5

Optics

As mentioned previously, one of the motivations for constructing a new and improved BEC machine (and, later, integrating these improvements into the current experiment) was to improve the optical capabilities of the entire system. The previous chapter has addressed the steps that were taken to provide stable, powerful, fiber-coupled light for the BEC experiment; this chapter details the systems that were constructed to bring that light to bear on the BEC. Section 5.1 covers the design of the new beam expanders and retro reflectors, and Section 5.2 discusses the addition of a motorized linear stage to aid in tweezer beam focusing.

5.1 Beam expanders and retro-reflectors

The experiment's beam expanders were designed from scratch to accomodate the new optical fiber system. The main objective was to obtain larger beams via a compact physical unit, since experience had shown that physical access to the experiment soon becomes difficult once all the ancillary optical, magnetic and support mechanisms are in place. Whatever the final design, the beam expanders had to accommodate a fiber connection mechanism, a quarter wave plate for circular polarization and the necessary optics for beam shaping, while allowing easy manual adjustments to focal lengths.

Beam diameter for the HP expanders and retro-reflectors was a definite design priority, since the number of atoms trapped in a MOT varies roughly as the diameter of the beam raised to an exponent of about 3.6 [62]. This strong dependence on beam diameter is a result not only of the MOT cross sectional area, proportional to D^2, but also to the distance an incoming thermal atom is subjected to

the effect of optical molasses, a velocity-dependent force.

Figures 5.1 and 5.2 give a detailed view of the LP and HP expanders and their components. The HP retro-reflector was designed with a small diameter back end to avoid using excessively large (and, consequently, expensive) quarter wave plates. Concern over issues that might arise from having a sharply converging beam pass through a quarter wave plate were also addressed with this design. Physical compactness proved satisfactory, though the unused back end of one of the HP expanders had to be hacksawed off with no apparent effect on mechanical stability of the element stack.

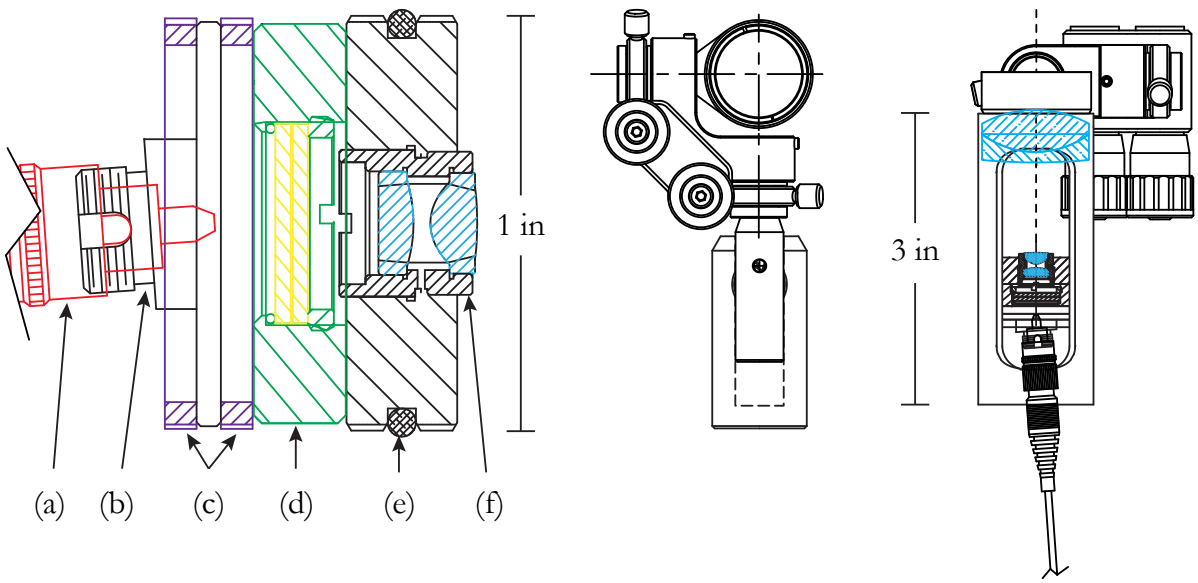

Figure 5.1: LP MOT beam expander. **Left**: A side view of the main components of the beam expander. The outer threaded tube (SM1L30C) is not shown, nor is the front f = 40 mm lens element (AC254-040-B). A connectorized fiber optic **(a)** (P3-780PM-FC-5, red) connects to an unthreaded fiber connection plate **(b)** (S1FCA, black) held in place by two threaded retaining rings **(c)** (SM1RR, purple). Next is a mounted multi-order quarter-wave plate **(d)** (WPMQ05M-780, green), which is not threaded, but is held tightly in place by the aspheric lens pair assembly **(d)** (C230260P-B lens and S1TM09 holder), which is threaded. **Center**: A view along the optical access of the beam expander (note the scale change) mounted to its gimbal mount (GMB1) which is itself mounted on a 2 in post and post holder. **Right**: Top view of LP beam expander. The slotted outer tube allows a view of the element stack described in the first illustration. Also shown is the gimbal mount. Technical drawings from Thorlabs used with permission.

The stack of elements used in both expanders requires no adjustment other than its location along the tube it is mounted in (via rotation, since the inside of the tube is threaded). This is due to a coincidental matching of the fiber ferrule location and the expected input position of the aspheric lens

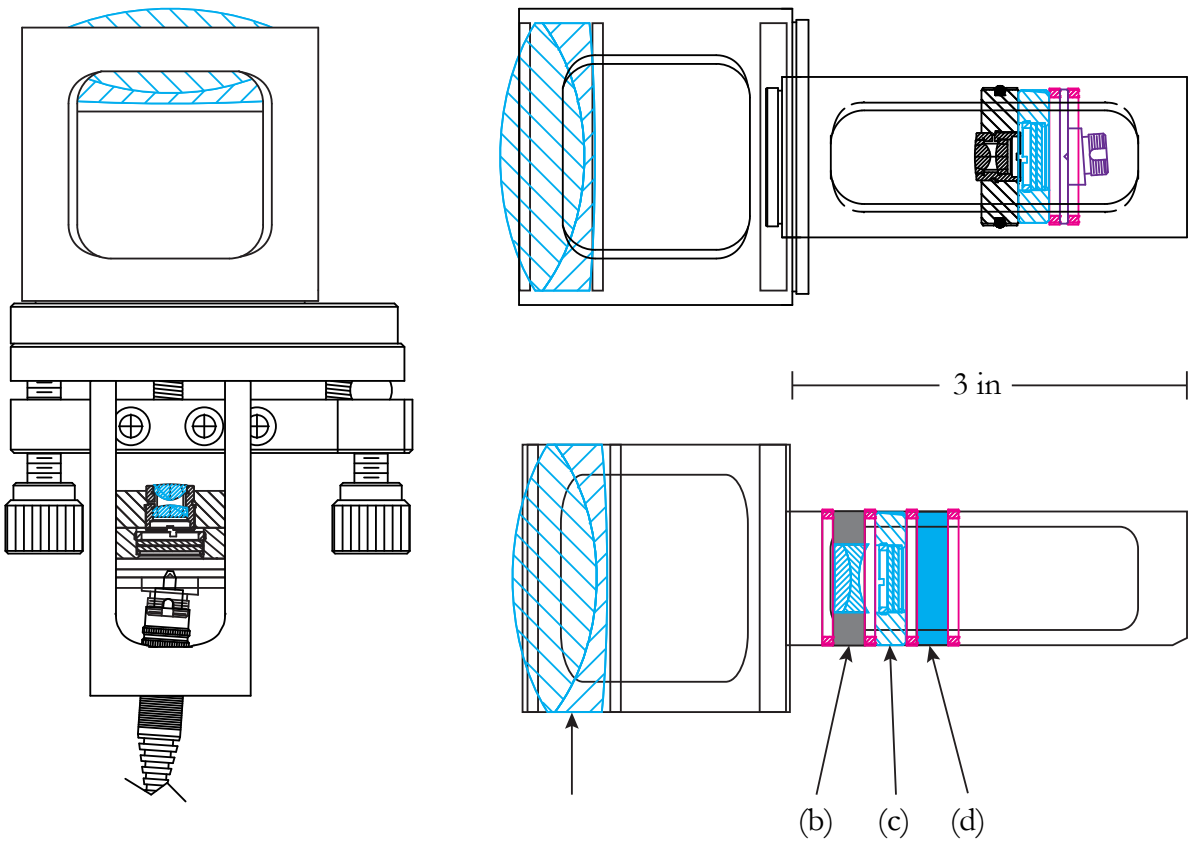

Figure 5.2: HP MOT beam expander and retro-reflector. **Left**: The element stack used in the HP expander is identical to that used in the LP expander. The only difference is that the f = 80 mm front lens element (AC508-080-B) is mounted in a 2 in diameter slotted tube (SM1L30C) and connected to the 1 in diameter slotted tube via a zero-length adapter plate (SM2A6). It is shown here mounted to a 2-axis kinematic mount (KM200T). **Right, top**: HP expander, top view. **Right, bottom**: HP retro-reflector. The same front element as the expander **(a)** is used, but an f = - 20 mm achromat collimates the incoming light **(b)** (ACN127-020-B) through a quarter-wave plate **(c)** and onto a coated dielectric mirror **(d)** (BB1-E03). Technical drawings from Thorlabs used with permission.

pair once all elements are in place. The slots along the side of the mounting tube provide easy finger access for quick adjustment.

The short physical size of the beam expanders is due, in large part, to the large numerical aperture possible with the aspherical lens pair (NA = 0.4). This allows the front achromat element to intersect the diverging beam closer to the stack.

It was found that the LP expanders pass about 86% of the power coming out of the fiber to the collimated beam. The efficiency is lowered, naturally, because the front optic and mounting tube clip

the outer edges of the Gaussian beam.

The HP expander was adjusted to produce a collimated beam. The measurements to ensure this was the case were taken at a few tens of centimeters from the expander, and again at a few meters. It was found that the Gaussian diameter ($2\omega(z)$) was (near/far) 32/33 mm, with a hard cutoff at 49/59 mm. The peak intensity at each location differed by no more than 0.3%. As a point of comparison, the original Sussex-era LANL BEC HP MOT beams were 23 mm in diameter [53].

The good collimation obtained with this design proved useful during the final assembly of the system, as one HP MOT beam expander is placed about 30 cm from a chamber window, allowing a photodiode/lens system to observe the MOT's luminosity along a very close line of sight.

This beam was passed through an AR-coated conflat vacuum window identical to those used in the experiment and it was found that, after focusing the emerging beam down onto a power meter, the total power transmitted from optical fiber to the other side of the window was 73%, down from 82% before the window. This discrepancy was mostly due to beam clipping.

The LP expanders' collimation was not tested out to such a large distance, using only the rough distances that would be encountered around the LP quartz cell. A Gaussian diameter of 21 mm at 30 mm from the front of the expander and a Gaussian diameter of 22 mm at 53 mm distance was measured. The quartz cell allows a 25 mm clear aperture when a beam impinges perpendicularly on its sides (this is the case for only 2 out of 6 beams, as seen in the previous chapter). This clear aperture, however, is larger than the aperture of the slotted tube that holds the LP expander components, which is 24 mm, which clips the LP MOT beam slightly. The final configuration of 4 out of the 6 LP beam expanders was actually further away from the BEC than these distances, but due to the ease with which collimation (at the expander) and power (at the divider) can be adjusted for each beam, a balanced, collimated set of beams were produced nonetheless.

The HP retro-reflectors were calibrated using a beamsplitting pellicle and a 1:1 retro-reflection was set at a distance of about 20 cm.

5.2 Motorized stage for the tweezer beam

Prior to the overhaul of the LANL BEC system, the position of the Mitutoyo optic, responsible for tweezer beam focusing and BEC imaging, was done entirely manually. The idea of using a motorized linear stage to position the optic along its axis arose when it was found that the MOT beams in the

vertical plane would have to cross at an angle wider than 90° (Section 3.2, Chapter 3). If the optic could be raised and lowered during each experimental cycle, perhaps this angle could be kept closer to 90°. In the end this was not done, but the advantage of being able to position the waist of the tweezer beam with great precision and remotely was found to be reason enough to adopt a motorized stage for vertical positioning.

Unfortunately, space near the LP quartz cell is already quite tight and it was necessary to carefully consider the installation of the motorized stage. All the optics used for the dipole beam light sheet, tweezer beam and imaging camera are installed on the same side of the quartz cell. In Figure 2.3 of Chapter 2, this would be on the upper side of the system in the top down view. Nothing is installed at the height of the optics table, however. Two raised breadboards, one stacked above the other, provide enough surface area to house all optics. The first, dedicated to the light sheet and camera optics, is 32.4 cm above the optics table, and the second, used for the tweezer beam expansion and deflection, 55.2 cm.

Figure 5.3 gives an overview of the final setup. Not shown is the hardware used to mount the Newport VP-25XA Precision Compact Linear Stage to the lower breadboard. This consisted of an X-Y manual translation stage, a sturdy 1.5 in diameter post for vertical positioning, and a custom aluminum plate machined to allow the motorized stage to be cantilevered away from the X-Y stage because of space constraints.

The first design consideration that had to be addressed was whether the VP-25XA could handle the off-center loading produced by the items that would be attached to it. It was determined (using a load calculation equation provided by the manufacturer) that considering the present location of all centers of mass, the stage could handle up to 12 N, compared to the actual calculated loading of about 7.4 N.

The more fundamental question of stability of position was addressed on an assembly that was built on the far end of the optics table, away from the fragile quartz cell and the optics currently in place. In this way the entire system could be tested in with minimal construction activity actually occurring near the cell itself, and installed as a monolithic unit once it was ready.

Two breadboards were set up and the position of the quartz cell was marked out on the optics table surface with electrical tape. A CCD camera (7.4 μm pixels) with an attached microscope objective was used to image the waist of the Mitutoyo objective. The optical magnification of the camera system was measured as 22.3.

The position and waist of the tweezer beam spot was calculated with Malcolm Boshier's becVideo

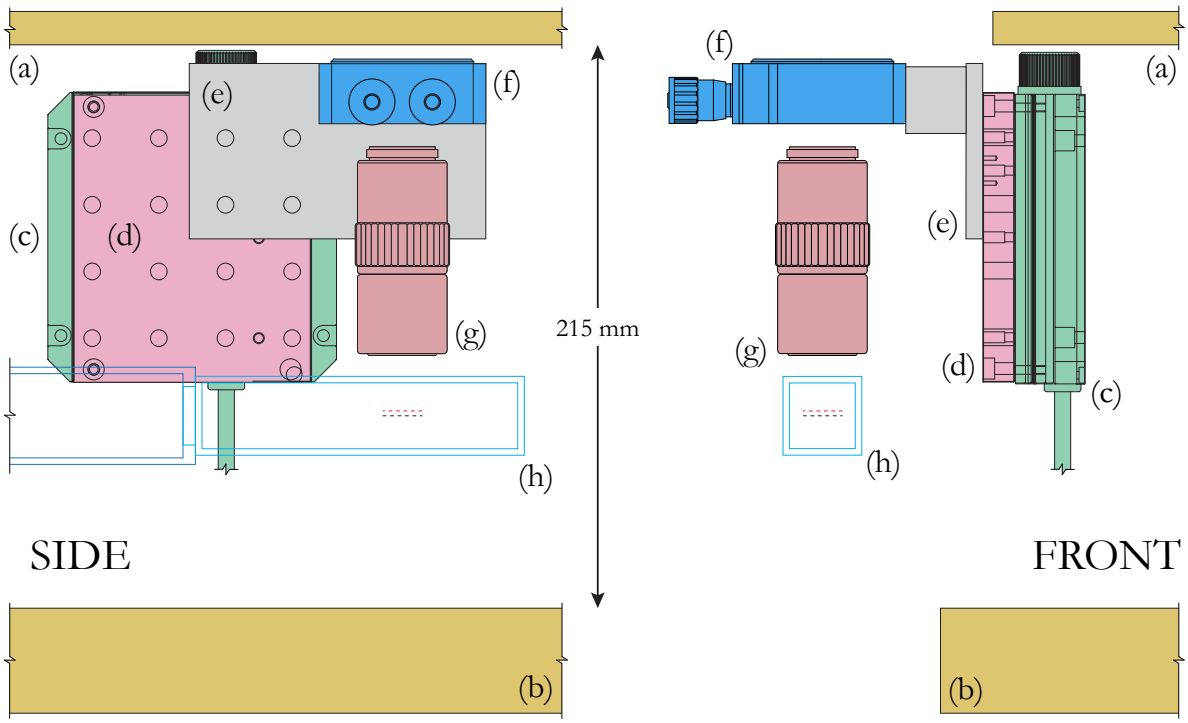

Figure 5.3: Vertical motion stage setup for tweezer beam. Of the three optical surfaces used at the LP end of the experiment (the main optical table is not shown) two are depicted: the topmost breadboard **(a)** (brown) and the middle level breadboard **(b)** (brown). The VP-25XA motorized linear stage **(c)** (green) is mounted vertically in the space between the breadboards (mounting hardware not shown). Its movable section **(d)** (pink) supports a custom plate **(e)** (gray) which, in turn, holds a Thorlabs GM100 gimbal mount **(f)** (blue). Attached to this mount via thread adaptors (omitted for simplicity) is the Mitutoyo tweezer beam objective **(g)** (red). Below it is the LP quartz cell **(h)** (light blue). Technical drawing from Newport used with permission.

LabView program, used for all image analysis tasks related to the LANL BEC experiment. Figure 5.4 shows a screen capture of the program in use while performing the first evaluations of the tweezer beam setup's susceptibility to vibration.

The principal issue that was encountered with the tweezer beam setup was not so much related to the VP-25XA motorized linear stage, but rather the long steel posts upon which the two elevated breadboards are placed. This issue was first noticed while performing several-hour measurement runs to determine how far and at what rate the location in space of the tweezer beam's waist might move. A relatively stable position had been registered one evening, only to find that the focus point had moved upwards by about 9 μm by the next morning. Considering that the lab is temperature controlled, the

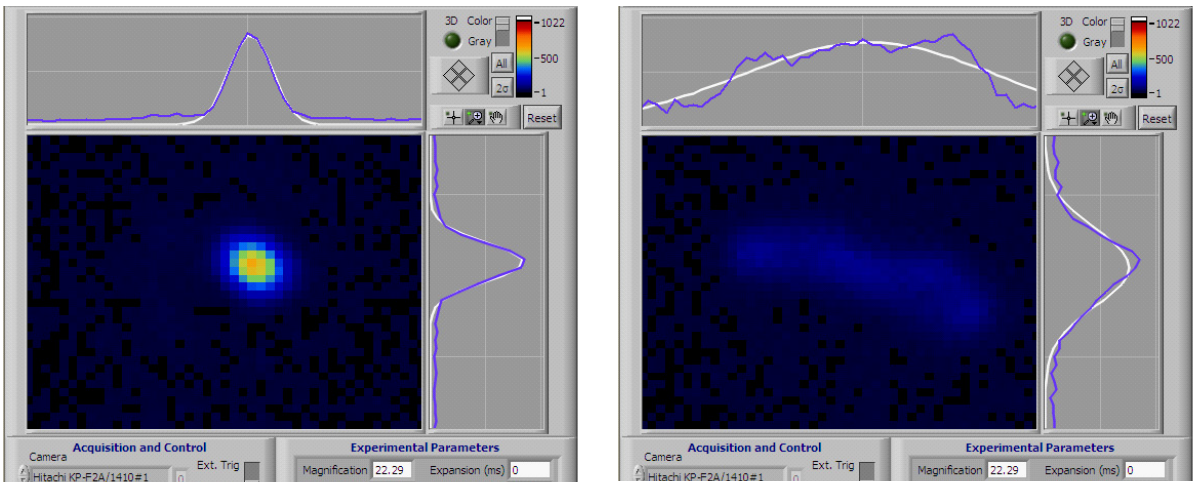

Figure 5.4: Tweezer beam susceptibility to mechanical vibration. Shown is a screen capture of the becVideo program. On the left, a 1.6 μm waist spot is imaged. On the right, an image taken precisely at the moment a vigorous stomp on the lab floor is produced 5 m away. The system was mounted on the far end of a non-floated 5 by 10 ft TMC optics table. Each pixel is 0.3 μm in the image. The camera setup was sandbagged with several large plastic bags of steel ball bearings as an attempt to damp camera vibration.

only difference between both runs was the operation of the Thermo Neslab Merlin M75 chiller, located about 1.5 m from the tweezer beam test setup. As a point of reference, a 1 °C change in 8 inch posts made of 303 stainless steel (of coefficient of thermal expansion about 17.3×10^{-6} m/°C) will result in a calculate change in length of about 3.5 μm. It was considered reasonable to conclude that the drift was a result of thermal effects and not creep in the VP-25XA drive mechanism (which the preloaded ballscrew mechanism is precisely designed to avoid). Indeed, in actual day-to-day operation of the final setup, the vertical location of the tweezer beam's focus must be adjusted, and it is predictable enough that the operator can guess at the correction required by noting the room temperature indicated on the lab's climate control panel.[1]

5.3 Summary

High-NA beam expanders and retro-reflectors were designed and assembled. These expanders allow very straightforward collimation adjustment, are relatively light, and completely modular. The HP expanders provide a MOT beam that is approximately 1.5 times the diameter of the Sussex-era MOT

[1] C. Ryu, personal communication.

beams. The addition of a motorized stage for the tweezer beam has resulted in focal plane stability limited essentially by thermal drift of the entire optical setup, while adjustments can be made to the focal plane position remotely and on the order of a μm.

Chapter 6

Phase Contrast Imaging

Phase-contrast imaging potentially allows the non-destructive imaging of Bose-Einstein Condensates. Under the right conditions, an image or series of phase-contrast images can be obtained to study the state or time evolution of a trapped BEC while minimizing the procedure's influence on the atoms. The goal of this chapter is to determine whether or not phase-contrast imaging can be applied to the present experimental setup, given constraints of repeatability, signal to noise in the final image, optical resolution and imaging time.

6.1 Overview

When a laser shines through a BEC, the laser will undergo a position-dependent phase shift and attenuation. These processes can be characterized by the complex index of refraction of the medium[1] $n = \sqrt{1 + \chi_e}$, which is position-dependent via the electric susceptibility χ_e of the medium. This susceptibility depends on the density distribution of the atoms in space, as well as the particular nature of their interaction with the laser light. Taken in cross-section, the beam will end up with a final total attenuation and phase shift. Under very reasonable assumptions, it is possible to derive expressions for this total phase shift and attenuation at every transverse point in the beam, which depends only on the integrated column density of atoms that a given portion of the beam has had to pass through.

If non-destructiveness is not a requirement, the simplest approach to imaging the BEC is to tune

[1] Elsewhere in this thesis, n represents the volumetric number density of atoms in the gas, N/V, but just this once we will use it to represent the index of refraction.

the laser in such a way that the absorption of the beam, as it passes through the atom cloud, leaves a shadow representation of the BEC. The intensity is attenuated as $I = I_0 e^{-D(\mathbf{r})}$, where $D(\mathbf{r})$ is the optical depth. This intensity profile can be processed to yield the atomic density distribution. This process is destructive, since the temperature of the BEC is so low, the recoil energy of each photon that is scattered by an atom is enough to kick said atom out of the cloud ($E_r \sim 45$nK for ^{87}Rb). Additionally, this technique is only practical when the optical depth of the BEC does not exceed about 3 or so [63]. This requires either arranging for a BEC with a low density or detuning the laser light from resonance, which, depending on the size of the detuning chosen, can have the unfortunate side effect of deviating the beam via lensing effects.

If non-destructiveness is sought, then a method that does not rely on the spontaneous scattering of the beam's photons must be used. There are several methods that rely instead on the phase shift imparted by the atoms to the beam. The actual method used to measure the phase shift of the light differentiates the methods, but they all depend on being able to separate the scattered and unscattered components of the beam in some way, and control their interference.

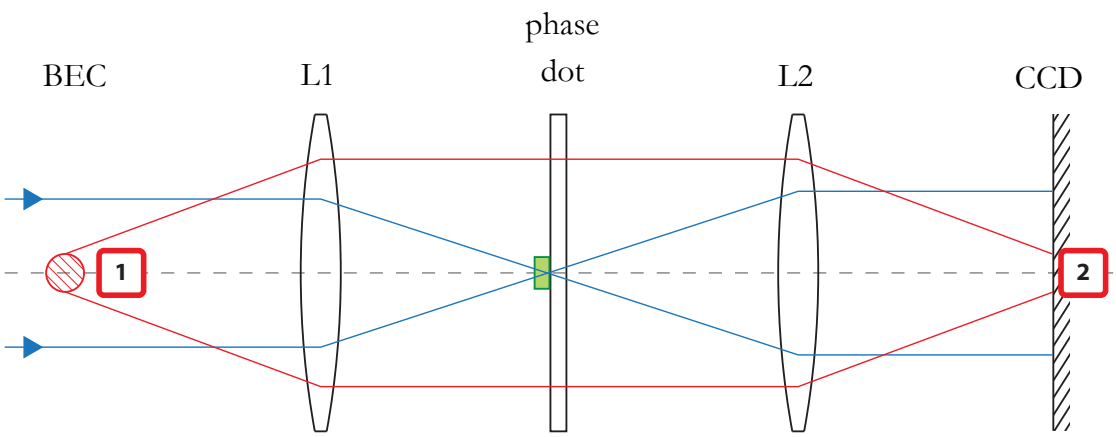

Figure 6.1: Phase contrast imaging setup of unity magnification (not to scale). The BEC, which has features on the order of 1 μm, is located at the focal point of lens L1 **(1)**. Light from the incoming probe (blue) beam is scattered by the BEC (red). After passing through L1, the unscattered light (blue) is phase shifted by a small phase dot (green) of about 100 μm diameter located at the back focal plane of L1. The light that was scattered by the BEC is almost entirely unaffected by the phase dot, and is focused onto the CCD by L2 **(2)**. The phase-shifted probe light interferes with this scattered light to produce the phase contrast signal. This imaging setup is that used by [64], for example.

The earliest form of phase-based imaging was the Schlieren (German; *streak*) used by A. Toepler in 1864, and the 1934 Nobel prize in physics went to Fritz Zernike for the phase-contrast method. In our implementation of this method a pair of lenses are used to focus the light scattered by the BEC

onto the CCD plane of a camera, as in Figure 6.1 . The unscattered laser light, having entered the lens system collimated, is focused down to a small waist between the lenses. At this point a small feature on a glass blank shifts the phase of this unscattered light by a given amount, which we will take as $\pi/2$ in the example below. This feature is usually a $MgFl_2$ dot no more than a few hundred micrometers in diameter. At the CCD plane, the phase-shifted light and that scattered by the atoms interferes, presenting an image signal that can be processed to yield the BEC's density along the optical axis.

A simple analysis of the phase shifts that the light undergoes in passing through this optical system yields a useful expression for the intensity at the CCD. Referring to the phasor diagram of Figure 6.2, we note that the electric field of the light scattered by the atoms can be expressed as $\Delta E = E - E_0$, where $E = te^{i\phi}E_0$ is the attenuated and phase-shifted light that we would encounter immediately behind the atom cloud (i.e., point **(1)** of Figure 6.1) and E_0 is the incoming unscattered probe light. The electric field E_{PC} at the CCD (at **(2)** in Figure 6.1), is then

$$E_{\mathrm{PC}} = E_0 e^{i\pi/2} + \Delta E \tag{6.1}$$

$$= E_0 e^{i\pi/2} + te^{i\phi}E_0 - E_0 \tag{6.2}$$

$$= E_0(e^{i\pi/2} + te^{i\phi} - 1). \tag{6.3}$$

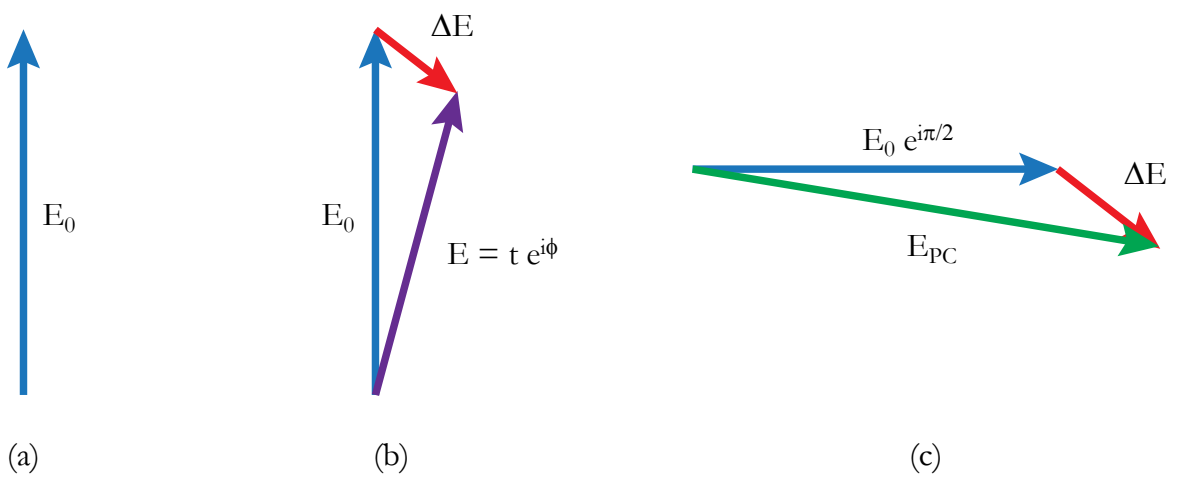

Figure 6.2: Phasor diagram for phase contrast imaging. **(a)** Incoming laser light is represented by phasor E_0. After encountering the atoms, the light immediately behind the atom cloud (labelled **(1)** in Figure 6.1) is phase-shifted and attenuated to $E = te^{i\phi}$ (purple). This phasor can be decomposed as the sum of the light scattered by the atoms (red), ΔE, and the original unscattered light, E_0. **(c)** After phase-shifting the unscattered light by $\pi/2$, the light scattered by the atoms interferes with the phase-shifted unscattered light. This results in the field described by the phasor E_{PC}. Adapted from [65].

The intensity of the light at the CCD is given by $I_{\mathrm{PC}} = \frac{c\epsilon_0}{2} E_{\mathrm{PC}} E^*_{\mathrm{PC}}$. As we will see later in this Chapter, we are interested in the case when the attenuation produced by the atoms is very small. In our case and considering the approximately ideal detuning we will arrive at later in this chapter, the transmission factor is only about 10^{-3} away from 1, and thus does not contribute in any significant way to our calculations. This justifies taking $t \to 1$. We also generalize the phase dot's phase shift from $\pi/2$ to θ, and after some algebra, we find

$$I_{\mathrm{after}} = I_{\mathrm{before}} \left(3 + 2\cos(\theta - \phi) - 2\cos\theta - 2\cos\phi\right). \tag{6.4}$$

The fractional phase contrast signal, a quantity that will be useful to us later on, is defined as $S_{PC} = (I_0 - I_{PC})/I_0$, and

$$S_{PC} = 2(\cos\theta + \cos\phi - \cos(\theta - \phi) - 1). \tag{6.5}$$

We note that if the phase shift ϕ imparted by the atoms is small (and in our case it certainly is) then, to first order in ϕ, the phase contrast signal is

$$S_{PC} = -2\phi \sin\theta, \tag{6.6}$$

which is linear in ϕ.

Returning to our complete expression for the phase contrast intensity I_{PC} (Equation 6.4), it is instructive to graph the dependence of the signal on the atom-induced phase shift, for various phase-shift plates. As we will see later, we expect to be operating in a situation where the total phase shift imparted by the atoms is quite small, on the order of 10^{-1}. It is clear from Figure 6.3 that the magnitude of the relative intensity of the light reaching the CCD does not depend much on the actual phase dot chosen to retard the unscattered light in this regime.

6.2 Calculation of the effects of the atom cloud on the probe beam

Predicting the actual phase shift we expect the current BEC clouds to impart on the probe laser beam requires a quantitative analysis. Fortunately, for our purposes, the BEC is well-approximated as a classical gas of independent quantum absorbers [66]. The simplest approach is to treat it as a bulk, isotropic dielectric gas, where the symmetry-breaking effect of the small magnetic bias field, used to keep the optically-trapped BEC spin-polarized, is neglected (references [64] and [67] cover the issue in

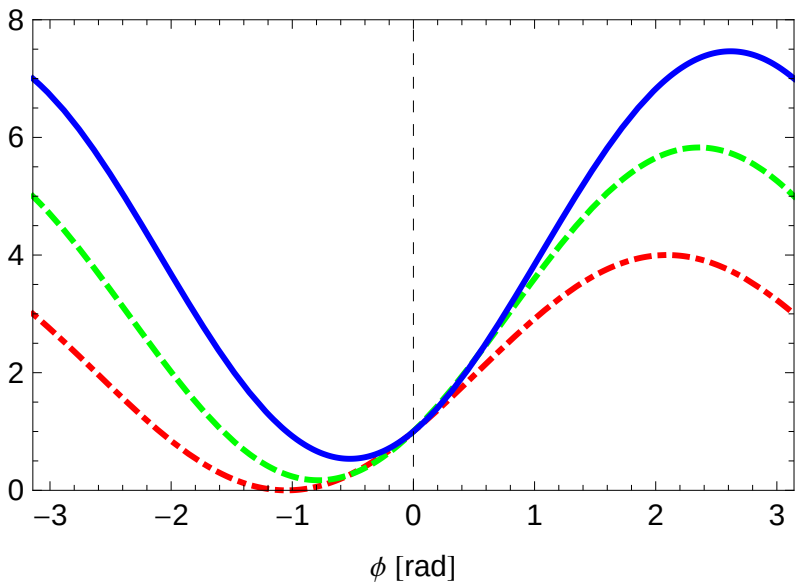

Figure 6.3: Phase contrast relative intensity I/I_0 versus atom phase shift for three different phase dots: $\pi/3$ (red, dot dashed), $\pi/2$ (green, dashed) and $2\pi/3$ (blue, solid).

greater detail). We must arrive, then, at expressions for the absorption and phase shift the medium will impart to a beam given the relevant atomic parameters (atomic density, linewidth of the transition closest to resonance and so on) and the laser frequency.

We expect the light passing through the atom cloud to be attenuated and phase-shifted. We can model these two phenomena simultaneously by allowing a complex wave vector $\tilde{k} = k_r + ik_i$ for a plane wave travelling along the z axis:

$$E_0 e^{i(\tilde{k}z-\omega t)} = E_0 e^{-k_i z} e^{i(k_r z-\omega t)}. \tag{6.7}$$

From the above expression we can easily identify the attenuation and total phase shift the plane wave undergoes at every point along the z axis. What is more relevant to our needs, however, is the total accumulated attenuation and phase shift after the plane wave has traversed a region where $\tilde{k}$ is position-dependent.

The attenuation should follow the Beer-Lambert Law [24], that is: as the beam traverses an absorbing medium, the amplitude of the electric field is reduced as

$$\frac{dE}{dz} = -b(z)E \tag{6.8}$$

where $b(z)$ is a position-dependent attenuation coefficient. This first order differential equation can be

easily solved to yield

$$E(z) = E_0 \exp^{-\int b(z)dz}. \tag{6.9}$$

We identify $b(z)$ as k_i in Equation 6.7. With a similar reasoning for the phase, we find that the plane wave has been attenuated and phase shifted:

$$E(z) = E_0 e^{-\int k_i dz'} e^{i\int k_r dz'} e^{-i\omega t}. \tag{6.10}$$

The integrals are taken over the region in which $\tilde{k}$ departs from k_0, the free space wavenumber. Comparison with a reference plane wave with constant and real k will provide the total attenuation and relative phase shift over the region. In summary, then, an atom cloud will affect light as

$$E_{\text{after}} = tE_{\text{before}} e^{i\phi}. \tag{6.11}$$

We now calculate how $\tilde{k}$ depends on the microscopic physics of the medium.

For simple, nonconductive linear media with no free charges or currents, where $\mathbf{B} = \mu\mathbf{H}$ and $\mathbf{D} = \epsilon\mathbf{E}$, Maxwell's Equations are [68]

$$\begin{aligned} \boldsymbol{\nabla}\cdot\mathbf{B} = 0 \qquad & \boldsymbol{\nabla}\times\mathbf{E} + \frac{\partial}{\partial t}\mathbf{B} = 0 \\ \boldsymbol{\nabla}\cdot\mathbf{D} = 0 \qquad & \boldsymbol{\nabla}\times\mathbf{H} - \frac{\partial}{\partial t}\mathbf{D} = 0. \end{aligned} \tag{6.12}$$

Taking $\boldsymbol{\nabla}\times$ of the top, rightmost equation and making use of the others leads to

$$\nabla^2\mathbf{E} = \mu\epsilon\frac{\partial^2}{\partial t^2}\mathbf{E}. \tag{6.13}$$

This is Maxwell's wave equation for a medium in which $\mathbf{D}$ is isotropic and collinear with $\mathbf{E}$. We substitute a 1D plane wave harmonic solution, $\mathbf{E}(\mathbf{r},t) = \mathbf{E_0}\exp[i(kz - wt)]$, in Equation 6.13 and assuming a nonmagnetic medium ($\mu = \mu_0$), we obtain the dispersion relation for a plane wave in dielectric, linear media.

$$k^2 = \frac{\omega^2}{c^2}\frac{\epsilon}{\epsilon_0}. \tag{6.14}$$

We seek to express Equation 6.14 in terms of parameters more explicitly related to the microscopic physics.

To do this, we note that the electric displacement is defined as

$$\mathbf{D} = \epsilon_0\mathbf{E} + \mathbf{P}, \tag{6.15}$$

where $\mathbf{P}$ is the macroscopic polarization density, and this is assumed to simply be linearly proportional to the electric field $\mathbf{E}$ (given that this is a linear, isotropic medium) via the electric susceptibility χ_e,

$$\mathbf{P} = \epsilon_0 \chi_e \mathbf{E}. \tag{6.16}$$

Given that $\mathbf{D} = \epsilon \mathbf{E}$ in our case, and using Equations 6.15 and 6.16, we obtain an expression for $\epsilon/\epsilon_0 = 1 + \chi_e$, and replace it in our dispersion relation, Equation 6.14, to obtain

$$k^2 = \frac{\omega^2}{c^2}(1 + \chi_e). \tag{6.17}$$

For small χ_e, as is the case with a dilute atomic cloud, $\sqrt{1+\chi_e} \sim 1 + \chi_e/2$ and

$$k_r = \frac{\omega}{c}\left(1 + \frac{1}{2}\,\mathrm{Re}(\chi_e)\right), \tag{6.18}$$

$$k_i = \frac{\omega}{c}\frac{\mathrm{Im}(\chi_e)}{2}. \tag{6.19}$$

We must now link the macroscopic electric susceptibility χ_e to the microscopic physics of the atoms in the BEC. From the macroscopic point of view, we expect the average, position-dependent polarization density $\mathbf{P}$ to be a result of all the induced atomic dipole moments $\langle \mathbf{d} \rangle$, via

$$\mathbf{P} = n \langle \mathbf{d} \rangle, \tag{6.20}$$

where n is the position-dependent number density of atoms in the BEC. From the microscopic point of view, on the other hand, these induced dipole moments are proportional to the applied electric field via the atomic polarizability α as $\langle \mathbf{d} \rangle = \alpha \mathbf{E}$. We can therefore write the polarization density as

$$\mathbf{P} = n \alpha \mathbf{E}. \tag{6.21}$$

Equating Equations 6.21 and 6.16 allows us to relate the electric susceptibility χ_e to the atomic polarizability α as

$$\chi_e = \frac{n\alpha}{\epsilon_0}. \tag{6.22}$$

Finally, Equation 6.18 becomes

$$k_r(z) = \frac{\omega}{c}\left(1 + \frac{n(z)}{2\epsilon_0}\,\mathrm{Re}(\alpha)\right), \tag{6.23}$$

$$k_i(z) = \frac{\omega}{c}\frac{n(z)}{2\epsilon_0}\mathrm{Im}(\alpha). \tag{6.24}$$

In the above, the z dependence of the volumetric number density of the atoms affecting the beam, n, has been made explicit.

The last step in our derivation is to obtain α from a semiclassical model of laser-atom interaction.

6.2.1 Density matrix treatment of the two-level atom

Following the treatment of [69], if we consider the atoms in the BEC as simple two-level systems, then we can start from the simple Hamiltonian

$$\hat{H} = \hbar\omega_e|e\rangle\langle e| + \hbar\omega_g|g\rangle\langle g| - \hat{\mathbf{d}}\cdot\mathbf{E}(\mathbf{r},t) \tag{6.25}$$

where we are assuming $\mathbf{E}(t) = \mathbf{E_0}\cos\omega t$ and the atomic dipole operator is $\hat{\mathbf{d}} = \mathbf{e}_d d(|e\rangle\langle g| + |g\rangle\langle e|)$. d is taken to be real for simplicity, and $\mathbf{e}_d$ is a unit vector parallel to the x axis and to $\mathbf{E}$. In this case Equation 6.25 becomes:

$$\hat{H} = \hbar\omega_e|e\rangle\langle e| + \hbar\omega_g|r\rangle\langle g| - dE(t)(|e\rangle\langle g| + |g\rangle\langle e|). \tag{6.26}$$

In order to simplify the subsequent steps, we offset the zero energy level of the Hamiltonian explicitly by

$$\hat{H} \to \hat{H} - \mathbb{1}\hbar\left(\frac{\omega_e - \omega_g}{2}\right). \tag{6.27}$$

This allows us to write the Hamiltonian as

$$\hat{H} = \frac{\hbar}{2}\omega_0|e\rangle\langle g| - \frac{\hbar}{2}\omega_0|g\rangle\langle g| - dE(t)(|e\rangle\langle g| + |g\rangle\langle e|) \tag{6.28}$$

$$= \begin{bmatrix} \hbar\omega_0/2 & -dE(t) \\ -dE(t) & -\hbar\omega_0/2 \end{bmatrix} \tag{6.29}$$

with $\omega_0 = \omega_e - \omega_g$. We now proceed to calculate the equation of motion for this density matrix,

$$\frac{d\hat{\rho}}{dt} = -\frac{i}{\hbar}[\hat{H},\hat{\rho}] \qquad \text{with } \hat{\rho} = \begin{bmatrix} \rho_{ee} & \rho_{eg} \\ \rho_{ge} & \rho_{gg} \end{bmatrix}. \tag{6.30}$$

We incorporate the phenomenological decay rate Γ manually, as is validated by QED. The collisional decohering rate has been taken as zero.

$$\dot{\rho}_{ee} = -\frac{i}{\hbar}dE(t)(\rho_{eg} - \rho_{ge}) - \Gamma\rho_{ee} \tag{6.31}$$

$$\dot{\rho}_{gg} = +\frac{i}{\hbar}dE(t)(\rho_{eg} - \rho_{ge}) + \Gamma\rho_{ee} \tag{6.32}$$

$$\dot{\rho}_{eg} = -\frac{i}{\hbar}\left[dE(t) + \rho_{eg}\hbar\omega_0\right] - \frac{\Gamma\rho_{ee}}{2}. \tag{6.33}$$

Going to a rotating frame, we define $\rho_{eg} = \tilde{\rho}_{eg}e^{-i\omega t}$ and $\Delta = \omega_0 - \omega$, the laser's detuning from the atomic frequency, and Equation 6.33 becomes

$$\dot{\tilde{\rho}}_{eg}e^{-i\omega t} = -\left(\frac{\Gamma}{2} + i\Delta\right)\rho_{eg} - i\frac{dE(t)}{\hbar}(\rho_{ee} - \rho_{gg}), \tag{6.34}$$

and writing the time dependence of the electric field explicitly,

$$\dot{\tilde{\rho}}_{eg} = -\left(\frac{\Gamma}{2} + i\Delta\right)\tilde{\rho}_{eg} - i\frac{dE_0}{2\hbar}(e^{i\omega t} + e^{-i\omega t})(\rho_{ee}e^{i\omega t} - \rho_{gg}e^{i\omega t}). \tag{6.35}$$

The Rotating Wave Approximation consists of discarding the rapidly oscillating terms of frequency $\omega_0 + \omega$ and keeping the proportionately slower-varying terms of frequency $\omega_0 - \omega$ when the two sets of parentheses are multiplied together. Identifying $\Omega_1 = dE_0/\hbar$ as the Rabi frequency we have

$$\dot{\tilde{\rho}}_{eg} = -\left(\frac{\Gamma}{2} + i\Delta\right)\tilde{\rho}_{eg} - i\frac{\Omega_1}{2}(\rho_{ee} - \rho_{gg}) \tag{6.36}$$

$$\dot{\rho}_{ee} = -\Gamma\rho_{ee} + i\frac{\Omega_1}{2}(\tilde{\rho}_{ge} - \tilde{\rho}_{eg}) \tag{6.37}$$

$$\dot{\rho}_{gg} = +\Gamma\rho_{ee} - i\frac{\Omega_1}{2}(\tilde{\rho}_{ge} - \tilde{\rho}_{eg}). \tag{6.38}$$

Noting that $(\tilde{\rho}_{eg} - \tilde{\rho}_{ge}) = 2i\mathrm{Im}(\tilde{\rho}_{eg})$, making use of $\rho_{ee} + \rho_{gg} = 1$ and setting all three time derivatives to zero, since we are looking for steady-state solutions, results in [69]

$$\begin{aligned}\tilde{\rho}^{ss}_{eg} &= i\frac{\Omega_1}{2}\frac{(\rho_{gg} - \rho_{ee})}{\Gamma/2 + i\Delta} \\ &= \frac{i\Omega_1}{2}\left(\frac{\Gamma/2 - i\Delta}{\Delta^2 + \Gamma^2/4 + \Omega_1^2/2}\right)\end{aligned} \tag{6.39}$$

$$\rho^{ss}_{ee} = \frac{\Omega_1^2}{4}\left(\frac{1}{\Delta^2 + \Gamma^2/4 + \Omega_1^2/2}\right). \tag{6.40}$$

To relate the steady-state solutions of the two-level atom in the presence of a laser field to the macroscopic polarization, note that the magnitude of the induced polarization density $P = n\langle\hat{d}\rangle$ is

$$P = n\,\mathrm{Tr}(\hat{d}\hat{\rho}) \tag{6.41}$$

$$= n\,\mathrm{Tr}\left\{\begin{bmatrix}\rho_{ee} & \rho_{eg}\\ \rho_{ge} & \rho_{gg}\end{bmatrix}\cdot\begin{bmatrix}0 & d\\ d & 0\end{bmatrix}\right\} \tag{6.42}$$

$$= n(d\tilde{\rho}_{eg}e^{-i\omega t} + d\tilde{\rho}_{ge}e^{i\omega t}). \tag{6.43}$$

We expect the time-dependent polarization density to be proportional to the applied electric field, but allowing for some phase lag. If we write the electric field of the laser and the polarization density of the atom cloud as

$$E(t) = E_0\cos(\omega t) = \tilde{E}^{(+)}e^{-i\omega t} + \tilde{E}^{(-)}e^{i\omega t} \tag{6.44}$$

$$P(t) = \tilde{P}^{(+)}e^{-i\omega t} + \tilde{P}^{(-)}e^{i\omega t} \tag{6.45}$$

with $E_0 = 2|\tilde{E}^{(+)}| = 2|\tilde{E}^{(-)}|$, and $\tilde{E}^{(\pm)}$, $\tilde{P}^{(\pm)}$ complex factors, then we would expect to be able to define the relative amplitude and phase of $\tilde{P}^{(+)}$ and $\tilde{E}^{(+)}$ via a complex atomic polarizability $\tilde{\alpha}$:

$$\tilde{P}^{(+)} = \tilde{\alpha}\tilde{E}^{(+)}, \tag{6.46}$$

and similarly for the complex conjugate. Replacing $\tilde{\rho}_{eg}$ (Equation 6.39) in Equation 6.43 allows us to finally identify the atomic polarizability as

$$\alpha(\omega) = \frac{d^2}{\hbar}\left(\frac{i\Gamma/2 + \Delta}{\Delta^2 + \Gamma^2/4 + \Omega_1^2/2}\right). \tag{6.47}$$

We can now replace this expression in the attenuating and phase-shifting components of the complex wave vector we allowed (Equations 6.23 and 6.24) and these, in turn, into the general expression for the total phase shift an attenuation a plane wave experiences over a certain distance, Equation 6.10. Using the expressions for the linewidth and the definition of the saturation intensity in terms of the Rabi frequency for a two-level atom [24, 69]

$$\Gamma = \frac{1}{4\pi\epsilon_0}\frac{4d^2\omega_0^2}{3\hbar c^3} \quad \text{and} \quad \frac{2\Omega_1^2}{\Gamma} = I/I_{sat}, \tag{6.48}$$

we we find useful expressions for the total phase shift ϕ and attenuation t that monochromatic light will experience moving through a medium of two-level atoms of varying density:

$$\left.\begin{aligned} \phi &= \frac{\sigma_0\tilde{n}}{2}\frac{\delta}{1 + I/I_{sat} + \delta^2} \\ t &= \exp\left[-\frac{\sigma_0\tilde{n}}{2}\frac{I/I_{sat}}{1 + I/I_{sat} + \delta^2}\right] \end{aligned}\right\} \quad \text{for } E_{\text{after}} = tE_{\text{before}}e^{i\phi}. \tag{6.49}$$

where we have defined $\delta = (\omega - \omega_0)/(\Gamma/2)$, the detuning in half linewidths; the resonant cross-section for a two-level atom $\sigma_0 = 6\pi\lambda\!\!\!^{-2}$ and $\tilde{n}$, the column density integrated along the light's path as $\tilde{n} = \int n(x)\, dx$.

6.3 Calculation of the effects of the probe beam on the atom cloud

In the previous section we have arrived at a way to quantify the effect the atom cloud will have on the probe beam. It is also fundamentally important to know what effect the probe beam will have on the atom cloud, since our goal is to carry out the imaging procedure several times with a controlled and bounded deterioration of the cloud after each shot. The most important detrimental effect the probe laser will have on the atom cloud is that of kicking atoms out of the trapping potential via spontaneous emission.

The rate at which an atom will scatter photons inelastically can be found by first considering the meaning of ρ_{ee}. Given the requirement that the sum of the excited and ground state density matrix

diagonal elements be normalized to 1, $\rho_{ee} + \rho_{gg} = 1$, it follows that ρ_{ee} is the fractional probability that an atom has interacted already with the laser beam and is in the excited state. Since this is true also for the steady-state solution, it must be true that the rate at which atoms are excited must match the rate at which they are decaying back down to the ground state. In other words, the rate at which they absorb a photon (and are lost from the trap) is also the rate at which they re-emit a photon by spontaneous emission. The average rate at which an excited atom decays is given by the inverse lifetime of the transition, or Γ. Thus, if we take the product of the fractional excited state probability ρ_{ee} and the rate at which these atoms decay, we obtain an expression for the rate of scattering [70]

$$R(I, \omega) = \Gamma \rho_{ee}. \tag{6.50}$$

Given the steady-state solution for ρ_{ee} (Equation 6.40) and making use of the definition of the saturation intensity (Equation 6.48), we can write the above expression as

$$R(I, \omega) = \frac{\Gamma}{2} \frac{I/I_{sat}}{1 + I/I_s + 4(\Delta/\Gamma)^2}. \tag{6.51}$$

This is the average rate at which an atom is scattered out of the cloud by a photon. It follows that during a pulse of length Δt, the number of atoms lost is $R(I, \omega)\Delta t$ times the number of atoms in the cloud. The probability of loss is the number of atoms lost divided by the total number of atoms, or

$$P_L = \Delta t \, \frac{\Gamma}{2} \frac{I/I_{sat}}{1 + I/I_s + 4(\Delta/\Gamma)^2}. \tag{6.52}$$

The probability of loss will be useful to provide bounds for the intensity, detuning and duration of the probe pulses given a maximum acceptable loss of atoms from the BEC.

It is also worth considering the issue of the transverse momentum transfer that occurs when the atoms interact elastically with the probe beam's photons. As a rough approximation, the refraction angle for a cloud of atoms that induce a phase shift of ϕ on the probe beam and have a representative diameter of d is $2\lambda\phi/\pi d$ [65]. This angle is smaller than the diffraction angle of λ/d when the phase shift is less than $\pi/2$, so we will consider this angle in our reasoning. We can estimate the transverse momentum imparted to the photon, and thus to the atom by conservation of momentum, if we assume that the forward scattering Doppler shifts are small. This allows us to take the magnitude of the photon's initial and final momentum vectors as equal, and $|\mathbf{k}_f - \mathbf{k}_i| = |\Delta\mathbf{k}| = 2k \sin(\theta/2)$. For probe light at 780 nm, a diameter on the order of a micrometer and (as we will see later), a phase shift on the order of 10^{-1}, this works out to a $|\Delta\mathbf{v}|$ of about 3×10^{-4} ms^{-1}.[2] The kinetic energy associated with this velocity is about 0.5 nK (as was also found in [71]), far below the trap depth of at least 100 nK.

[2]For pulses 10 to 20 times shorter than the oscillation period of the trap (as is the usual case), the scattered atoms behave essentially as free particles.

6.4 Feasibility study for phase contrast imaging

Having laid out the theory of phase contrast imaging (PCI), the feasibility of obtaining scientifically useful images must be evaluated. The basic requirements for this imaging method are that it preserve the condensate—both in atom number and in state—relatively undisturbed, and that the signal present at the camera's CCD chip be detectable and above the noise floor.

A CCD pixel, in simple terms, captures photons that arrive at its surface. They are converted into electrons with a certain quantum efficiency η_Q that depends on their wavelength. Each pixel can be considered a "well" into which electrons are placed until the CCD enters the readout stage, or the well becomes full and cannot accept any more photoelectrons. The translation from incoming photons into a usable light intensity signal is subject to several sources of noise.

Dark noise is due to electrons appearing and being registered in the well that were not a product of the incoming photons. The cameras used in this experiment have dark noise counts far below the pixel fill count that the CCDs routinely operate at (numbering in the tens of counts at most). Operating with pixels filled considerably above this limit allows us to neglect dark noise.

Readout noise appears when the photoelectron voltage is turned into a digitized signal. The characteristics of this noise are mainly inherent to the design of the CCD chip and, again, it numbers in the tens of counts.

The main contribution to signal noise is shot noise, which is an inevitable result of the quantum nature of the incoming photons. The photon number fluctuates as a Poissonian distribution. The standard deviation of this type of noise is equal to the square root of the average number of incoming photons. The signal-to-noise ratio for this noise process is $\mathrm{SNR}_{shot} = N/\sqrt{N}$, and it is evident that this ratio can be improved by dealing with a larger average number of photons per pixel per imaging pulse. The way this is done is to increase the intensity of the imaging light such that the pixels that receive the most light are as near as possible to being "full" at the end of the imaging pulse (without actually filling, of course).

The light intensity, however, cannot be increased arbitrarily, since the probability of losing an atom from the cloud depends on the imaging light's intensity, among other things. The probability of loss can be reduced by increasing the detuning from resonance of the imaging light as a compensation for higher intensity. The phase contrast signal will be reduced by doing this, and it is precisely this interdependence of experimental parameters that makes it complex to arrive at an "ideal" configuration.

Nonetheless, it is straightforward to pick certain experimental quantities that will be set according to our requirements, and then calculate what all the other parameters must be set to to achieve these goals. In particular, we wish to calculate the expected phase contrast signal S_{PC} and signal-to-noise ratio SNR_{PC} given a predetermined probability of loss P_L, exposure time Δt, imaging beam's saturation parameter I/I_{sat} and phase shift θ the MgF_2 dot induces.

In order to do this, there is one more relationship between the imaging light and the CCD that must be determined: the number of photoelectrons expected to be accumulated at the pixel given an incoming laser intensity. This can be determined from the total number of photons that fall on an area of size A_{px} over an interval Δt with a probe intensity I at the BEC,

$$N_{well} = \eta_Q \frac{I \Delta t A_{px}}{E_p} \frac{1}{M^2} \tag{6.53}$$

where E_p is the energy hc/λ of a single photon and we have introduced the optical system's linear magnification factor M in anticipation of various possible optical setups.

The signal to noise ratio for the main phase contrast measurement is determined as follows. The smallest meaningful detectable fractional change in a pixel's intensity measurement is $\sqrt{N_{well}}/N_{well}$, or $1/\sqrt{N_{well}}$. The fractional phase contrast signal size S_{PC} is given by Equation 6.5. Thus the ratio of these two quantities corresponds to the phase contrast measurement signal to noise ratio:

$$\mathrm{SNR}_{PC} = \frac{2(\cos\theta + \cos\phi - \cos(\theta - \phi) - 1)}{\sqrt{\frac{E_p M^2}{\eta_Q I \Delta t A_{px}}}} \tag{6.54}$$

This quantity tells us by what factor the signal we are trying to observe is larger than the noise-induced fluctuations in the light intensity. SNR_{PC} should be as far from unity as possible given all other constraints.

Inverting Equation 6.52 provides an expression for the detuning required to attain a given probability of loss:

$$\Delta(P_L, I) = \frac{\Gamma}{2}\sqrt{\frac{I}{I_{sat}}\left(\frac{\Gamma \Delta t}{2P_L} - 1\right) - 1}. \tag{6.55}$$

This expression can then be used in our equation for the phase shift (Equation 6.49) which, in turn, is used in the phase contrast signal (Equation 6.5). We are now equipped with the tools necessary to make a reasonable prediction of the expected phase contrast signal given the expected shape and density of the BEC.

6.4.1 Expected signal and required parameters for observation of the LANL BEC

The Bose-Einstein condensate produced in the P-21 BEC Lab at LANL was described in the Introduction and in [52] in general. Since that publication, new experimental directives will require the succesful determination of the atom number present on either side of a toroidal BEC. The toroid has a Thomas-Fermi radius of approximately 1 μm, and is itself about 4 μm in diameter. For our purposes, we can take the number density as uniform throughout the toroid, even though it is not in reality, and calculate an approximate average number density of

$$\begin{aligned}\rho_0 &= \frac{2 \times 10^3 \text{ atoms}}{2\pi^2 \times 10^{-18} \text{ m}^{-3}} \\ &= 1 \times 10^{20} \text{ m}^{-3}\end{aligned} \tag{6.56}$$

for a 2000-atom BEC. Note that we are now using the symbol ρ_0 to denote number density, as it is unlikely, in what follows, that it will be confused with the density matrix.

Though the precise optical system and magnification that will be used is yet to be determined, it will probably be based on a Mitutoyo "M Plan Apo NIR" objective, an infinity-corrected objective with a numerical aperture of 0.40.[3] The camera will be a MicroMax:512BFT model camera from Princeton Instruments back-illuminated CCD camera. The characteristics of this camera that are relevant to this section are about a 75% quantum efficiency η_Q at 780 nm, 13 μm square pixels and greater than 118,000 e^- full well capacity per pixel. If the optical system is taken to have a magnification of 13, then one pixel at the CCD corresponds to 1 μm^2 at the BEC. The actual magnification that will be used will probably be close to this value.

If an arbitrary probability of loss of 3% is chosen and we imagine that a 100 μs imaging pulse is required, we still have the liberty to choose the pulse's intensity. For fixed P_L and Δt, increasing the intensity increases SNR_{PC} but the signal itself decreases due to the larger detuning required.

The number of parameters that can be varied in an atempt to improve the signal to noise ratio of the measurement within the range of acceptable experimental parameters is rather daunting. Consider two examples for concreteness.

- At $I = I_{sat}/4$, the signal to noise ratio is 7.3 with a fractional signal of 0.21. The detuning required is around 375 MHz, and the phase shift is -0.12. A pixel illuminated by this intensity, however, would be about 1% full.

[3] Mitutoyo Catalog, Section I, order number 378-824-5.

- Increasing the intensity to half the saturation intensity provides a calculated signal to noise ratio of 7.4 with a fractional signal of 0.16. The detuning, in this case, is 530 MHz, and the phase shift is -0.08. The extra intensity results in less than a 2% pixel fill ratio.

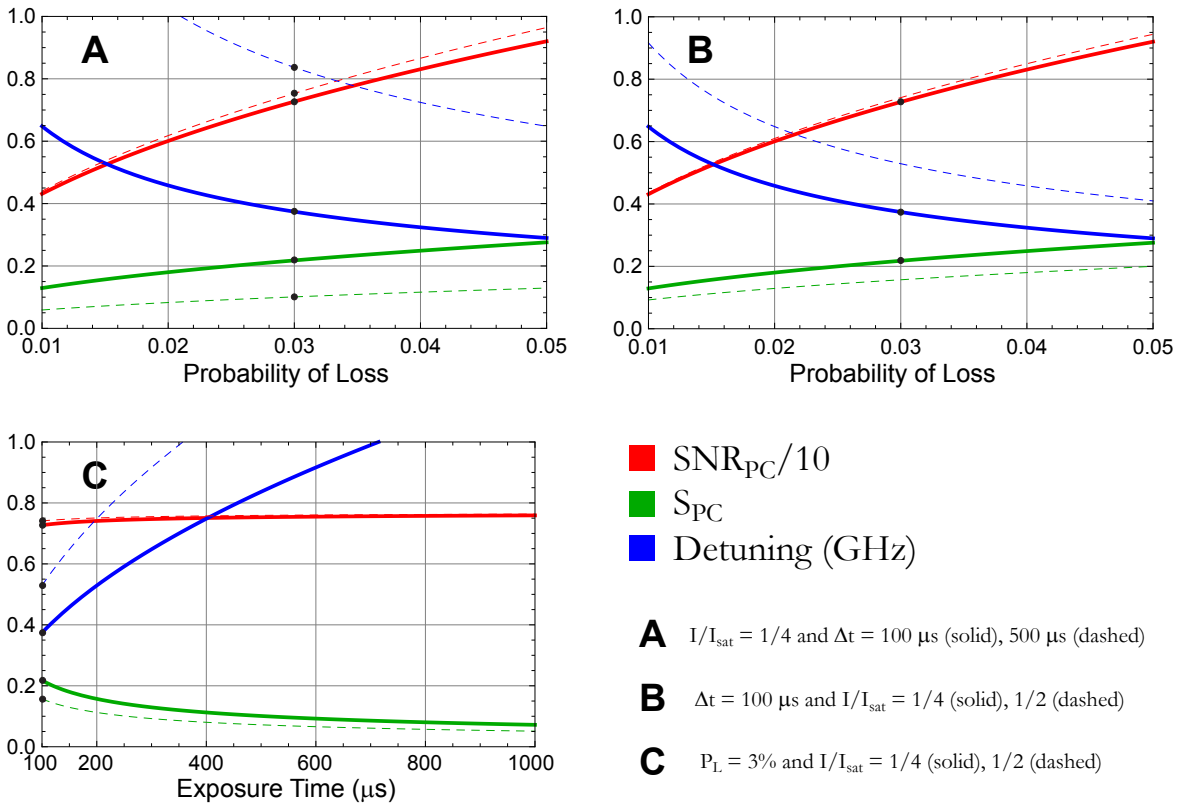

Figure 6.4: Signal-to-noise, phase contrast signal and detuning required given various fixed parameters. Note that the signal to noise ratio, $\mathrm{SNR_{PC}}$, has been rescaled by a factor of 1/10. These three quantities are plotted versus the probability of loss and exposure time for different probe beam intensities or exposure times.

These two examples have been plotted with black dots on the graphs of Figure 6.4 to assist the reader in their interpretation. Plotted are three key quantities of interest: the phase contrast measurement's signal to noise ratio $\mathrm{SNR_{PC}}$ (red), the phase contrast signal $\mathrm{S_{PC}}$ (green) and the detuning required to maintain the required probability of loss (P_L) (blue). These quantities are plotted versus (**A**) P_L for two exposure times, (**B**) versus P_L for two probe intensities, and (**C**) versus exposure time for two probe intensities.

Graph (**A**) tells us that increasing the exposure time from 100 μs to 500 μs hardly helps the signal

to noise ratio, and roughly doubles the size of the detuning required to keep the probability of loss fixed. In fact, Graph (**C**) shows that increasing the exposure time beyond 100 μs will not vary the signal to noise ratio much at all. On the other hand, from Graph (**B**) we see that raising the laser intensity doesn't really help the signal to noise ratio of the measurement either.

The greatest contribution to a higher $\mathrm{SNR_{PC}}$ is, unfortunately, allowing the probability of loss to rise.

6.4.2 Comparison with other publications

It is instructive to compare these expected experimental parameters with other labs' setups. Though several publications that made use of phase contrast imaging for BEC observation were consulted [63, 64, 67, 71–77], there is one that provided enough technical detail about their setup to compare the reported values with those predicted by the relations derived previously in this chapter. These were the publication and thesis of R. Meppelink at the University of Utrecht [67, 73].

R. Meppelink writes about the imaging of the thermal wings of a BEC, using phase contrast imaging to capture an effectively enormous dynamic range of optical density. The element used was sodium, and the phase dot was 50 μm in diameter, imparting a phase shift of $\pi/3$. Using the intensity ratio $I/I_{sat} = 6 \times 10^{-2}$ and a detuning of 281 MHz, my calculated loss rate (via Equation 6.51) is about 200 atoms per second. For a 50 μs exposure, this results in a per-shot loss of about 1% of the atoms in their condensate, a result that they confirm ([67], p. 52).

The camera used in that experiment is an Apogee AP1E, apparently using a Kodak KAF-0401E chip with 9 μm pixels, 0.6 η_Q at the 589.15 nm wavelength of Na and their optical system had a magnification factor of 3 ± 0.05. At the intensity and exposure time they quote, the pixels should be at about 3000 electrons full out of a total well capacity of 100,000, as predicted by Equation 6.53, a 3% fill ratio.

This pixel fill ratio is similar to the situation predicted for the LANL BEC, though it should be noted that the *signal* that they measure is much larger in magnitude. This is due to the much larger physical size of their BEC (20 μm for theirs versus our present case of 1 μm), a situation shared by most of the other experiments reviewed. The LANL BEC, being toroidal in shape and only 1 μm thick along the optical axis, presents a particularly challenging situation in terms of imparting enough phase shift to the probe light to raise the signal to noise ratio for the measurement appreciably. The phase shift is proportional to the integrated column density and this, in turn, is directly proportional to the

condensate's depth.[4] At small phase shifts the signal (Equation 6.6) is linear in the phase shift, so while the LANL BEC might share similar conditions at the CCD, it differs from the reviewed experiments in terms of the size of the signal and the resulting signal to noise ratio for the measurement.

Despite this anticipated challenge, a signal to noise ratio between 7 and 8 (for reasonable detuning parameters and per shot atom loss, as seen above) is still expected to provide scientifically relevant information, suggesting that this imaging method should be attempted.

6.5 Image processing for phase contrast imaging

Experimentally, the imaging sequence consists of three images [67]. First the intensity profile of the probe field with the atoms is obtained, $I_{atoms}(x, y)$. Next, the intensity profile of the probe beam is registered with no atoms, $I_0(x, y)$. The third image is a dark field image taken with no atoms and no probe light, $I_{bg}(x, y)$. This is called a dark frame, and is useful for removing systematic offsets in the CCD signal.

The normalized intensity profile is then, as taken for each pixel at (x, y)

$$I(x, y) = \frac{I_{atoms}(x, y) - I_{bg}(x, y)}{I_0(x, y) - I_{bg}(x, y)}. \tag{6.57}$$

Since the phase shift imparted by the atoms is small, Equation 6.6 can be inverted and used with Equation 6.57 to yield

$$\phi_{atoms}(x, y) = \frac{1}{2 \sin \theta} (1 - I(x, y)) \tag{6.58}$$

or Equation 6.4 can be inverted numerically. The number density of the atom cloud, the quantity we set out to find, is then determined from Equation 6.49.

6.6 Summary

The physical basis for phase-contrast imaging has been studied with the purpose of determining whether or not this imaging method can be applied to future experimental requirements of the LANL BEC experiment. Though the column phase shift imparted by the BECs is much smaller than that imparted by the BECs used in other groups' experiments, it is anticipated that this method can be applied to the LANL BEC to obtain images with a signal-to-noise ratio of over 7 at a total phase shift of about 0.1.

[4] The integrated column density is just $w\rho_0$ if the condensate is taken as being of uniform density and of width w, or $2/3\ w\rho_0$ if the density follows an inverse parabolic distribution.

Chapter 7

Summary and Outlook

The essence of achieving Bose Einstein condensation (BEC) is managing to get a gas of neutral atoms to sit in a potential well and become cold and dense enough that the occupation of the ground state is on the order of the number of atoms in the cloud. This is not easy, and it took 70 years to go from a theoretical description of bosonic condensation to an experimental implementation.

The approach taken with the LANL BEC experiment is to load Rubidium 87 atoms from a very low pressure vapor into a magneto-optical trap (MOT). The trap consists of a combination of appropriately-detuned laser beams, all pointed towards the center of the trap, and a quadrupole magnetic field that have the combined effect of slowing the thermal atoms (with $v_{rms} \sim 300$ m/s at 18 °C), with a deceleration that can be as high as 10^3 times that of gravity, in a volume a few cm in diameter. Once enough atoms have been collected, an on-resonant laser beam pulse shoots the trapped atoms to the other side of the vacuum chamber, into another MOT. This end is called the low pressure (LP) end. The two ends (high and low pressure; HP and LP) of the system are connected only through a long and thin tube, to allow the LP end to be kept at a low pressure (10^{-11} Torr), where the trapped atoms won't suffer too many collisions with background gas, and to allow the high end to be kept at a certain background pressure of Rubidium, to allow enough thermal atoms to be captured in a reasonable time.

The LP MOT will not cool the trapped atoms all the way to BEC, so they are then held in a purely magnetic potential, where the outermost atoms are gradually removed from the trap via an applied RF frequency. Since the outermost atoms are, on average, those with most energy, this removal process cools the remaining atoms. This will only happen, however, if the cloud can rethermalize faster than the rate at which collisions with background gas and three-body collisions in the trapped atoms eject

atoms from the trap. The rethermalization rate is assisted by increasing the current flowing through the magnetic trapping coils, rendering the magnetic potential steeper and tighter, and increasing the density of the atoms, which increases the rate at which they rethermalize.

As the cloud cools and becomes denser, the rate at which it loses atoms from the trap center—via a process called Majorana flips—increases. If left unaddressed, this loss process would empty the trap before reaching BEC. Instead, before these losses become significant, the magnetic potential is turned off and an all-optical dipole potential, created with intense far-detuned laser light, is ramped on. This optical dipole potential does not suffer from the Majorana loss process, and the evaporation of trapped atoms is continued by slowly lowering the intensity of the optical trapping beam, allowing the hottest atoms to escape. This ultimately leads to BEC.

Many of the experimental systems required for the above process, described in far greater detail in Chapter 1, were upgraded between 2009 and 2012. The objectives that these upgrades aimed for and achieved were:

- Faster experimental cycle time,
- More atoms in the BEC,
- Better optical quality and access,
- Robustness and stability.

The way in which each of these objectives was addressed for the Vacuum (Chapter 2), Magnetic Coil (Chapter 3), Laser (Chapter 4) and Optics (Chapter 5) systems is summarized in Table 7.1.

The experimental cycle time has been reduced from 2 minutes to roughly 30 seconds. This is extremely important, since the actual scientific part of the cycle can last only a few tens of milliseconds, and any reduction in the long preliminary stages allows more data to be taken in less time. Larger HP MOT beam diameters with adequate power, provided by the new laser system, result in faster loading of the HP MOT which, in turn, results in a larger flux of atoms being sent to the LP MOT. Also, tighter magnetic trapping potentials allow a faster RF evaporation stage.

Though the maximum number of atoms that can condensed to BEC have not yet been measured (since other, more scientifically interesting and pressing questions were addressed as soon as the LANL BEC machine became operational after the upgrade), it is expected that this number will be significantly larger than the 2×10^5 atoms that could be condensed in the Sussex-era BEC machine.

Motivation	Optics	Vacuum System	Magnetic Coils	Laser System
Faster experimental cycle time	Bigger MOT beams	Higher HP/LP pressure ratio		Power for MOT beams
Larger N BEC	Bigger MOT beams	Higher HP/LP pressure ratio, Faster LP pumping speed	Higher magnetic trap gradient	Power for MOT beams
Better optical quality and access	Quartz cell		Compact quadrupole instead of IP	MOT expanders placed far away
Robustness, stability	Motorized tweezer beam mount		Epoxy potting, damped supports	Mechanical decoupling

Figure 7.1: Experimental system improvement goals, and the way each subsystem was modified to achieve them.

Optical access to the BEC has also improved with the switch to compact anti-Helmholtz coils, as opposed to the bulky Ioffe-Pritchard setup used previously, and higher magnetic field gradients for magnetic trapping and compression have been achieved without having to replace the existing water circuit chiller, booster pump or current source. This was a result of careful consideration of the geometric and thermodynamic properties of the LP magnetic coils.

The beam expanders and retro-reflectors have proved stable, compact and easy to adjust. Their good collimation enables them to be placed relatively far from the cell, allowing valuable space for other optical elements and beams.

Finally, the new quartz cell has improved both the quality and regularity of the potentials that are painted with the 830 nm tweezer beam and the quality of the absorption images from which all experimental information is obtained, and the motorized positioning stage for the tweezer beam has resulted in vertical beam waist position adjustments that are more precise and easier to perform.

The method of phase contrast imaging was studied and, for the current experimental requirements (non-destructively imaging toroidal BECs about 1 μm thick), a smaller total phase shift than that reported by other groups using phase contrast imaging will result in an expected signal to noise ratio that, while not very high, is still expected to provide scientifically useful information.

In summary, all design goals for the construction of an updated BEC machine were met, and the work performed resulted in real and tangible improvements to the machine's capabilities. The experimental implementation of a phase contrast imaging scheme will allow non-destructive images of BECs to be made, further enhancing the scientific usefulness of the LANL BEC machine.

7.1 Outlook

The present-day (May 2012) operation of the LANL BEC machine revolves around the creation of small, ~ 4 μm diameter toroidal BECs, with a thickness of about 1 μm. These traps are created by time-averaging one 830 nm vertical tweezer beam, with its waist sweeping out a circle in the horizontal plane, and a 1064 nm horizontal light sheet beam, sweeping back and forth in the horizontal plane to create a flat optical dipole potential. Taken together, they create a toroidal potential. The greatest limitation to the system's operation is currently the drift that the tweezer beam waist experiences in the vertical direction as compared to the location of the waist of the horizontal light sheet. This drift is thermal in origin, and it is expected that a more thermally-stable mount for the tweezer beam objective will address this issue. Nonetheless, though this drift is a nuisance, it can be manually compensated for via the precision vertical adjustment of the tweezer beam.

The improved optical quality of the new cell has increased the tweezer beam resolution from 4-5 μm previously to around 1.5 μm[1]. This resolution is physically very relevant, since it is now on the order of the BEC *healing length* ξ, defined as the characteristic distance over which the BEC adapts to variations in the potential, e.g. an abrupt step in the trapping potential would create a change in the BEC density profile over a length scale characterized by ξ. The healing length is defined as $\xi = (8\pi na)^{-1/2}$ [26], and for an average particle density of $n \sim 10^{20}$ m^{-3} and a scattering length of about 100 times the Bohr radius, it is about 0.3 μm at its smallest, near the center of the potential.[2]

The significance of attaining painted potentials with a resolution on the order of the healing length is that the degree to which tunneling effects occur across barriers placed in the BEC is characterized by the relationship between the barrier size and the healing length. In the toroidal painted potential, a barrier can be created by momentarily reducing the power in the tweezer beam as it passes the same point on the torus during its painting cycle, thus creating a bump in an otherwise smooth potential. This bump can only be made as narrow as the waist of the tweezer beam allows, and so better optical

[1] It is expected that 1 μm is attainable, though it has not been necessary to do so.

[2] Note that since n is not constant throughout the potential, the healing length will be longer where the density is lower, i.e. towards the edges of the potential.

resolution of the dipole potentials ultimately means narrower and finer potentials can be created for the BEC.

Currently the experimental goal for the LANL BEC group is to study Josephson junction type structures, specifically an analog to the SQUID (superconducting quantum interference device, [78]), using a BEC held in a toroidal potential with two diametrically-opposed raised bumps. These bumps are analogous to the insulating junctions found in a SQUID. The applications include the creation of macroscopic quantum information states (cat states) and ultra-sensitive measurements of rotation, vital to achieving precise inertial navigation systems. The size of the signal obtained from this (tentatively-named atom SQUID) depends on the BEC tunneling current across the potential barriers, and so precise control of their size and shape is vital to the realization of this objective. It is expected that the high resolution painted potentials attained after the system's upgrade will allow these objectives to be reached.

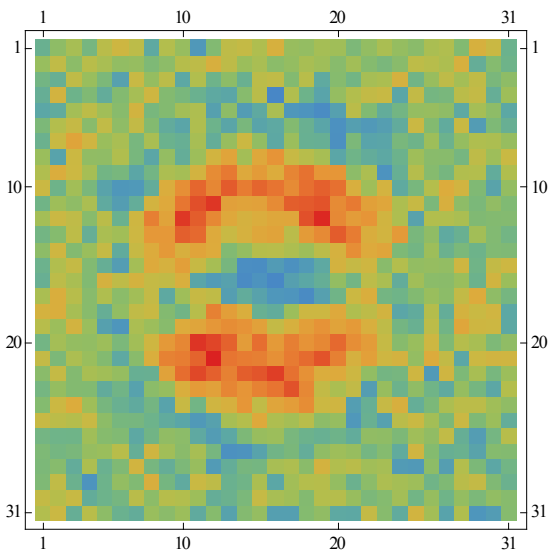

Figure 7.2: Absorption image of toroidal BEC. This absorption image of an 8 μm diameter BEC was taken in-situ, showing the two potential barriers that segment the potential in the horizontal direction. Each pixel is about 0.6 μm in size. Image courtesy of C. Ryu.

In closing, it is important to point out that none of these systems were designed in a vacuum. The valuable, constant input and insight of Dr Boshier and, on occasion, the insightful suggestions of Dr Ryu, were essential to the final designs documented in this Thesis.

References

[1] P. Kapitza, *Viscosity of Liquid Helium below the λ-Point*, Nature **141** (1938), 74–74.

[2] H. Kamerlingh Onnes, *The disappearance of the resistivity of mercury*, Leiden Commun **120b 122b**.

[3] J. Bardeen, L. Cooper, and J. Schrieffer, *Microscopic Theory of Superconductivity*, Physical Review **106** (1957), 162–164.

[4] J. Bardeen, L. N. Cooper, and J. R. Schrieffer, *Theory of Superconductivity*, Physical Review **108** (1957), 1175–1204.

[5] L. Cooper, *Bound Electron Pairs in a Degenerate Fermi Gas*, Physical Review **104** (1956), 1189–1190.

[6] M. H. Anderson, J. R. Ensher, M. R. Matthews, C. E. Wieman, and E. A. Cornell, *Observation of Bose-Einstein Condensation in a Dilute Atomic Vapor.*, Science (New York, N.Y.) **269** (1995), 198–201.

[7] K. Davis, M. Mewes, M. Andrews, N. van Druten, D. Durfee, D. Kurn, and W. Ketterle, *Bose-Einstein Condensation in a Gas of Sodium Atoms*, Physical Review Letters **75** (1995), 3969–3973.

[8] C. Bradley, C. Sackett, J. Tollett, and R. Hulet, *Evidence of Bose-Einstein Condensation in an Atomic Gas with Attractive Interactions*, Physical Review Letters **75** (1995), 1687–1690.

[9] E. Raab, M. Prentiss, A. Cable, S. Chu, and D. Pritchard, *Trapping of Neutral Sodium Atoms with Radiation Pressure*, Physical Review Letters **59** (1987), 2631–2634.

[10] D. Fried, T. Killian, L. Willmann, D. Landhuis, S. Moss, D. Kleppner, and T. Greytak, *Bose-Einstein Condensation of Atomic Hydrogen*, Physical Review Letters **81** (1998), 3811–3814.

[11] S. L. Cornish, N. R. Claussen, J. L. Roberts, E. A. Cornell, and C. E. Wieman, *Stable ˆ{85}Rb Bose-Einstein Condensates with Widely Tunable Interactions*, Physical Review Letters **85** (2000), 1795–1798.

[12] F. Pereira Dos Santos, J. Léonard, J. Wang, C. Barrelet, F. Perales, E. Rasel, C. Unnikrishnan, M. Leduc, and C. Cohen-Tannoudji, *Bose-Einstein Condensation of Metastable Helium*, Physical Review Letters **86** (2001), 3459–3462.

[13] A. Robert, O. Sirjean, A. Browaeys, J. Poupard, S. Nowak, D. Boiron, C. I. Westbrook, and A. Aspect, *A Bose-Einstein condensate of metastable atoms.*, Science (New York, N.Y.) **292** (2001), 461–4.

[14] G. Modugno, G. Ferrari, G. Roati, R. J. Brecha, A. Simoni, and M. Inguscio, *Bose-Einstein condensation of potassium atoms by sympathetic cooling.*, Science (New York, N.Y.) **294** (2001), 1320–2.

[15] T. Weber, J. Herbig, M. Mark, H.-C. Nägerl, and R. Grimm, *Bose-Einstein condensation of cesium.*, Science (New York, N.Y.) **299** (2003), 232–5.

[16] Y. Takasu, K. Maki, K. Komori, T. Takano, K. Honda, M. Kumakura, T. Yabuzaki, and Y. Takahashi, *Spin-Singlet Bose-Einstein Condensation of Two-Electron Atoms*, Physical Review Letters **91** (2003), 3–6.

[17] A. Griesmaier, J. Werner, S. Hensler, J. Stuhler, and T. Pfau, *Bose-Einstein Condensation of Chromium*, Physical Review Letters **94**.

[18] S. Stellmer, M. Tey, B. Huang, R. Grimm, and F. Schreck, *Bose-Einstein Condensation of Strontium*, Physical Review Letters **103**.

[19] S. Stellmer, M. Tey, R. Grimm, and F. Schreck, *Bose-Einstein condensation of ˆ{86}Sr*, Physical Review A **82**.

[20] P. G. Mickelson, Y. N. Martinez de Escobar, M. Yan, B. J. DeSalvo, and T. C. Killian, *Bose-Einstein condensation of ˆ{88}Sr through sympathetic cooling with ˆ{87}Sr*, Physical Review A **81**.

[21] A. Einstein.., -, Sitzber. Kgl. Preuss. Akad. Wiss. **-** (1924), 261.

[22] A. Einstein., -, Sitzber. Kgl. Preuss. Akad. Wiss. **-** (1925), 3.

[23] S. N. Bose, *Plancks Gesetz und Lichtquantenhypothese*, Z. Phys. **26** (1924), 178.

[24] C. J. Foot, *Atomic physics*, Oxford University Press, Oxford; New York, 2005.

[25] K. Huang, *Statistical Mechanics*, Wiley, New York, 1987.

[26] F. Dalfovo, S. Giorgini, L. P. Pitaevskii, and S. Stringari, *Theory of Bose-Einstein condensation in trapped gases*, Reviews of Modern Physics **71** (1999), 463–512.

[27] L. P. Pitaevskii, *Vortex lines in an imperfect Bose gas*, Sov Phys JETP **13** (1961), 451.

[28] E. P. Gross, *Structure of a quantized vortex in boson systems*, Il Nuovo Cimento **20** (1961), 454–477.

[29] G. Baym and C. Pethick, *Ground-State Properties of Magnetically Trapped Bose-Condensed Rubidium Gas*, Physical Review Letters **76** (1996), 6–9.

[30] A. Tacla, S. Boixo, A. Datta, A. Shaji, and C. Caves, *Nonlinear interferometry with Bose-Einstein condensates*, Physical Review A **82** (2010), 1–9.

[31] C. J. Pethick and H. Smith, *BoseEinstein Condensation in Dilute Gases*, Cambridge University Press, Cambridge, 2008.

[32] E. W. Streed, *87Rubidium Bose-Einstein condensates: Machine Construction and Quantum Zeno Experiments.*, PhD thesis, MIT, 2006.

[33] A. Arnold, *Preparation and Manipulation of an Rb Bose-Einstein Condensate*, PhD thesis, University of Sussex, 1999.

[34] J. Prodan, W. Phillips, and H. Metcalf, *Laser Production of a Very Slow Monoenergetic Atomic Beam*, Physical Review Letters **49** (1982), 1149–1153.

[35] C. Monroe, W. Swann, H. Robinson, and C. Wieman, *Very cold trapped atoms in a vapor cell*, Physical Review Letters **65** (1990), 1571–1574.

[36] T. Hänsch and A. Schawlow, *Cooling of gases by laser radiation*, Optics Communications **13** (1975), 68–69.

[37] P. D. Lett, W. D. Phillips, S. L. Rolston, C. E. Tanner, R. N. Watts, and C. I. Westbrook, *Optical molasses*, Journal of the Optical Society of America B **6** (1989), 2084.

[38] S. Bize, Y. Sortais, M. S. Santos, C. Mandache, A. Clairon, and C. Salomon, *High-accuracy measurement of the 87 Rb ground-state hyperfine splitting in an atomic fountain*, Europhysics Letters (EPL) **45** (1999), 558–564.

[39] J. Ye, S. Swartz, P. Jungner, and J. L. Hall, *Hyperfine structure and absolute frequency of the ˆ87Rb 5P_3/2 state*, Optics Letters **21** (1996), 1280.

[40] D. A. Steck *Rubidium 87 D Line Data*, 2010.

[41] C. J. Myatt, N. R. Newbury, R. W. Ghrist, S. Loutzenhiser, and C. E. Wieman, *Multiply loaded magneto-optical trap*, Optics Letters **21** (1996), 290.

[42] P. Lett, R. Watts, C. Westbrook, W. Phillips, P. Gould, and H. Metcalf, *Observation of Atoms Laser Cooled below the Doppler Limit*, Physical Review Letters **61** (1988), 169–172.

[43] J. Dalibard and C. Cohen-Tannoudji, *Laser cooling below the Doppler limit by polarization gradients: simple theoretical models*, Journal of the Optical Society of America B **6** (1989), 2023.

[44] S. Chu and C. E. Wieman, *Laser Cooling and Trapping of Atoms*, Journal of the Optical Society of America B **6** (1989), 2020.

[45] C. D. Wallace, T. P. Dinneen, K. Y. N. Tan, A. Kumarakrishnan, P. L. Gould, and J. Javanainen, *Measurements of temperature and spring constant in a magneto-optical trap*, Journal of the Optical Society of America B **11** (1994), 703.

[46] K. Davis, M.-O. Mewes, M. Joffe, M. Andrews, and W. Ketterle, *Evaporative Cooling of Sodium Atoms*, Physical Review Letters **74** (1995), 5202–5205.

[47] E. Majorana, *Atomi orientati in campo magnetico variabile*, Nuovo Cimento **9** (1932), 43.

[48] W. Petrich, M. Anderson, J. Ensher, and E. Cornell, *Stable, Tightly Confining Magnetic Trap for Evaporative Cooling of Neutral Atoms*, Physical Review Letters **74** (1995), 3352–3355.

[49] D. Pritchard, *Cooling Neutral Atoms in a Magnetic Trap for Precision Spectroscopy*, Physical Review Letters **51** (1983), 1336–1339.

[50] Y.-J. Lin, a. Perry, R. Compton, I. Spielman, and J. Porto, *Rapid production of R87b Bose-Einstein condensates in a combined magnetic and optical potential*, Physical Review A **79** (2009), 1–8.

[51] R. Grimm, M. Weidemüller, and Y. B. Ovchinnikov, *Optical Dipole Traps for Neutral Atoms*, Advances in Atomic, Molecular and Optical Physics **42** (2000), 95–170.

[52] K. Henderson, C. Ryu, C. MacCormick, and M. G. Boshier, *Experimental demonstration of painting arbitrary and dynamic potentials for BoseEinstein condensates*, New Journal of Physics **11** (2009), 043030.

[53] C. Maccormick, *Coherent Atom Optics with a Dilute Bose-Einstein Condensate*, PhD thesis, University of Sussex, 2002.

[54] J. M. Lafferty, *Foundations of Vacuum Science and Technology*, 1997.

[55] M. Stephens and C. Wieman, *High collection efficiency in a laser trap*, Physical Review Letters **72** (1994), 3787–3790.

[56] T. Bergeman, G. Erez, and H. Metcalf, *Magnetostatic trapping fields for neutral atoms*, Physical Review A **35** (1987), 1535–1546.

[57] D. B. Montgomery, *Solenoid Magnet Design: The Magnetic and Mechanical Aspects of Resistive and Superconducting Systems*, Wiley-Interscience, 1969.

[58] (Tuthill Pump Group) *D Series Specifications 1002-01*, 2001.

[59] U. Volz and H. Schmoranzer, *Precision lifetime measurements on alkali atoms and on helium by beamgaslaser spectroscopy*, Physica Scripta **T65** (1996), 48–56.

[60] K. B. MacAdam, A. Steinbach, and C. Wieman, *A narrow-band tunable diode laser system with grating feedback, and a saturated absorption spectrometer for Cs and Rb*, American Journal of Physics **60** (1992), 1098.

[61] Thorlabs, *Thorlabs Catalog*, 2012.

[62] K. Lindquist, M. Stephens, and C. Wieman, *Experimental and theoretical study of the vapor-cell Zeeman optical trap*, Physical Review A **46** (1992), 4082–4090.

[63] M. Matthews, *Vortices in a Bose-Einstein Condensate*, Physical Review Letters **83** (1999), 2498–2501.

[64] P. C. Haljan, *Vortices in a Bose-Einstein Condensate*, PhD thesis, University of Colorado, 2003.

[65] W. Ketterle, D. S. Durfee, and D. M. Stamper-Kurn, *Making, probing and understanding Bose-Einstein condensates*, Vol. -, 1999, p. 90.

[66] O. Morice, Y. Castin, and J. Dalibard, *Refractive index of a dilute Bose gas*, Physical Review A **51** (1995), 3896–3901.

[67] R. Meppelink, *Hydrodynamic excitations in a Bose-Einstein condensate*, PhD thesis, University of Utrecht, 2009.

[68] J. D. Jackson, *Classical Electrodynamics Third Edition*, Vol. 67, Wiley, 1998.

[69] G. W. F. Drake, *Handbook of Atomic, Molecular, and Optical Physics*, Springer, 2006.

[70] H. J. Metcalf, *Laser cooling and trapping*, Springer, New York, 1999.

[71] M. R. Andrews, M.-O. Mewes, N. J. van Druten, D. S. Durfee, D. M. Kurn, and W. Ketterle, *Direct, Nondestructive Observation of a Bose Condensate*, Science **273** (1996), 84–87.

[72] C. Menotti, M. Kramer, A. Smerzi, L. Pitaevskii, S. Stringari, and M. Krämer, *Propagation of sound in a Bose-Einstein condensate in an optical lattice*, Physical Review A **70** (2004), 1–8.

[73] R. Meppelink, R. A. Rozendaal, S. B. Koller, J. M. Vogels, and P. van der Straten, *Thermodynamics of Bose-Einstein-condensed clouds using phase-contrast imaging*, Physical Review A **81** (2010), –.

[74] M. R. Matthews, *Two-Component Bose-Einstein Condensation*, PhD thesis, University of Colorado, 1999.

[75] D. Scherer, C. Weiler, T. Neely, and B. Anderson, *Vortex Formation by Merging of Multiple Trapped Bose-Einstein Condensates*, Physical Review Letters **98** (2007), 1–4.

[76] D. Scherer, *Vortex formation by merging and interference of multiple trapped Bose Einstein condensates*, PhD thesis, University of Arizona, 2007.

[77] C. C. Bradley, C. A. Sackett, and R. G. Hulet, *Bose-Einstein Condensation of Lithium: Observation of Limited Condensate Number*, Physical Review Letters **78** (1997), 985–989.

[78] T. Ryhnen, H. Sepp, R. Ilmoniemi, and J. Knuutila, *SQUID magnetometers for low-frequency applications*, Journal of Low Temperature Physics **76** (1989), 287–386.